MEASUREMENT AND MODELLING OF BROADBAND AND SPECTRAL GLOBAL IRRADIANCE IN SOUTHERN SASKATCHEWAN, CANADA

by

James Morley
B.Sc., University of Regina, 2003

THESIS SUBMITTED IN PARTIAL FULFILLMENT OF
THE REQUIREMENTS FOR THE DEGREE OF

MASTER OF SCIENCE

In the
Department
of
Geography

SIMON FRASER UNIVERSITY

Summer 2005

Approval

Name:	**James Upton Morley**
Degree:	**Master of Science**
Title of Thesis:	**MEASUREMENT AND MODELLING OF BROADBAND AND SPECTRAL GLOBAL IRRADIANCE IN SOUTHERN SASKATCHEWAN, CANADA**
Examining Committee:	
Chair:	**Dr. N.K. Blomley,** Professor

Dr. W.G. Bailey, Professor
Department of Geography, Simon Fraser University
Senior Supervisor

Dr. A.M. Sawchuk, University College Professor
Department of Geography, Kwantlen University College
Committee Member

Dr. L.J.B. McArthur, Chief, Experimental Studies Division, Air Quality Research Branch,
Meteorological Service of Canada, Environment Canada
Committee Member

Dr. I.G. McKendry, Professor
Department of Geography and Atmospheric Sciences,
University of British Columbia
External Examiner

Date Approved: July 25, 2005

SIMON FRASER UNIVERSITY

PARTIAL COPYRIGHT LICENCE

Abstract

One-minute and daily cloudless sky global, direct and diffuse irradiance measurements at Environment Canada's Baseline Surface Radiation Network Bratt's Lake Observatory in Saskatchewan, throughout 2003, are presented, analyzed and compared to model estimations. The magnitude of broadband irradiances proves highly responsive to changes in optical air mass and aerosol optical depth as shown by the clearness index, transmissivity and diffuse ratio. During summer, wildfire activity in southern British Columbia and the western United States produced aerosols that caused a large increase in optical depth at the Observatory. Attenuation from pyrogenic aerosols caused a negative forcing in broadband global irradiance equal to 3.4 percent.

Spectral global irradiance data collected under summertime cloudless conditions shows increased reductions during periods with pyrogenic aerosol. Both the spectral clearness index and the aerosol optical depth reveal that attenuation is not constant over the spectral range 0.28 to 0.80 micrometres; instead, attenuation increases towards shorter wavelengths.

Dedication

This research is dedicated to the Morley family. To my father Ronald, my mother Patricia, my sister Heather and my three brothers: Robert, David and Andrew.

Acknowledgements

I would like to acknowledge the valuable contributions made by several individuals to this research. From my supervisory committee, I am grateful for the financial support, encouragement and advice provided by Bruce McArthur and Allan Sawchuk. Furthermore, I greatly appreciate the encouragement and comments provided by my external examiner Ian McKendry. Finally, I am particularly thankful for the leadership, generosity, friendship and council given by my senior supervisor Bill Bailey.

I would also like to thank my colleagues from Environment Canada who provided support and advice throughout this research. I am thankful to David Halliwell for his assistance during my field research at the Bratt's Lake Observatory and for help in obtaining aerosol optical depth data. Edmund Wu made important contributions to this research, specifically in the determination of the calibration and scanning speed of the OL 754 Spectroradiometer and in obtaining back trajectory data. I am grateful to Ihab Abboud for his assistance throughout this research, specifically with the construction of the broadband irradiance dataset. Finally, I am very thankful for the friendship and support given by Ormanda Niebergall and Everett Hagar.

Finally, I would like to thank all of the people in the Department of Geography at Simon Fraser University. Specifically, I would like to thank my office mates Scott Weston, Owen Hertzman, Mark Coté and Reesa Dexter for their friendship and encouragement throughout this research. Furthermore, I would like to thank B-Jae Kelly, Robert Huish, Craig Emmerton, Daniel Stevens, Christopher Bone, Kimberly Blais, Taskin Shirazi, Nicole Wright, Vanessa Egginton, Gift Dumedah, Sean Connelly, Aviv Ettya and Jerome Lesemann for their friendship.

Table of Contents

List of Figures

List of Tables

Chapter 1.
Introduction

Solar irradiance is the driving force for the Earth's climate. Solar irradiance entering the Earth's atmosphere is subject to attenuation processes from a variety of atmospheric constituents arising from both natural and anthropogenic sources. Atmospheric gases, cloud and aerosols are the three major atmospheric constituents involved in the attenuation process. Of these three, cloud is often the most difficult atmospheric constituent for which to account. Due to their highly variable temporal nature and strong radiative absorption and scattering characteristics, clouds are capable of causing significant short-term fluctuations in irradiances at the surface. Such natural variability makes it difficult to estimate, describe and analyze surface irradiance under cloudy conditions. As such, this research examines solely surface irradiance under cloudless atmospheric conditions in order to explicitly consider the important role of atmospheric gases and aerosols on irradiance attenuation.

In terms of aerosols, this research focuses on the attenuation effects of pyrogenic aerosols arising from large North American wildland fires. While the important warming role of atmospheric greenhouse gases (i.e. CH_4, CO_2, N_2O, O_3 and H_2O) in climate change is recognized (i.e. Canada's implementation of the Kyoto Protocol) (Intergovernmental Panel on Climate Change, 2001), aerosol effects on climate have received less attention; this despite indications that negative radiative forcing from aerosols could potentially mask warming associated with greenhouse gases (Intergovernmental Panel on Climate Change, 2001; Latha and Badarinath, 2004; Power, 2003). Such cooling effects are not necessarily limited to aerosol source regions, but can also influence surface irradiance over much larger spatial scales. This is not only true of dust and ash, regularly transported by winds over large distances (i.e. documented wind-borne transportation of dust from China into the United States, and widespread distribution of ash from the 1991 volcanic eruption of Mt. Pinatubo), but also of forest

fire aerosols (Gueymard, 2000). The influence of pyrogenic aerosols in terms of radiative forcing, atmospheric chemistry, air pollution and visibility is not only apparent at local scales, but has also been documented at regional scales (O'Neill *et al.*, 2002). Enhanced absorption and scattering of irradiance by aerosols can lead to reduced irradiances at the surface, directly influencing net radiation across a range of spatial and temporal scales. This is significant as net radiation plays a major role in defining the plethora of unique climates observed at the Earth's surface.

This research incorporates data collected entirely from surface based sensors. The initial analysis utilizes broadband instruments for the measurement of direct, diffuse and global irradiance, with the latter analysis using spectrally resolved global irradiance observations. While both types of instruments have inherent advantages and limitations, there are merits to using both in conjunction.

1.1. Study Objectives

The objectives of this thesis are twofold:

(1) To analyze diurnal and seasonal observations of cloudless sky global, direct and diffuse irradiance from one-minute data collected throughout 2003 at Environment Canada's Bratt's Lake Observatory in southern Saskatchewan. Additionally, a cloudless sky global irradiance model is applied in order to quantify the influence of pyrogenic aerosols on incoming broadband irradiance.

(2) To undertake an empirical and numerical study of global spectral irradiance from 0.28 to 0.80 μm employing spectral measurements collected during the summer of 2003. Analysis of spectral data collected during late July and August is of particular interest, when higher aerosol optical depths were measured due to the transport of pyrogenic aerosol plumes from wildland fire sources upwind from the measurement site.

1.2. Thesis Organization

This thesis is organized into four chapters. Following this introductory chapter, thesis material is subdivided into two chapters. Chapter 2 focuses on diurnal and seasonal influences on measured and modelled one-minute and daily global, direct and diffuse broadband irradiance. Chapter 2 also explores the application of a cloudless sky global irradiance model for quantifying pyrogenic aerosol influences on broadband surface irradiance. Chapter 3 examines cloudless sky spectral global irradiance from 0.28 to 0.8 μm and includes a discussion of pyrogenic aerosol effects over this wavelength range. For comparative purposes, measured spectra and integrated irradiance across spectral bands are ratioed against their top-of-atmosphere counterparts to create a clearness index. Major research conclusions are presented in Chapter 4.

1.3. Site Description

All research measurements for this thesis were collected at the Environment Canada Bratt's Lake Observatory (50° 12′ 15.1″ N, 104° 42′ 46.5″ W) (Figure 1.1). The Observatory is located approximately 25 km south of Regina, Saskatchewan and is Canada's contribution to the World Climate Research Programme (WCRP) Baseline Surface Radiation Network (BSRN). Located on the Regina plain, the Observatory encompasses 16 square kilometres of agricultural land (over which there is an elevation gain of less than two metres) and is located at approximately 578 metres above sea level.

The Observatory is located in an area formally classified as the Prairies climatic region (Hare and Thomas, 1974). Annually, the measurement site receives 384 mm of precipitation, 287.2 mm of which falls as rain (Phillips, 1990). While snowfall is an important source of moisture in Saskatchewan, it is generally not heavy, especially in the southern parts of the province (Phillips, 1990; Fung, 1999). The study region is subject to a large annual temperature range. The mean annual temperature is 2.2°C with an average daily temperature of -17.9°C in January and 18.9°C in July (Phillips, 1990).

Westerly winds dominate atmospheric circulation above southern Saskatchewan throughout the year (Fung, 1999). As such, weather systems move generally from west to east across the site (Phillips, 1990), causing short-term yet often intense frontal precipitation events in all seasons. While not a factor in the winter season, intense local heating of the surface during the summer often results in strong convectional precipitation events.

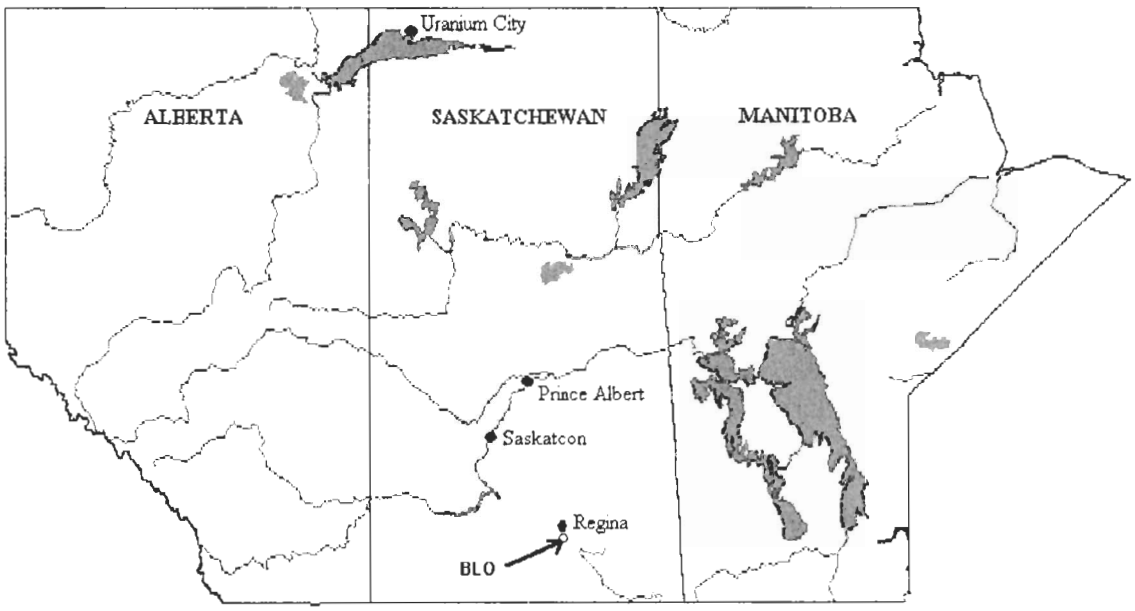

Figure 1.1. Map showing the location of the Bratt's Lake Observatory (BLO), Saskatchewan (50° 12′ 15.1″ N, 104° 42′ 46.5″ W), Canada.

All irradiance measurements employed throughout this research were obtained from instruments located on an elevated measurement platform. The platform is elevated 6.1 metres above the ground surface. Broadband direct, diffuse and global irradiance measurements were collected using a Kipp and Zonen CH1 Pyrheliometer, a shaded Kipp and Zonen CM21 Pyranometer and a Kipp and Zonen CM21 Pyranometer respectively (Figures 1.2 and 1.3). In accordance with BSRN standards, one-minute mean, minimum, maximum and standard deviation values were derived from irradiance measurements recorded at a one-second sampling interval (McArthur, 1998). Furthermore, all

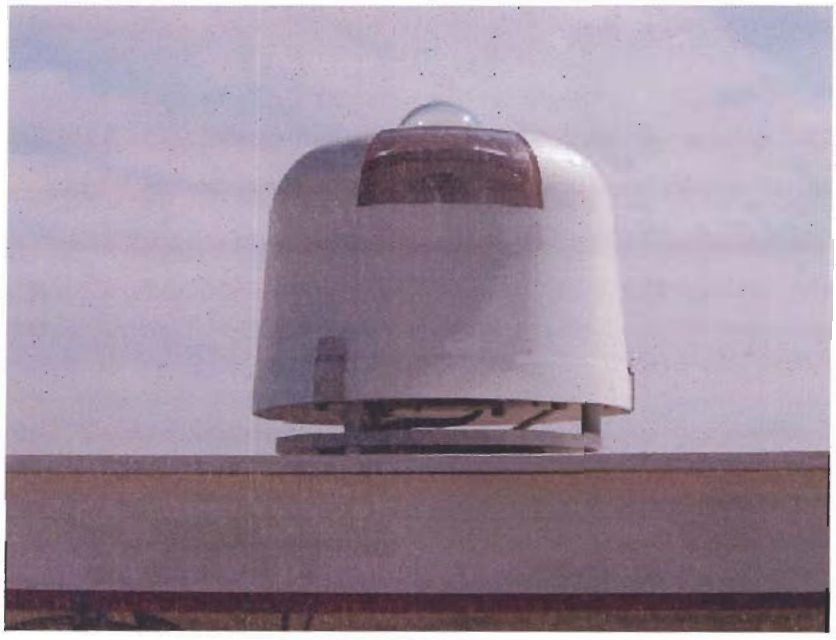

Figure 1.2. Photograph showing a Kipp and Zonen CM21 Pyranometer. The pyranometer measures broadband global irradiance on the elevated platform at the Bratt's Lake Observatory, Saskatchewan.

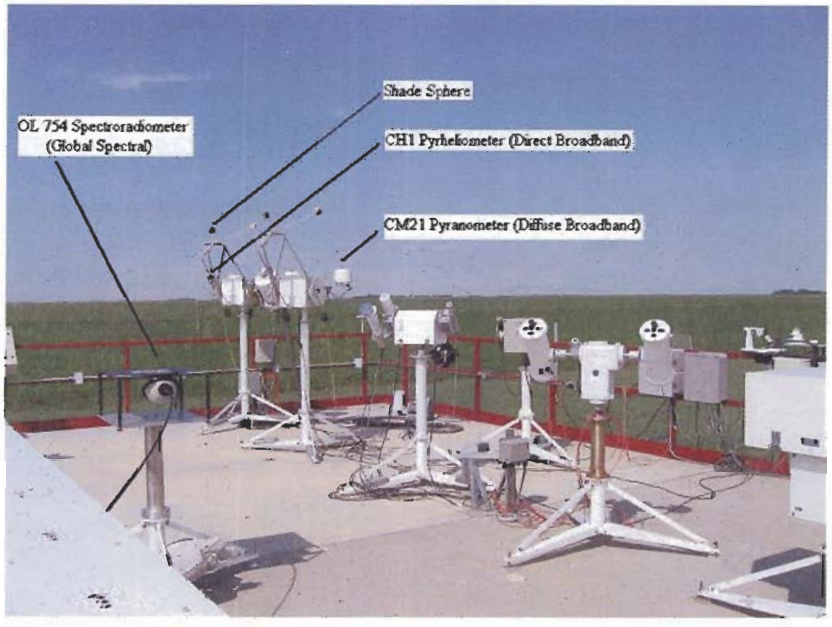

Figure 1.3. Photograph showing broadband direct, diffuse and spectral global irradiance instrumentation on the elevated platform at the Bratt's Lake Observatory. Instruments recording direct and diffuse (with shade sphere) irradiance are pointed at the solar disc. Photograph is looking towards the northeast.

pyranometers were ventilated in order to minimize the influence of infrared absorption and emittance on irradiance measurements. Broadband irradiance measurements were made on a continuous basis throughout 2003, and data collected during cloudless conditions were selected, analyzed and presented in the first half of this research.

Besides broadband measurements, the Observatory houses several spectral instruments. During the summer of 2003, spectral instrumentation at the Observatory included an Optronic Laboratories OL 754 Portable High Accuracy UV-Visible Spectroradiometer (Figure 1.4). Positioned on the main platform, and equipped with an OL 754-O-PMT Optics Head, the OL 754 measured spectral global irradiance on a horizontal surface at 0.001 μm intervals between 0.28 – 0.80 μm. The OL 754 Optics Head consists of a high efficiency double monochromator with dual holographic gratings, an S-20 response thermoelectrically cooled photomultiplier (PMT) detector, and a PTFE coated integrating sphere with fused silica dome (Optronic Laboratories Inc., 1996).

Figure 1.4. Photograph showing the integrating sphere of the Optronic Laboratories OL 754 Portable High Accuracy UV-Visible Spectroradiometer on a tripod. The spectroradiometer measures spectral global irradiance on the elevated platform at the Bratt's Lake Observatory.

With a large user adjustable wavelength range, narrow bandwidth, low stray light level and high wavelength precision and accuracy, the OL 754 is capable of generating high quality measurements of spectral global irradiance. The measurement program ran from June 15 to August 22 and scanning occurred under cloudless sky conditions. Throughout the measurement program (i.e. every three weeks), the OL 754 was calibrated using a 1000 Watt tungsten halogen lamp, an irradiance standard traceable to the National Institute of Standards and Technology (NIST) (Wu, 2002).

Chapter 2.
Measurement and Modelling of Broadband Global Irradiance: The Cloudless Sky Regime in Southern Saskatchewan, Canada

2.1. Introduction

High quality measurements of broadband solar irradiance are of importance to researchers in both scientific and industrial fields. For climatologists, global irradiance is the major source of energy in the Earth's surface radiation balance. Broadband global irradiance data are applied regularly in the field of photobiology (Kelly and Bothwell, 2002; Kelly *et al.*, 2003), for testing radiative transfer models (Monteith, 1962; Idso, 1970; Davies *et al.*, 1975; Davies and McKay 1982, 1989; Gueymard, 2000) and for ground-truthing satellite measurements (World Climate Research Programme, 1991; Whitlock *et al.*, 1995; Pinker *et al.*, 2005). In agricultural science, it is a required input for crop productivity models. In industrial applications, knowledge of global irradiance and its components are necessary for the development and sizing of photovoltaic systems.

Global solar irradiance consists of two separate components, direct beam and diffuse irradiance. This separation distinguishes the irradiance reaching the surface directly from the solar disc from that scattered by the atmosphere and reflected by the ground. Individually, these two parameters provide supplemental information to that obtained solely from global irradiance. For example, measurements of direct irradiance are required to derive important climatological parameters like the aerosol optical depth (Unsworth and Monteith, 1972). Alternately, knowledge of diffuse irradiance is crucial for the design of photovoltaic systems deployed in high latitude and high cloud environments. While global irradiance is routinely measured, direct beam and diffuse irradiance are seldom measured. For example, across Canada there are approximately 35 stations measuring global irradiance, while diffuse irradiance is measured at six stations

and direct beam irradiance at only two stations (L. J. B. McArthur 2005, personal communication). Many times these component irradiances must instead be modelled.

In the cloudless atmosphere, broadband direct beam irradiance can be estimated as a residual after depletion of extraterrestrial irradiance (K_{EX}) by atmospheric scattering and absorption has been accounted for (Davies *et al.*, 1975). This transmittance approach towards estimating irradiance is defined mathematically as

$$S_o = K_{EX}\, T \tag{2.1}$$

where S_o is the cloudless sky direct beam irradiance on a horizontal plane at the Earth's surface and T is the product of transmissions due to water vapour absorption (ϕ_{wa}), ozone absorption (ϕ_{o_3}), dust absorption (ϕ_{da}), water vapour scattering (ϕ_{ws}), dust scattering (ϕ_{ds}), and dry air / Rayleigh scattering (ϕ_{rs}). That is,

$$T = \phi_{rs}\, \phi_{o_3}\, \phi_{wa}\, \phi_{ws}\, \phi_{da}\, \phi_{ds} \quad . \tag{2.2}$$

Equation 2.1 is an application of Beer's law. These transmission functions are exponential functions of species amount and zenith angle. In practical application however, least squares or polynomial relations often approximate these functions (Houghton, 1954; McDonald, 1960; Lacis and Hansen, 1974).

After cloud, aerosols are the greatest extinction source of solar irradiance in the atmosphere (Gueymard *et al.*, 2000). By grouping the last two functions, transmission of solar irradiance due to aerosols (i.e. dust) can be written as

$$\phi_{da}\, \phi_{ds} = e^{-\tau_a m} \tag{2.3}$$

where τ_a is the aerosol optical depth (dimensionless) and m is the optical air mass. By definition, τ_a is a measure of the total aerosol extinction (i.e. the sum of aerosol absorption and scattering) of a beam of irradiance traversing the atmospheric column. The effect of τ_a on surface irradiance is potentially large because aerosol attenuation occurs at visible wavelengths, where absorption and scattering from atmospheric gases (i.e. ozone, water vapour and carbon dioxide) is minimal and irradiance is maximal for the Planck curve.

Aerosol attenuation, which requires knowledge of τ_a, is difficult to model. Difficulties arise due to the highly variable physical and temporal characteristics and strong extinction effects of aerosols. In physical terms, aerosols are small solid or liquid particles that range in size from 10^{-3} to 10^2 μm (Latha and Badarinath, 2004). For a given location, the physical characteristics of aerosols (i.e. size, concentration and chemical composition) depend on several factors, including meteorological conditions and source type. For example, aerosols may originate from either natural (i.e. volcanic eruptions, dust storms, forest fires, ocean spray, vegetation (i.e. pollen and spores) and small insects), or anthropogenic (i.e. industrial, commercial and domestic pollution) sources (Monteith, 1962; Power, 2003). Aerosols can also display large temporal variability, with concentrations fluctuating greatly over short-term periods. Such variability in τ_a has been observed at locations in both eastern and western Canada (Holben *et al.*, 2001; Gutro *et al.*, 2002). For example, on July 6, 2002, NASA (National Aeronautics and Space Administration) researchers and Canadian scientists measured τ_a in Toronto and New York when pyrogenic aerosols from Canadian forest fires were present. Throughout the day, τ_a ranged from approximately 0.5 (i.e. a large optical depth) to over 4.0 (Gutro *et al.*, 2002).

During the summer of 2003, large wildland fires raged across northwestern regions of North America. These fires consumed forest, range and grassland ecosystems throughout the province of British Columbia and the states of Washington, Oregon, Idaho and Montana (Appendix 2) (National Interagency Coordination Center, 2003; Filmon, 2004). These intense and wide-ranging fires introduced large plumes of pyrogenic aerosols into the atmosphere. Prevailing winds transported these aerosol plumes hundreds of kilometres eastward into the skies above southern Alberta and Saskatchewan. Despite the large distance from source locations, the haze was very evident in southern Saskatchewan and must have had a distinct impact on global, direct and diffuse irradiance at the surface. These aerosol plumes also pose a challenge to efforts directed at modelling irradiances.

There are three major objectives for this chapter. There are few estimates of broadband aerosol optical depth for the southern prairies. The first objective is to

estimate aerosol optical depth for a single location in southern Saskatchewan during cloudless days in 2003. While seasonal and diurnal changes in aerosol optical depth are examined, specific focus is placed on the magnitude and variability of aerosol optical depth when pyrogenic aerosols are present. Secondly, seasonal and diurnal global, direct and diffuse irradiance regimes are examined using one-minute measurements, and patterns are linked to changes in atmospheric attenuation via the clearness index, transmissivity and diffuse ratio. The final objective is to assess the accuracy of one-minute estimates of cloudless sky global, direct and diffuse irradiance from the Houghton (1954) model.

The radiative influence of aerosols can be assessed by comparing cloudless sky irradiance measurements collected when aerosols are present with model estimates of irradiance for an atmosphere free from aerosols yet containing O_3, H_2O and CO_2 (Robinson, 1962). Following Unsworth and Monteith (1972), τ_a is calculated from equation 2.3 for all cloudless days in southern Saskatchewan throughout 2003.

Measurements of broadband global, direct and diffuse irradiance were collected at the Environment Canada Baseline Surface Radiation Network (BSRN) Bratt's Lake Observatory located in southern Saskatchewan. Following BSRN standards, irradiance measurements collected at the Observatory are of the highest accuracy; with minimum deviation from true irradiance values being 1% (2 W m^{-2}) for direct, 2% (5 W m^{-2}) for global and 4 % (5 W m^{-2}) for diffuse (McArthur, 1998).

2.2. Calculation of Top-of-Atmosphere and Surface Broadband Irradiance

Irradiance is the rate of solar energy arriving at a surface per unit time and per unit area (Iqbal, 1983). By convention, solar irradiance has a wavelength range from 0.1-4.0 μm. The rate of solar irradiance striking the top of the Earth's atmosphere on a plane of unit area perpendicular to the solar beam at a distance of one astronomical unit is termed the solar constant (I_o) (Iqbal, 1983). While not a 'true' constant (as it fluctuates slightly) the numerical value of the solar constant currently accepted by the space

community is 1366.1 W m^{-2} (American Society for Testing and Materials, 2000; Renewable Resource Data Center, 2005; Johnson, 2005).

Extraterrestrial radiation (K_{EX}) is the rate of solar irradiance incident upon the top of the planetary atmosphere on a horizontal plane of unit area. A numerical value for K_{EX} is calculated by making a simple geometric correction to I_o and accounting for the nature of the Earth's elliptical orbit about the Sun. Hence,

$$K_{EX} = I_o \cos(z) E_o \tag{2.4}$$

where z is the solar zenith angle and E_o is the eccentricity correction factor. E_o is calculated from McCullough (1968) as

$$E_o = 1 + 2\varepsilon \cos(\omega d_n) \tag{2.5}$$

where ε is the eccentricity of the Earth's elliptical orbit (0.01675), ω is a constant (2π / 365), and d_n is the day-of-year (DOY).

Cos(z) is determined from

$$\cos(z) = \sin(ø) \sin(\delta) + \cos(ø) \cos(\delta) \cos(h) \tag{2.6}$$

where ø is the latitude, δ is the declination and h is the hour angle. The declination is calculated from Michalsky (1988) as

$$\delta = \sin^{-1}(\sin(ep) * \sin(\iota)) \tag{2.7}$$

where ep is the obliquity of the ecliptic and ι is the ecliptic longitude. The obliquity of the ecliptic is defined as follows

$$ep = 23.439 - 0.0000004 * n(\text{degrees}) \tag{2.8}$$

where n is defined as

$$n = jd - 2451545.0 \tag{2.9}$$

where jd is the Julian date. The ecliptic longitude is defined as

$$\iota = L + 1.915 * \sin(g) + 0.020 * \sin(2 * g) \tag{2.10}$$

where L (mean longitude) is calculated as

$$L = 280.460 + 0.9856474 * n \tag{2.11}$$

and g (mean anomaly) is calculated as

$$g = 357.528 + 0.9856003 * n \quad (2.12)$$

where L, g and ι are $\geq 0°$ and $< 360°$ (Michalsky, 1988).

The hour angle can be calculated from

$$h = 15 \left| 12 - LAT \right| \quad (2.13)$$

where LAT is the local apparent time. LAT is calculated as

$$LAT = LST + 4(L_S - L_E) + et \quad (2.14)$$

where LST is the local standard time, L_S is the standard meridian, L_E is the local station longitude and et is the equation of time (minutes) (Iqbal, 1983).

As irradiance enters the Earth's atmosphere, attenuation from a variety of atmospheric constituents takes place. Atmospheric gases (i.e. O, O_2, O_3, N, N_2, CO_2, CH_4 and H_2O), cloud and various aerosols (i.e. dust, smoke, ash and sea salts) act to scatter and absorb incoming solar irradiance. While atmospheric absorption depletes direct beam irradiance entering the Earth's atmosphere, scattering redirects this irradiance to other portions of the sky hemisphere. The irradiance scattered from the direct beam and reflected between the atmosphere and ground is termed diffuse irradiance. Together, direct horizontal (S) and diffuse (D) irradiance make up global irradiance (K↓). This relationship is

$$K\downarrow = S + D \quad . \quad (2.15)$$

Houghton (1954) proposed a straightforward approach for modelling the cloudless sky global irradiance at the surface. In developing this model, Houghton made several assumptions regarding atmospheric attenuation. Three of these assumptions are: 1) absorption takes place in the atmosphere before scattering, 2) approximately 50% of aerosol attenuation is by absorption and the other 50% is by scattering, and 3) scattering is isotropic. With respect to the first assumption, some inaccuracy among model estimates is expected as both scattering and absorption processes operate more or less simultaneously within the atmosphere (McDonald, 1960). From the third assumption, model underestimation of global irradiance is expected because large atmospheric

particles scatter more radiation in a forward direction (i.e. Mie scattering) (Houghton, 1954).

The following equations are used to estimate the cloudless sky direct, diffuse and global irradiance at the surface

$$S_o = K_{EX}\, \phi_{wa}\, \phi_{da}\, \phi_{o_3}\, \phi_{ws}\, \phi_{ds}\, \phi_{rs} \tag{2.16}$$

$$D_o = K_{EX} [\phi_{wa}\, \phi_{da}\, \phi_{o_3} (1 - \phi_{ws}\, \phi_{ds}\, \phi_{rs}) / 2] \tag{2.17}$$

where the subscript o denotes cloudless conditions. Equations 2.16 and 2.17 are added to obtain the incoming global irradiance

$$K_o\downarrow = K_{EX} [\phi_{wa}\, \phi_{da}\, \phi_{o_3} (\phi_{ws}\, \phi_{ds}\, \phi_{rs} + 1) / 2] \quad . \tag{2.18}$$

Except for ozone absorption, Davies *et al.* (1975) provide the broadband transmittance functions required to solve equation 2.18 as

$$\phi_d = \phi_{da}\, \phi_{ds} = k^m \tag{2.19}$$

$$\phi_{da} = \phi_{ds} = 0.975^m \tag{2.20}$$

$$\phi_{ws} = 1 - 0.0225\ wm \tag{2.21}$$

$$\phi_{wa} = 1 - 0.077\ wm^{0.3} \tag{2.22}$$

$$\phi_{rs} = 0.972 - 0.08262m + 0.00933\ m^2 - 0.00095\ m^3 + 0.0000437\ m^4 \tag{2.23}$$

where the dust factor k = 0.95, ϕ_d represents the transmissivity due to dust, m is the optical air mass, and wm denotes water mass (m * precipitable water (cm)). While the above transmittance functions for water vapour and Rayleigh scattering are those originally proposed by Houghton (1954), Davies *et al.* (1975) replaced Houghton's original transmission function for water vapour absorption with McDonald's (1960) parameterization (equation 2.22).

Precipitable water measurements were obtained from the Glasgow, Montana Air Force Base, at 48.42° N, 106.53° W, approximately 240 km southwest of the Observatory. Precipitable water measurements are obtained from upper air soundings twice daily, at 0000 and at 1200 UTC. A daily precipitable water value was obtained by

averaging the morning and afternoon values. Appendix 3 examines model sensitivity to precipitable water.

Another assumption made by Houghton was that ozone absorption in the atmosphere is negligible. More recently, however, other researchers have suggested that transmittance for ozone is not negligible. For example, Davies and McKay (1982) use the following formula from Lacis and Hansen (1974) to calculate ozone transmittance

$$\phi_{o_3} = 1 - [0.1082\, X_1 / (1+ 13.86\, X_1)^{0.805}] + \qquad (2.24)$$

$$[0.00658\, X_1 / (1 + (10.36\, X_1)^3)] +$$

$$[0.002118\, X_1 / (1 + 0.0042\, X_1 + 0.00000323\, X_1^2)]$$

where X_1 is determined by

$$X_1 = m\, U_o \qquad (2.25)$$

where U_o is the equivalent ozone depth (cm).

Depending on day length and visibility of the solar disc, a Brewer spectrophotometer collects ozone depth (cm) measurements between 10 and 30 times a day. The Brewer spectrophotometer is located on the elevated instrumentation platform at Environment Canada's Bratt's Lake Observatory. A daily ozone depth value (cm) is derived by averaging these ozone depth values. Appendix 4 summarizes model sensitivity to ozone depth.

Optical air mass is the atmospheric path length through which a solar beam must pass as it travels from the top of the Earth's atmosphere to the surface. Therefore, irradiance entering the Earth's atmosphere close to the horizon travels through a larger portion of the atmosphere than irradiance entering at higher solar elevations. Numerical values for optical air mass range from one (if the Sun is directly overhead) to infinity (as the Sun sinks low on the horizon). For this study, Kasten's (1966) formula is employed

$$m = [\cos(z) + 0.15(93.885 - z)^{-1.253}]^{-1} \quad . \qquad (2.26)$$

Kasten's formula incorporates refraction effects at large zenith angles.

2.3. Experimental Procedure

The experimental site is Environment Canada's Bratt's Lake Observatory (50° 12′ 15.1″ N, 104° 42′ 46.5″ W). The direct, diffuse and global irradiance sensors used in this research are located on an elevated platform, 6.1 metres above the ground surface. The direct, diffuse and global broadband irradiance sensors used in this research are a Kipp and Zonen CH1 Pyrheliometer (mounted on a Sci-Tec Cosmos Tracker with a pointing accuracy better than 0.05°), a shaded Kipp and Zonen CM21 Pyranometer (mounted on a Sci-Tec Cosmos Tracker with the direct beam occluded by a shade sphere) and a Kipp and Zonen CM21 Pyranometer respectively (Table 2.1). For accuracy and contingency purposes, each solar flux (i.e. direct, diffuse and global irradiance) was measured by two identical instruments situated in close proximity to each other on the platform.

These broadband instruments operated continuously throughout 2003, recording irradiance at one-second intervals and storing measurements as one-minute means, together with maximum, minimum and standard deviation values. A data acquisition system was specifically designed for the accurate collection of the above irradiance data.

From this irradiance dataset, individual days were categorized as 1) cloudless full days, 2) cloudless half days (further subdivided into cloudless forenoon and cloudless afternoon categories), and 3) cloudy or cloudy-bright days. Only days falling into the first two categories were selected for study. Days falling into the first category are attributable to periods of mid-latitude anticyclone activity. Throughout 2003, fourteen days fell into this first category. With respect to the second category, early afternoon summertime cloudy periods often arose due to intense surface heating which caused local cumulus clouds to develop. Alternately, cloudless afternoon periods are generally attributable to frontal activity, where forenoon cloudy conditions yield a cloudless afternoon with the passage of fronts, usually cold fronts. Twenty-one days fell into the second category, nine as cloudless forenoon periods, and twelve as cloudless afternoons.

The categorization of cloudless full and one-half days was achieved using minute irradiance plots from the two direct, two diffuse and two global sensors (Table 2.1), as well as with a Multi Filter Rotating Shadow Band Radiometer (MFRSR). The MFRSR provides both broadband and spectral (i.e. at wavelengths 415, 500, 610, 665, 862 and

940 nm) total horizontal, direct normal and diffuse irradiance (Harrison *et al.*, 1994). Diurnal irradiance plots from the MFRSR are generated from spectral data collected sequentially at each wavelength every 15 seconds and integrated into 3-minute averages (Harrison *et al.*, 1994).

Table 2.1. Radiometers employed for the measurement of broadband global, direct and diffuse irradiance.

Instrument	**Parameter**	**Measurement Interval**	**Time Frame**
Kipp and Zonen CM21 Pyranometer	Incoming global irradiance (broadband range: 0.305 – 2.8 μm)	Continuous, 1 minute averages	01/01/03–12/31/03
Kipp and Zonen CM21 Pyranometer (with occluding sphere)	Diffuse irradiance (broadband range: 0.305– 2.8 μm)	Continuous, 1 minute averages	01/01/03–12/31/03
Kipp and Zonen CH1 Pyrheliometer	Direct irradiance (broadband range: 0.20 – 4.0 μm)	Continuous, 1 minute averages	01/01/03–12/31/03

Despite the presence of ventilating fans, the pyranometer sensors employed in this study were subject to infrared absorption and emission during day and night periods. These thermal characteristics are obvious in the negative irradiance readings (or offsets) recorded at night. An algorithm developed by Wardle *et al.* (1996) was applied to correct the dataset for these offsets. This correction acts to reduce the nighttime offsets to less than 1 W m^{-2} and correct the daytime irradiances to an estimated 2 – 3 W m^{-2}.

In order to obtain the highest quality data, all instruments situated on the Observatory's elevated platform were subject to daily maintenance checks. Daily maintenance as needed included: (1) dome cleaning, (2) ventilation fan checks, (3) desiccant checks and (4) instrument levelling checks.

2.4. Aerosol Extinction of Irradiance in Southern Saskatchewan

Interaction of extraterrestrial irradiance with atmospheric aerosols causes depletion of the direct solar beam through absorption, and a corresponding increase in the diffuse flux through scattering. The amount of attenuation by aerosols can be estimated by comparing cloudless sky irradiance measurements collected when aerosols are present with model estimates of irradiance for an atmosphere free from aerosols yet containing O_3, H_2O and CO_2 (Robinson, 1962). Under cloudless conditions, direct beam irradiance on a horizontal surface for an aerosol free atmosphere (S_{oa}) is calculated as

$$S_{oa} = K_{EX}\, \phi_{rs}\, \phi_{o_3}\, \phi_{wa}\, \phi_{ws} \quad . \tag{2.27}$$

From equation (2.27), and cloudless sky measurements of direct horizontal irradiance (S_o), τ_a is calculated using the following approach of Unsworth and Monteith (1972)

$$S_o = S_{oa}\, e^{-\tau_a m} \quad . \tag{2.28}$$

Solving for τ_a from equation 2.28 yields

$$S_o / S_{oa} = e^{-\tau_a m} \tag{2.29}$$

$$\ln (S_o / S_{oa}) = -\tau_a m \tag{2.30}$$

$$\tau_a = (\ln(S_o) - \ln(S_{oa})) \; / \; -m \quad . \tag{2.31}$$

From equation 2.31, the mean and standard deviation of τ_a (i.e. calculated from one-minute τ_a values at $z < 80°$) was determined for all 35 cloudless full and half days identified in 2003.

Analysis of results (i.e. equation 2.31) shows a mean of 0.072 and standard deviation equal to 0.053 (coefficient of variation equal to 73.6%). The large variability in aerosol optical depth is the result of both large (i.e. maximum $\tau_a = 0.251$) and small (i.e. minimum $\tau_a = 0.007$) values.

Daily aerosol optical depths, calculated from one-minute τ_a values, yield a mean of 0.057 and standard deviation equal to 0.045. The frequency distribution of daily values is shown in Figure 2.1.

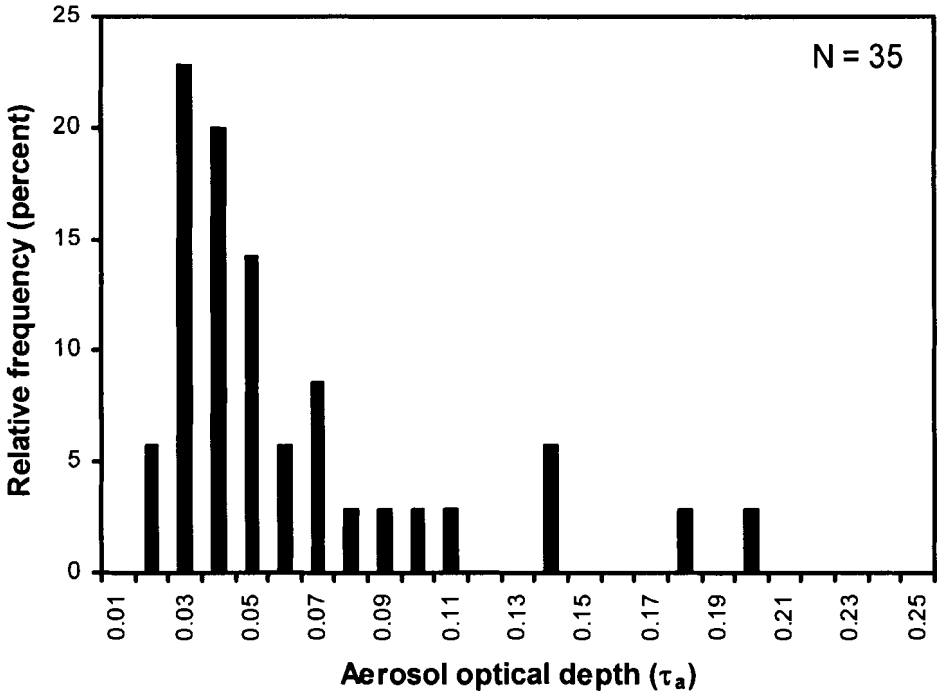

Figure 2.1. Frequency histogram of average daily τ_a ($z < 80°$) values for cloudless full and half days in 2003 at the Bratt's Lake Observatory. The four days (DOY 209, 227, 230 and 231) on which pyrogenic aerosols were present are denoted by the largest τ_a values.

From Figure 2.1, it is apparent that τ_a at the Observatory remains low throughout all seasons, with several larger values causing variability in the seasonal regime. Specifically, τ_a ranged from 0.012 on DOY 42 to 0.198 on DOY 230. The relatively large standard deviation is primarily the result of the large τ_a values on DOY 209, 227, 230 and 231. Excluding these days, τ_a was considerably lower and showed less variability. Specifically, the maximum τ_a was 0.102 on DOY 131, and the average and standard deviation were equal to 0.043 and 0.023, respectively.

By comparison, values of τ_a in Britain are generally greater than values in southern Saskatchewan, ranging from 0.05 to 0.15 in maritime air and from 0.1 to 0.5 in continental air (Unsworth and Monteith, 1972).

From Figure 2.2, and neglecting days with pyrogenic aerosols, τ_a exhibits seasonal change with maximum values occurring in the spring and minimum values in the winter. Smirnov *et al.* (1996) observed a similar pattern in τ_a at 0.5 μm, with a springtime maximum and late autumn minimum at Wynyard, Saskatchewan (51° 46′ N, 104° 12′ W).

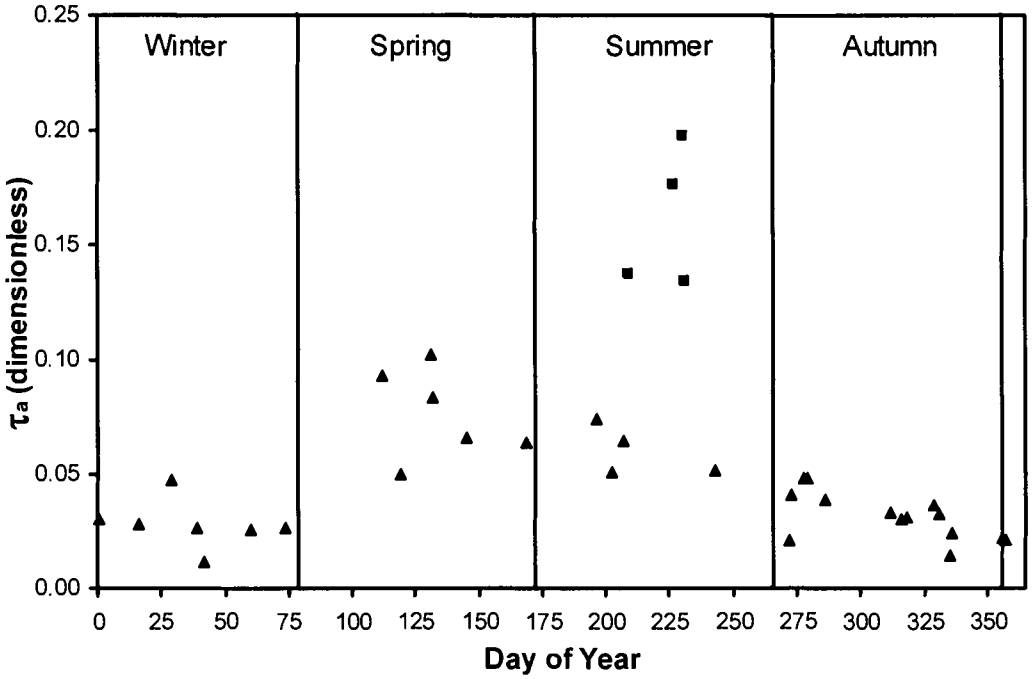

Figure 2.2. Average daily values of τ_a ($z < 80°$) for cloudless full and half days in 2003 at the Bratt's Lake Observatory. The symbol (■) indicates days with pyrogenic aerosols.

The annual τ_a regime for southern Saskatchewan is greatly affected by surface condition. During the winter and late autumn, τ_a is extremely low due to a frozen or snow covered surface. These surface conditions, which characterize the prairie landscape during the winter and late autumn, retain dust at the surface and prevent it from rising into the atmosphere. Following surface thaw in the spring, cultivation of agricultural fields occurs and τ_a is likely to increase. This is because cultivation not only removes surface cover (i.e. stubble), but also loosens the soil causing increased wind erosion and thus more dust in the atmosphere. While soil moisture and wind speed may contribute to

variability in τ_a, it is hypothesised that relatively large values of τ_a observed on DOY 131 and 132 are due to increased atmospheric concentrations of dust arising from the cultivation of agricultural fields in the spring season.

Pyrogenic aerosols arising from upwind wildland fires in British Columbia, and several northwestern states, dramatically influenced τ_a (Figures 2.1 and 2.2) (Appendix 2). The arrival of pyrogenic aerosol plumes at the Observatory (i.e. DOY 209, 227, 230 and 231) caused values of τ_a to rise sharply above normal background levels. On these days, values of τ_a were larger than on all other cloudless days in 2003 (i.e. average equal to 0.162). Furthermore, τ_a showed variability when pyrogenic aerosols were present, ranging from 0.134 on DOY 231 to 0.198 on DOY 230 (i.e. standard deviation equal to 0.031).

The large and unique aerosol attenuation that occurred on DOY 209, 227, 230 and 231 is also apparent in the frequency histogram for average daily τ_a (Figure 2.1). Holben *et al.* (2001) examined τ_a at 0.5 μm for Thompson, Manitoba (55° 47′ N, 97° 50′ W) and presented a similar frequency histogram. Holben *et al.* (2001) noted that while the majority of days from 1994 – 1999 at Thompson coincided with small values of τ_a, the infrequent but large values were attributable to forest fire smoke.

Aerosol particles are subject to atmospheric motion and as such can display strong spatial and temporal variability. For example, pyrogenic aerosols arising from forest fires in Quebec in 2002, caused diurnal variations in τ_a at locations in Toronto and New York in excess of 3.5 (Gutro *et al.*, 2002). Figure 2.3 shows the diurnal variability in τ_a for four cloudless days in 2003; one winter day (i.e. DOY 42), one summer day without pyrogenic aerosols (i.e. DOY 243) and two summer days with pyrogenic aerosols (i.e. DOY 227 and 230). Besides the fact that τ_a is larger when pyrogenic aerosols are present, the diurnal variability is also considerably larger (Table 2.2). From Figure 2.3, it is clear that the diurnal variability on such days is complex, with some days displaying a forenoon maximum and others showing a late afternoon maximum. These observations have implications for modelling irradiances in aerosol-laden environments.

Table 2.2. Daily mean and standard deviation of the aerosol optical depth for the four days listed in Figure 2.3.

DOY	Mean	Standard Deviation
42	0.012	0.001
227	0.177	0.018
230	0.198	0.040
243	0.052	0.011

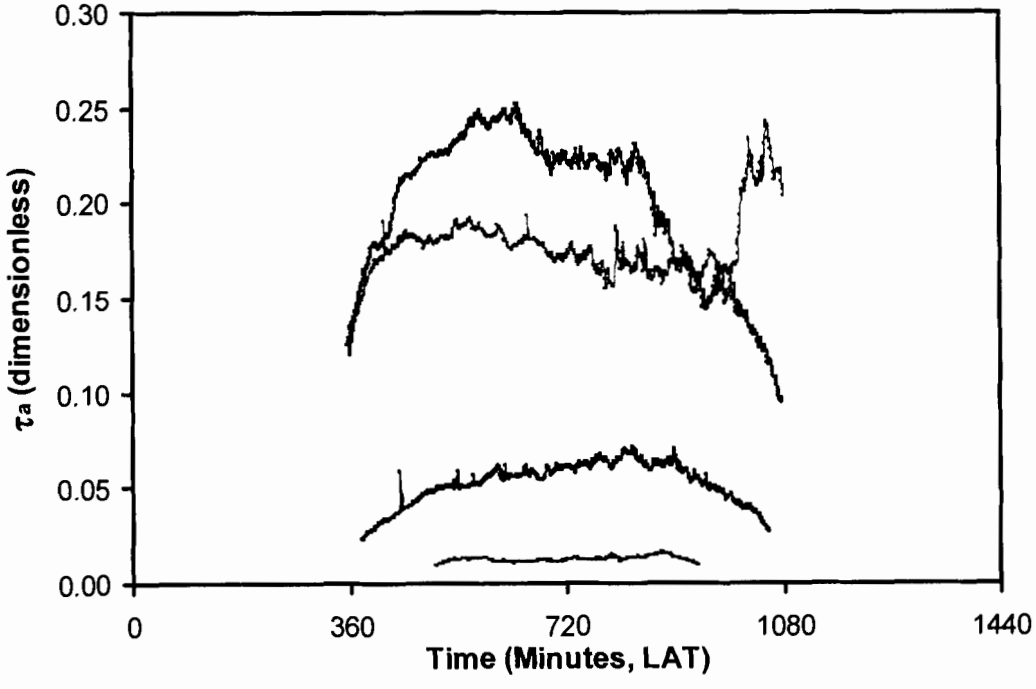

Figure 2.3. One-minute values of τ_a for selected cloudless days in 2003. From top to bottom: DOY 230 (summer pyrogenic aerosol day), DOY 227 (summer pyrogenic aerosol day), DOY 243 (summer day) and DOY 42 (winter day).

2.5. Modelling Cloudless Sky Global Irradiance

2.5.1. Observed Seasonal Cloudless Sky Broadband Global Irradiance Regime

Distinct seasonal differences in cloudless sky global irradiance are evident in southern Saskatchewan in 2003. Furthermore, seasonal differences observed in direct horizontal (from now on referred to as direct), diffuse and extraterrestrial irradiance are

discussed. As only 14 cloudless full days occurred at the Observatory throughout 2003, the 21 cloudless half days were modified to generate 21 artificial cloudless full days. These artificial cloudless full days were created by doubling the half day irradiance totals. Global, direct and diffuse daily totals were calculated from one-minute irradiance measurements while daily totals of extraterrestrial irradiance were derived from one-minute values calculated mathematically (equation 2.4). Table A5.2 of Appendix 5 contains the daily totals for global, direct, diffuse and extraterrestrial irradiance.

As expected, daily totals of extraterrestrial irradiance for the year exhibit a distinct pattern, with mid-year maximum (41.7 MJ m^{-2} d^{-1} on DOY 169) and winter minimum (7.3 MJ m^{-2} d^{-1} on DOY 356) values. From Figure 2.4, it is clear that measurements of cloudless sky global irradiance generally track the trend observed in extraterrestrial irradiance. Maximum and minimum global irradiance values of 31.7 MJ m^{-2} d^{-1} and 5.2 MJ m^{-2} d^{-1} occurred on DOY 169 and DOY 356 respectively. Similarly, direct, and to a lesser extent diffuse irradiance track extraterrestrial irradiance under cloudless conditions (Figure 2.4). However, unlike global irradiance, direct and diffuse irradiance are highly responsive to changes in atmospheric attenuation.

During the summer of 2003, pyrogenic aerosols arising from wildland fires burning in northwestern regions of North America were present in the atmosphere above the Bratt's Lake Observatory. Back trajectory analysis attained from Environment Canada implicates large wildland fires in southern British Columbia and several northwestern states as the primary source regions of the aerosols (Appendix 2). Of the 35 cloudless full and half days recorded in 2003, pyrogenic aerosols were visibly present within the atmosphere on four days. These four days were July 28 (209), August 15 (DOY 227), August 18 (DOY 230) and August 19 (DOY 231). On these days, pyrogenic aerosol concentrations were high enough to modify the cloudless sky seasonal regimes for global, direct and diffuse irradiance. Specifically, the aerosols increased the attenuation of direct irradiance through absorption (i.e. conversion of radiant energy to heat energy) and scattering (i.e. a distinct trough is visible in Figure 2.4), and caused a corresponding aerosol-induced rise in diffuse irradiance via scattering (i.e. a discordant peak is visible in Figure 2.4) (Jacovides *et al.*, 2000; Unsworth and Monteith, 1972). The aerosol-induced rise in diffuse irradiance partially compensated for the dramatic

attenuation of the direct beam and acted to minimize the effects on the global irradiance. This aerosol attenuation, which causes a shortfall in irradiance levels at the surface, is a negative radiative forcing.

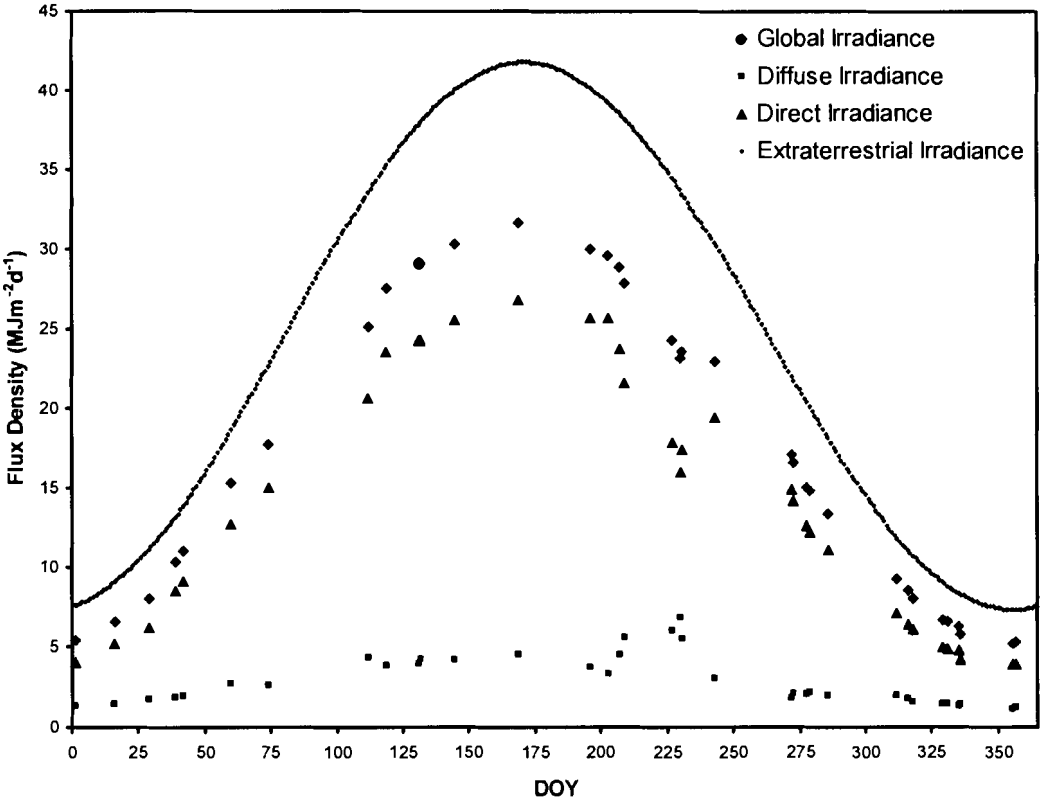

Figure 2.4. Daily totals (full and artificial full) (MJ $m^{-2} d^{-1}$) of global, direct and diffuse irradiances for 2003 under cloudless skies at the Bratt's Lake Observatory. Daily totals of extraterrestrial irradiance (MJ $m^{-2} d^{-1}$) are plotted for 2003. The decrease in daily global and direct irradiance and the increase in daily diffuse irradiance on DOY 209, 227, 230 and 231 are attributable to pyrogenic aerosols.

As discussed, daily values of global, direct and diffuse irradiance experience distinct seasonal change. A portion of this change is attributable to atmospheric effects on irradiance. Under cloudless conditions, the ratios of global, direct and diffuse irradiance to extraterrestrial irradiance can provide three dimensionless measures of atmospheric attenuation. These measures, defined as follows, are the clearness index (c_i), transmissivity (t) and diffuse ratio (d_r)

$$c_i = K\downarrow / K_{EX} \quad (2.32)$$

$$t = S / K_{EX} \quad (2.33)$$

$$d_r = D / K_{EX} \quad . \quad (2.34)$$

Equations 2.32, 2.33 and 2.34 are actual to potential ratios, indicating the actual amount of global, direct and diffuse irradiance reaching the surface relative to the amount of irradiance incident at the top of the planetary atmosphere. While the diffuse ratio is a measure of atmospheric scattering, clearness index and transmissivity are measures of atmospheric transparency. However, of these three ratios, transmissivity is the only pure measure of atmospheric attenuation. This is because diffuse irradiance, which is affected by surface reflectivity, is inherent to both the clearness index and diffuse ratio. Therefore, while the clearness index and diffuse ratio are useful for identifying changes in atmospheric attenuation, scrutiny of these parameters is merited in order to ensure that changes are not solely caused by an increase or decrease in surface reflectivity.

Daily clearness index, transmissivity and diffuse ratio values calculated for the 35 cloudless full and half days identified in 2003 are presented in Figure 2.5 and Table A5.3 (Appendix 5). From Figure 2.5, the average daily clearness index and transmissivity for 2003 are approximately 0.75 and 0.60 respectively. The average daily diffuse ratio for 2003 was approximately 0.13. These average values seem to be especially representative of the majority of spring and summer days (i.e. from DOY 79 – DOY 265). Generally, more significant deviations from these average values occur on winter (DOY 1 – 78, DOY 356 – 365) and autumn days (DOY 266 – 355), or on days in which pyrogenic aerosols were present within the atmosphere.

During the winter and autumn, the increasing and decreasing patterns in the three ratios are linked to optical air mass (i.e. Figure 2.5). In the early parts of 2003, daily clearness index and transmissivity are relatively low while daily diffuse ratio values are relatively high. This is directly attributable to large average daily values of optical air mass (i.e. low solar elevations). This means that extraterrestrial irradiance is subject to more absorption and scattering (relative to mid-year conditions) as it has to pass through a relatively thicker atmospheric column. As DOY increases, the clearness index and transmissivity increase, while the diffuse ratio decreases. Specifically, the clearness

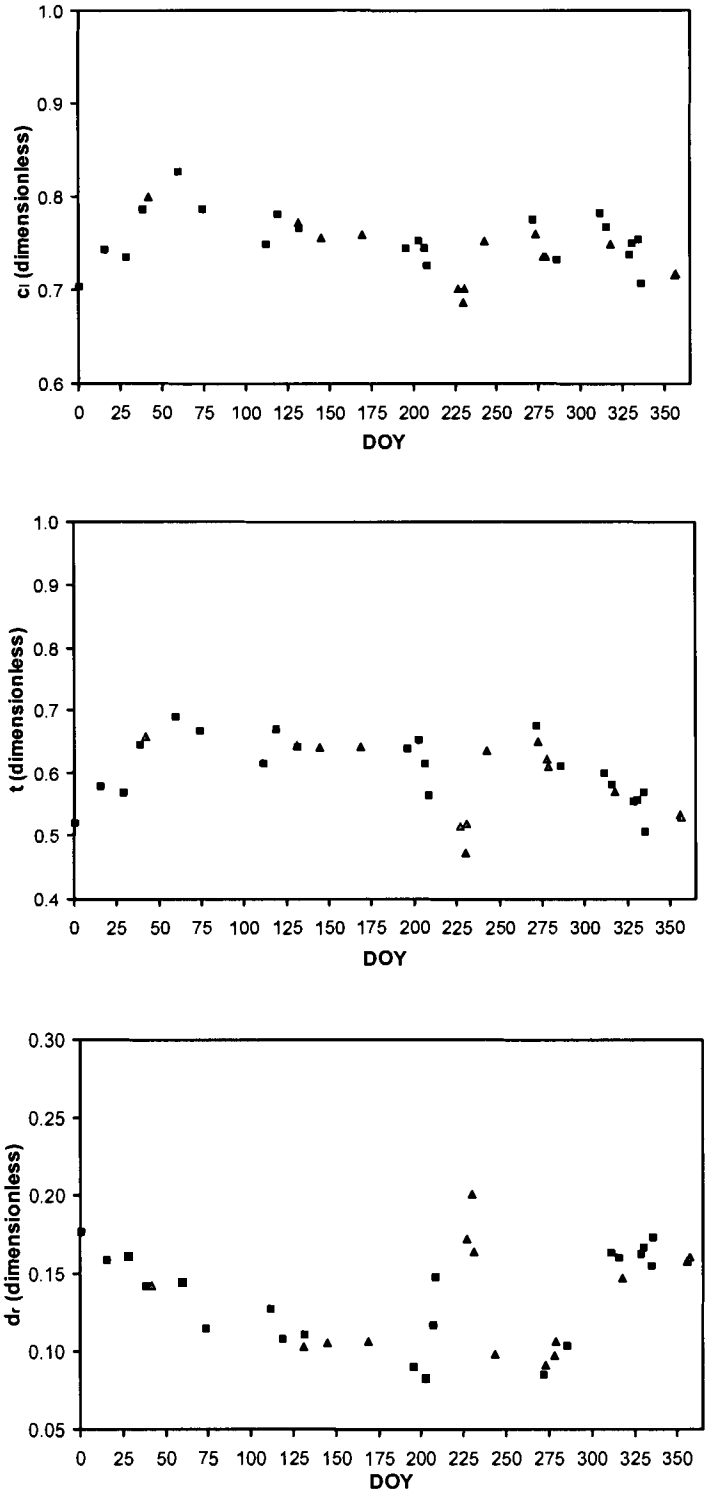

Figure 2.5. Daily clearness index, transmissivity and diffuse ratio values for cloudless full (▲) and cloudless half days (■) in 2003 at the Bratt's Lake Observatory. Note the change in scale for the diffuse ratio, and the presence of pyrogenic aerosols on DOY 209, 227, 230 and 231.

index and transmissivity increase from 0.70 and 0.52 respectively on DOY 1 to 0.79 and 0.67 on DOY 74 (Table A5.3). Alternately, the diffuse ratio decreases from 0.18 on DOY 1 to 0.11 on DOY 74. These changes are primarily the result of changing optical air mass. With increasing DOY (until the summer solstice), atmospheric attenuation generally decreases in response to decreasing average daily values of optical air mass. Throughout much of the spring and summer, the pattern observed in the clearness index, transmissivity and diffuse ratio are more constant.

By early autumn, a decreasing trend is apparent in the clearness index and transmissivity. The clearness index and transmissivity decrease from 0.78 and 0.67 respectively on DOY 272 to 0.72 and 0.53 on DOY 357 (Table A5.3). Alternately, daily diffuse ratio values increase over this period, from 0.09 on DOY 272 to 0.16 on DOY 357. These changes are attributable to increasing average daily values of optical air mass (until the winter solstice). Large optical air mass values result in increased absorption and scattering of extraterrestrial irradiance, ultimately lowering the clearness index and transmissivity, and increasing the diffuse ratio.

Pyrogenic aerosols affect irradiance by enhancing normal atmospheric scattering and absorption levels. As such, the radiative signature of these aerosols is a decrease in the clearness index and transmissivity, and an increase in the diffuse ratio. The second distinct deviation of the clearness index, transmissivity and diffuse ratio from their average annual values occurred on DOY 209, 227, 230 and 231 (Figure 2.5). On these days, the aerosol effects are distinct, causing the clearness index and transmissivity to drop to 0.69 and 0.47 respectively on DOY 230. This represents an 8.0 and 21.7 % decrease in the clearness index and transmissivity respectively, relative to their annual averages. The enhanced atmospheric scattering from the pyrogenic aerosols caused the diffuse ratio to spike as high as 0.20 on DOY 230. This spike in the diffuse ratio represents a 53.5 % increase relative to the annual average.

Unlike during the winter and autumn, the changes to the clearness index, transmissivity and diffuse ratio on the four aerosol days are not attributable to optical air mass. For example, in Figure 2.5, note how daily clearness index, transmissivity and diffuse ratio values immediately before and after the aerosol event are significantly closer to the average annual values of 0.75, 0.60 and 0.13 respectively. Figure 2.6 also supports

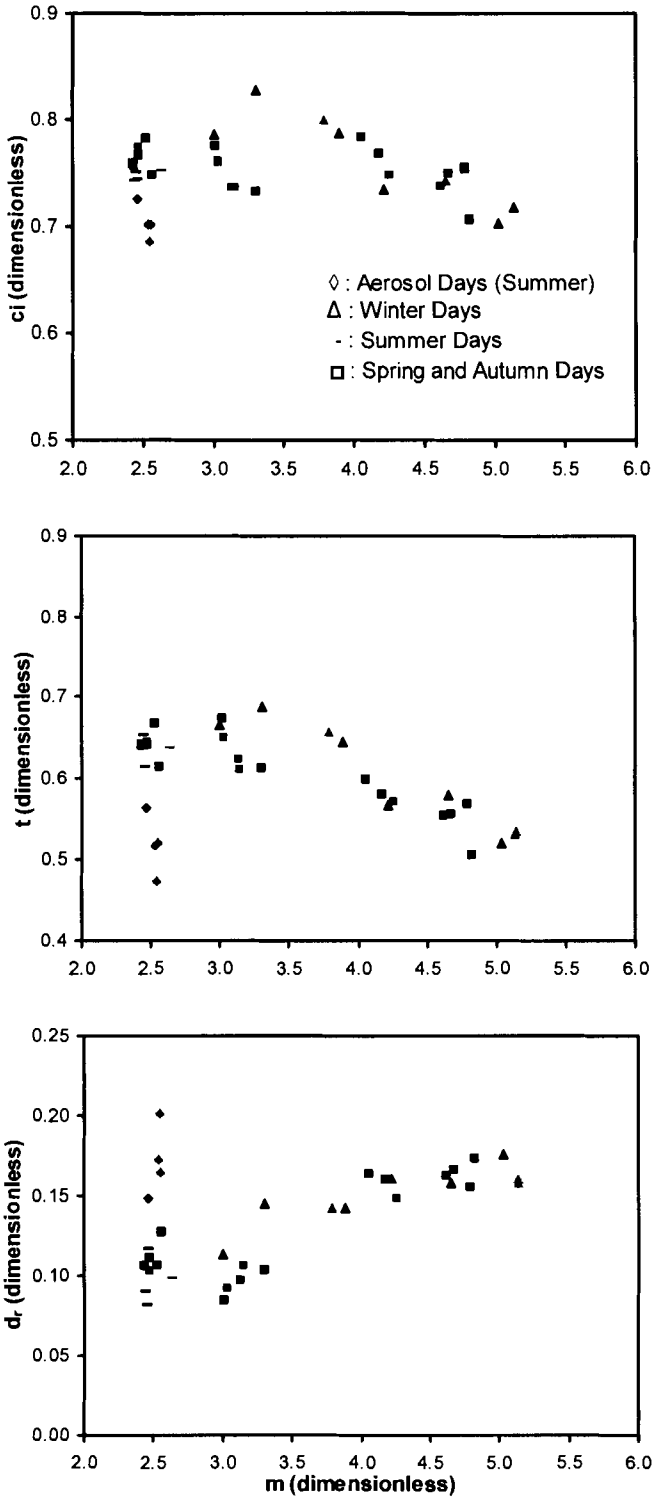

Figure 2.6. Daily clearness index, transmissivity and diffuse ratio vs. average daily optical air mass ($z < 85°$). Cloudless full and half days are represented in grey and black respectively. Note scale change between figures.

this conclusion. In Figure 2.6, the clearness index, transmissivity and diffuse ratio are plotted against the average daily optical air mass (calculated from one-minute optical air mass values when $z < 85°$). For approximately the same optical air mass (≈ 2.5), distinctly lower clearness index and transmissivity values and higher diffuse ratio values are observed on the four days in which pyrogenic aerosols are present. Figure 2.6 also shows that as optical air mass increases (i.e. from lowest in summer to highest in winter), the daily clearness index and transmissivity decrease while the daily diffuse ratio increases.

2.5.2. Observed Diurnal Cloudless Sky Broadband Global Irradiance Regime

The diurnal cloudless sky global irradiance regime is examined using one-minute data. This regime exhibits a definite repeatable trend that is clearly dependent on solar zenith angle. During cloudless days, global, direct and diffuse irradiance regimes show symmetry about solar noon (Figure 2.7). Maximum global, direct and diffuse irradiance values occur at solar noon as the Sun reaches its diurnal apex (i.e. smallest zenith angle). The cloudless half day plots of global, direct and diffuse irradiance show a lack of symmetry however, with fluctuations occurring in those forenoon or afternoon periods in which cloud was present (Figure 2.7). While this cloud-induced asymmetry negates a day from being categorized as cloudless, cloudless half days can be modified into artificial cloudless full days. By calculating the irradiance received at the surface during a cloudless forenoon or afternoon period in MJ m^{-2} half day^{-1}, the irradiance received at the surface during a cloudless full day can be simulated by multiplying this half day irradiance total by two.

The symmetry, or lack thereof, observed in the diurnal irradiance plots of Figure 2.7 is also present in the diurnal one-minute plots of the clearness index, transmissivity and the diffuse ratio. From Figure 2.7, it is apparent that the transmissivity and clearness index behave similarly on cloudless days, with both parameters showing symmetry about a peak ratio value at solar noon (Figure 2.7). Conversely, the diffuse ratio shows symmetry about a diurnal low value, which also occurs at solar noon (Figure 2.7). These two patterns occur as attenuation levels change due to diurnal changes in atmospheric path length (i.e. optical air mass). The increase in attenuation at high optical air mass

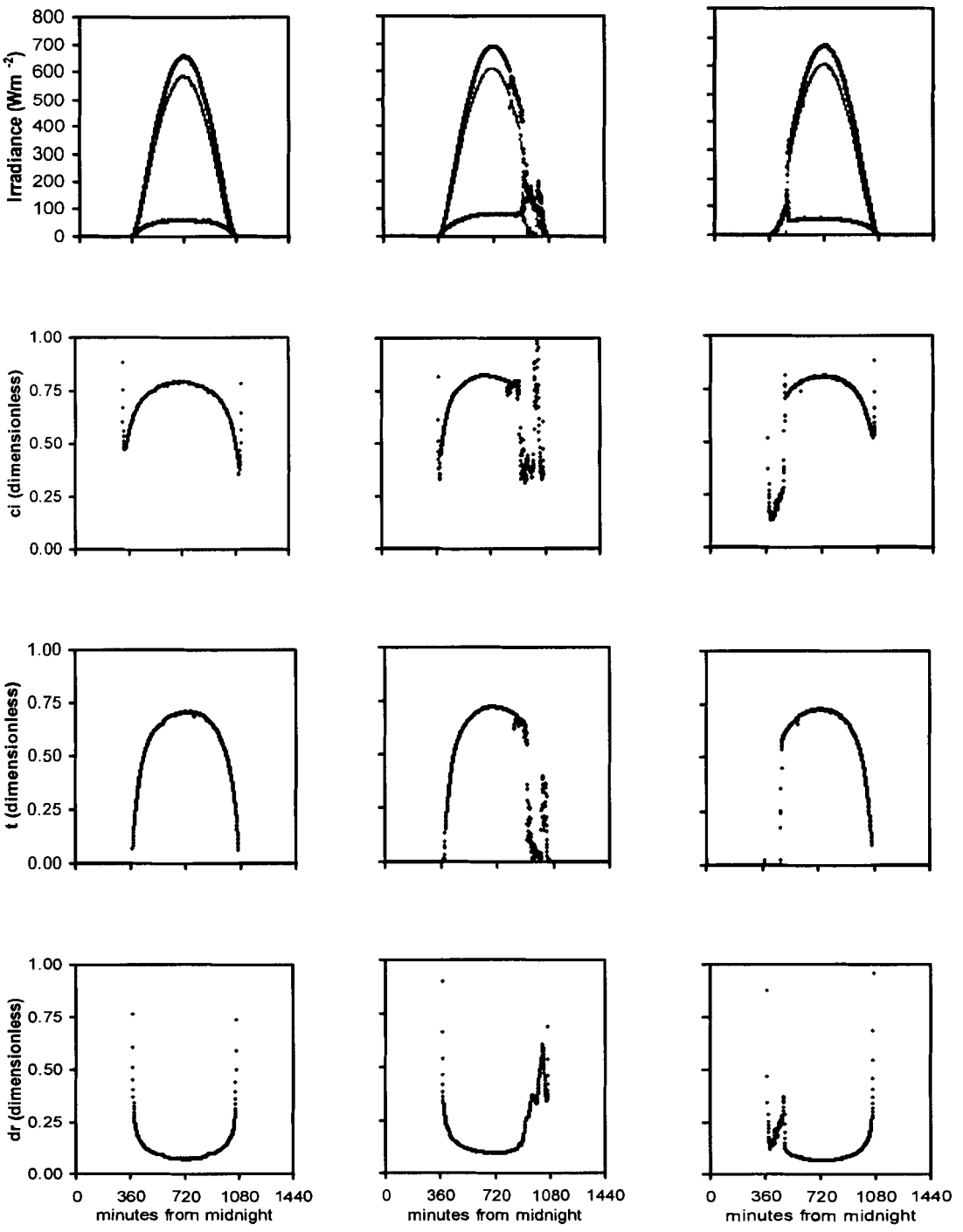

Figure 2.7. The diurnal trend of one-minute global, direct and diffuse irradiance, corresponding transmissivity (t), clearness index (c_i) and diffuse ratio (d_r) values. Near perfect symmetry exists for cloudless full days and distinct asymmetry is observed when cloud is present.

results in relatively small transmissivity and clearness index values, and relatively large diffuse ratio values (Figure 2.7). Alternately, as optical air mass decreases towards a diurnal minimum at solar noon, the amount of attenuation decreases, resulting in relatively large transmissivity and clearness index values, and small diffuse ratio values.

Upon scrutiny of diurnal trends in the clearness index, transmissivity and diffuse ratio, it is apparent that global, direct and diffuse irradiance are not perfectly symmetrical about solar noon, even on cloudless days. This asymmetry indicates differences in atmospheric attenuation from forenoon to afternoon periods; which is likely due to changes in surface convection, and the advection of aerosols. Aerosol optical depths often rise during the afternoon in response to increased surface constituents (i.e. dust) being lifted into the atmosphere through convective turbulence. Larger aerosol optical depths then lead to increased attenuation and diurnal asymmetry in the clearness index, transmissivity and diffuse ratio. Secondly, the advection of aerosols from distant upwind wildland fires or air masses of tropical origin may also be responsible for the observed diurnal asymmetry at the Observatory.

2.5.3. Modelling Cloudless Sky Global Irradiance

For each of the 35 cloudless days identified in 2003, the Houghton (1954) model was applied to estimate one-minute global, direct and diffuse irradiance. While originally intended for estimating seasonal irradiance over large areas, the Houghton model performs well at predicting global irradiance at individual locations over daily and monthly periods (Davies *et. al.*, 1975; Monteith, 1962; Idso, 1970). Specifically, the direct beam is calculated from equation 2.16, the diffuse irradiance from equation 2.17 and the global irradiance from equation 2.18. The transmittance functions are given in equations 2.19 to 2.24. Houghton's (1954) treatment of aerosols is through the factor k, hence

$$\phi_d = \phi_{da}\,\phi_{ds} = k^m = e^{-\tau_a m} \quad . \tag{2.35}$$

By definition, the factor k is the exponential of the aerosol optical depth. From equation 2.19, Houghton treats k as a constant (k = 0.95). This corresponds to an aerosol optical depth of 0.051.

It is important to note that equation 2.17 is correct only for the diffuse irradiance over a surface with zero albedo and therefore does not account for multiple reflections between the ground and the atmosphere. Neglecting multiple reflections will lead to model underestimation of the diffuse irradiance. This effect can be large during the winter months with a snow surface or when aerosol optical depths are large.

Figure 2.8 is a diurnal plot of observed and predicted global, direct and diffuse irradiance for a late spring (DOY 169) and early autumn (DOY 273) day. The agreement between modelled and measured global and direct irradiance is excellent, with all modelled values falling within ± 5 percent of the measured. The 1:1 plots corresponding to Figure 2.8 are presented in Figure 2.9. For the diffuse irradiance, model inaccuracy is on the order of 5 percent.

During the late spring, summer (pyrogenic aerosols are absent) and early autumn, model accuracy is high because Houghton's dust factor (i.e. $k = 0.95$ or $\tau_a = 0.051$) is a good approximation of background aerosol concentrations in southern Saskatchewan (i.e. average $\tau_a = 0.060$). However, during periods when the aerosol optical depth is larger than average (i.e. $\tau_a = 0.102$ on spring day DOY 131), irradiance estimates prove less accurate. Specifically, the increased aerosol optical depth results in an overestimation of direct irradiance and underestimation of diffuse irradiance (Figure 2.10). The net effect in terms of the global irradiance is a slight overestimation.

Deterioration in model accuracy occurred primarily during two periods in 2003: 1) during the winter and late autumn, and 2) during the mid-summer pyrogenic aerosol period. During the winter and late autumn in southern Saskatchewan, the amount of aerosols in the atmosphere is minimal, due in large part to the frozen and or snow covered surface that dominates the landscape during these times. Furthermore, southern Saskatchewan experiences regular periods of high pressure during the winter season. The subsiding nature of atmospheric high-pressure systems tends to suppress surface materials like dust from rising high into the atmosphere. As previously discussed, Houghton's expression for the diffuse flux does not include the effects of surface albedo. The implications of this modelling assumption will be an underestimate of the diffuse flux.

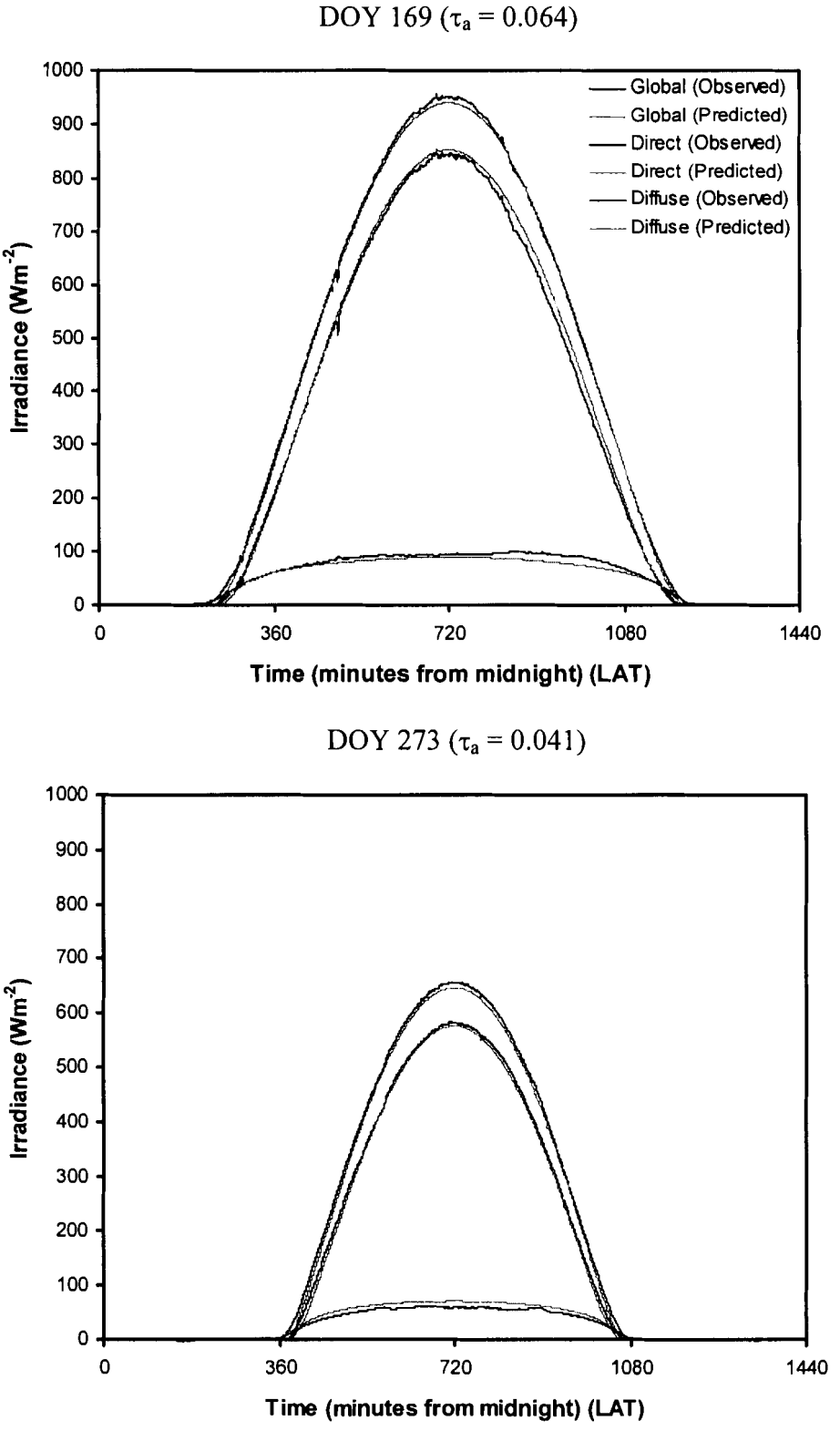

Figure 2.8. Diurnal trends of observed and predicted global, direct and diffuse irradiance on two cloudless days (DOY 169 and DOY 273).

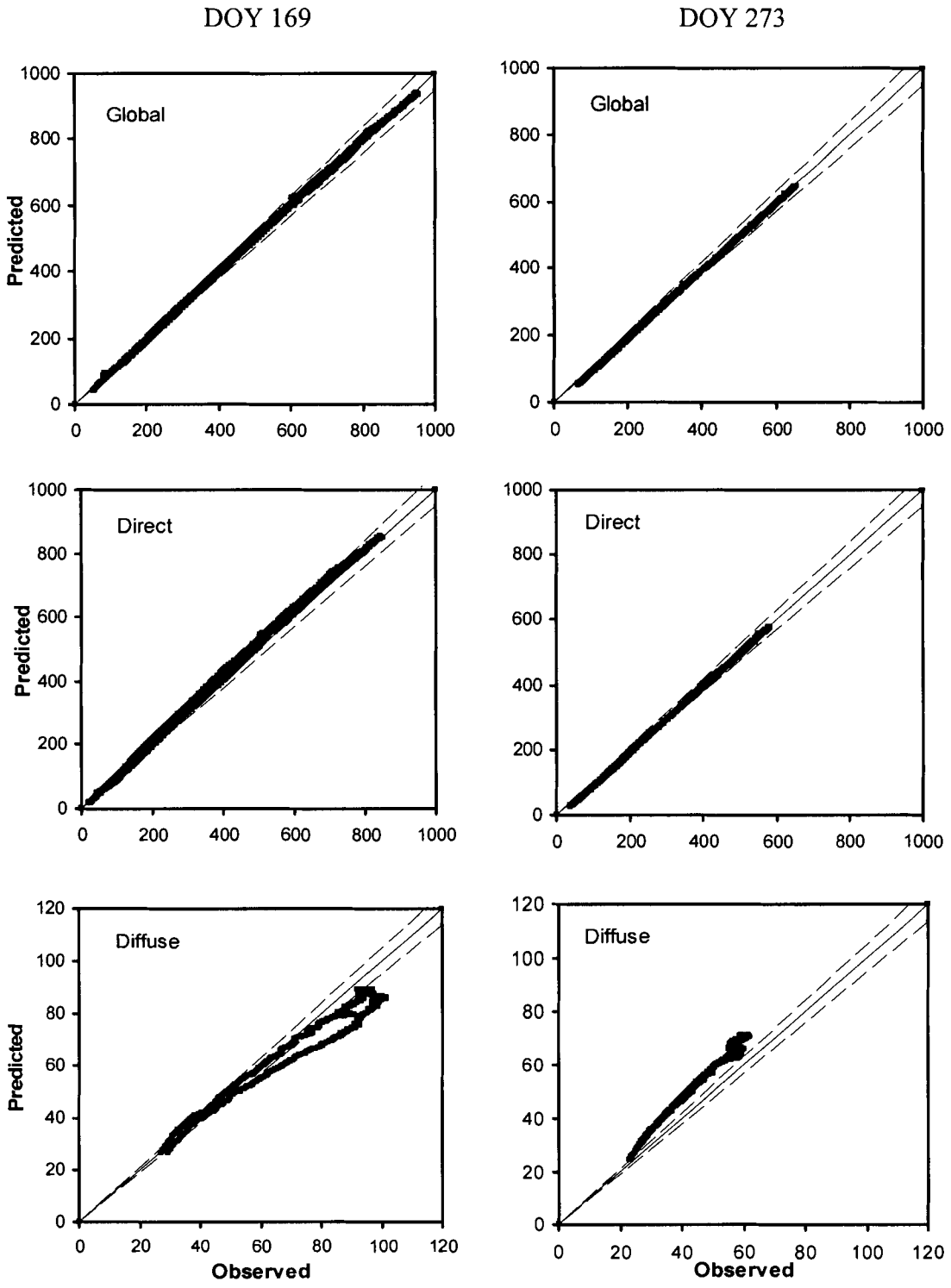

Figure 2.9. Predicted and observed one-minute global, direct and diffuse irradiance on two cloudless days (DOY 169 and DOY 273) for $z < 85°$. The units are in Wm^{-2}. Dashed lines represent ± 5 % deviation from the 1:1 line.

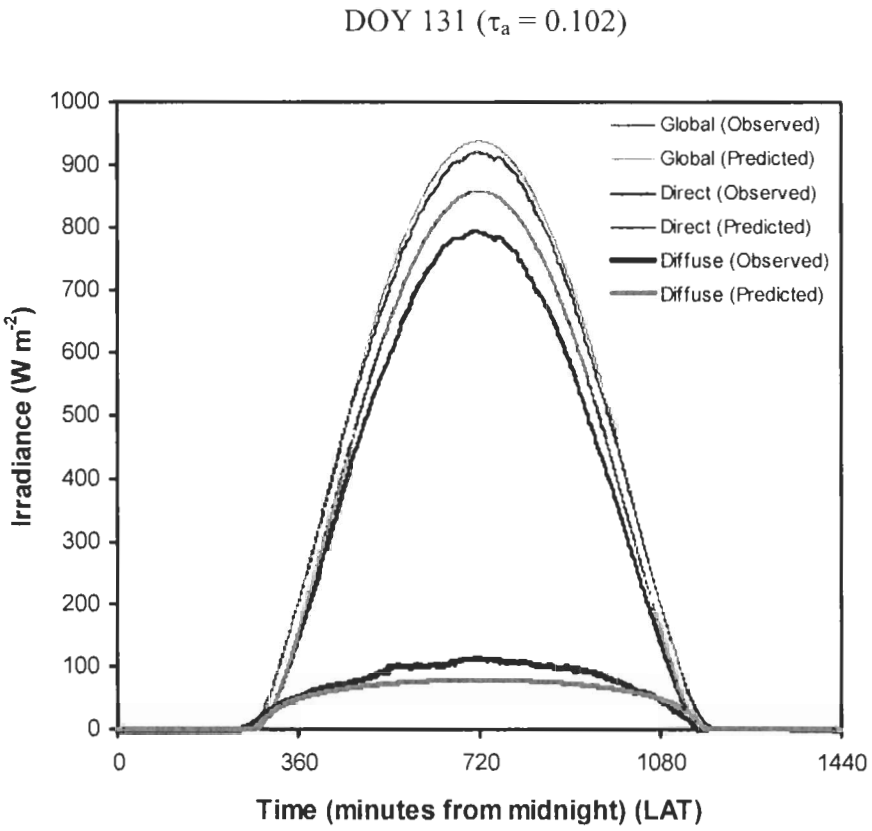

Figure 2.10. Diurnal trends of observed and predicted global, direct and diffuse irradiance on cloudless day DOY 131.

The model's aerosol parameterization (i.e. $\phi_{da} = \phi_{ds} = 0.975^{m}$) assumes that aerosols are present (with concentrations remaining constant) over land at all latitudes throughout the year (Monteith, 1962). As discussed above and shown in section 2.4, this assumption represents a major source of error as constant aerosol concentrations within the atmosphere are not representative of conditions throughout Canada's prairie environment. While aerosols are present within the atmosphere during all parts of the year, due in large part to lifting and transportation by local and regional winds, reduced aerosol concentrations are more common during colder months.

Figure 2.11 is a diurnal irradiance plot for two winter days (i.e. DOY 42 and DOY 357) in 2003. On both days, it is apparent that model estimates of global and direct irradiance are noticeably lower than measured values. This deficiency is primarily attributable to Houghton's assumption of constant atmospheric aerosol concentrations

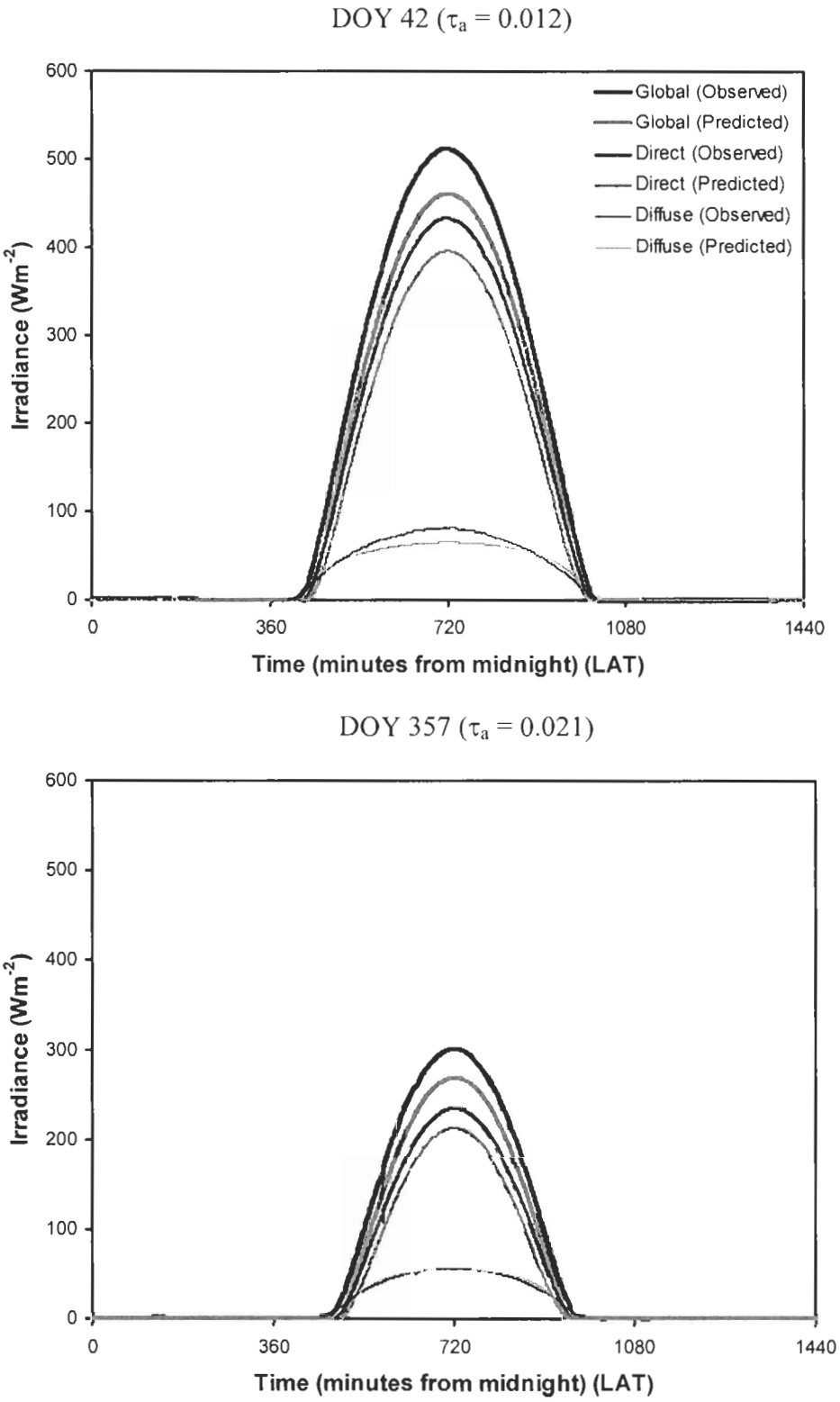

Figure 2.11. Diurnal trends of observed and predicted global, direct and diffuse irradiance on two cloudless days (DOY 42 and DOY 357).

and the neglect of multiple reflections. Figure 2.12, which contains the 1:1 plots for DOY 42 and DOY 357, shows that predicted global and direct irradiance fall short of their observed counterparts, with all data points falling below the 1:1 line. While model estimation of diffuse irradiance on DOY 42 was better than expected, deviation from the 1:1 line is attributable to the absence of calculations to correct for multiple reflections.

During the summer of 2003, aerosol optical depth in southern Saskatchewan increased due to the presence of pyrogenic aerosol plumes. The increase in atmospheric aerosol concentration on several cloudless days in late July and August resulted in large differences between estimated and observed global, direct and diffuse irradiances. The increased absorption and scattering from pyrogenic aerosols caused reductions in direct irradiance at the surface. The enhanced scattering from these aerosols caused an increase in the diffuse irradiance. Due to Houghton's constant aerosol parameterization, model estimates were unable to account for the changes in atmospheric attenuation caused by the pyrogenic aerosols. As such, the model overestimated the global and direct beam irradiance and underestimated the diffuse irradiance. Monteith (1962) also identified similar differences between Houghton model estimates and observations of global, direct and diffuse irradiance in the presence of aerosols.

Figure 2.13 shows the difference between predicted and observed one-minute irradiance values during two summer days in which pyrogenic aerosols are present. The model overestimates global and direct irradiance and underestimates the diffuse irradiance. The 1:1 comparative plots corresponding to Figure 2.13 are presented in Figure 2.14. By fitting a linear trend to the 1:1 plots of one-minute observed and predicted irradiance data, the slope of the trend line provides an indication of the amount of pyrogenic aerosol attenuation within the atmosphere (Table 2.3). The percentage decrease in global irradiance suggests that pyrogenic aerosols initiated a maximum 3.4% negative shortwave forcing within the atmosphere. The large percentage increase in diffuse irradiance suggests that while there is absorption by the aerosols, a significant amount of direct beam irradiance is also scattered.

Figure 2.15 provides a graphical comparison of observed and predicted daily irradiance totals. From Figure 2.15, both model predictions and observed values display

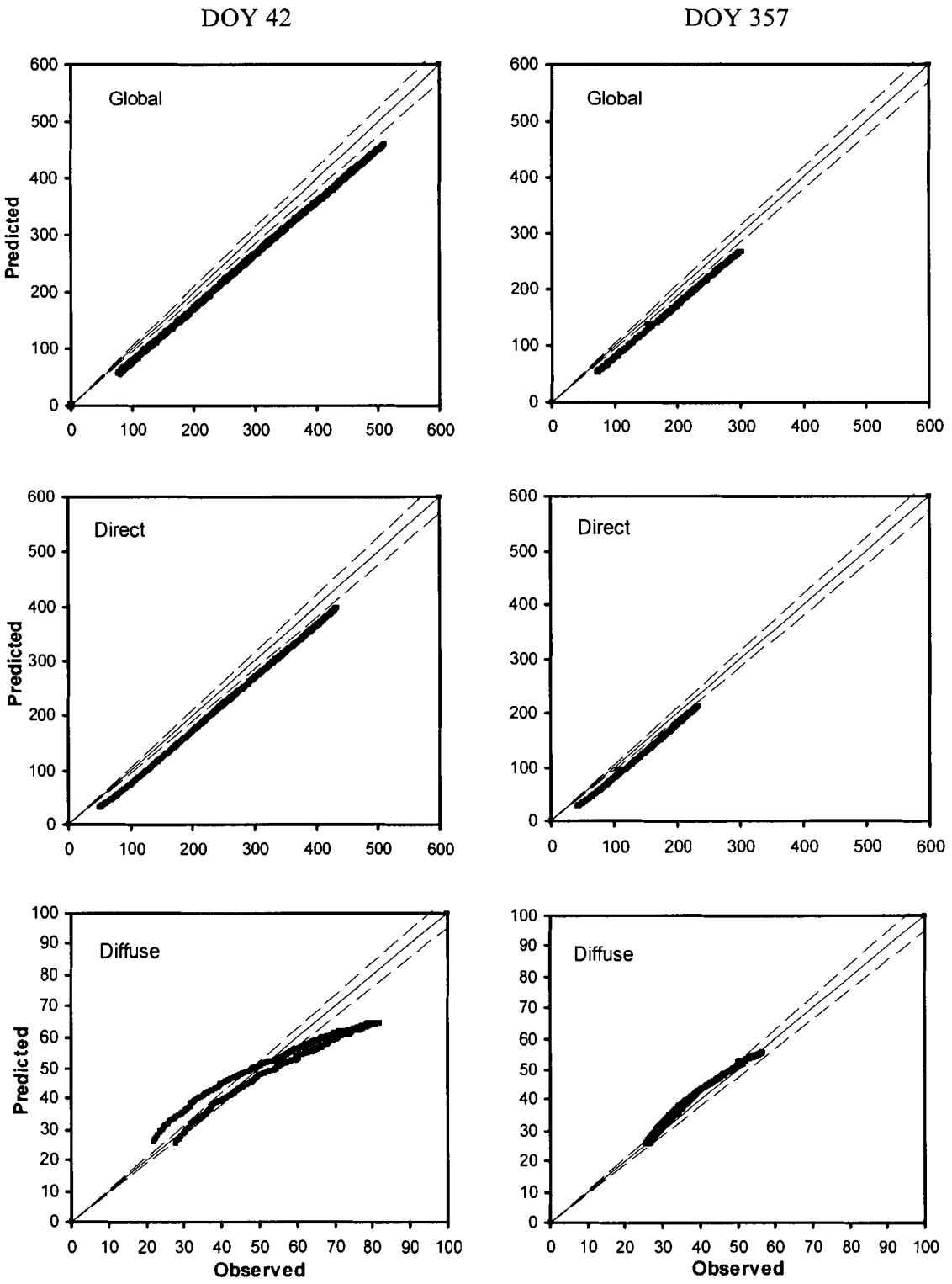

Figure 2.12. Predicted and observed one-minute global, direct and diffuse irradiance on two cloudless days (DOY 42 and DOY 357) for $z < 85°$. The units are in Wm^{-2}. Dashed lines represent ± 5 % deviation from the 1:1 line.

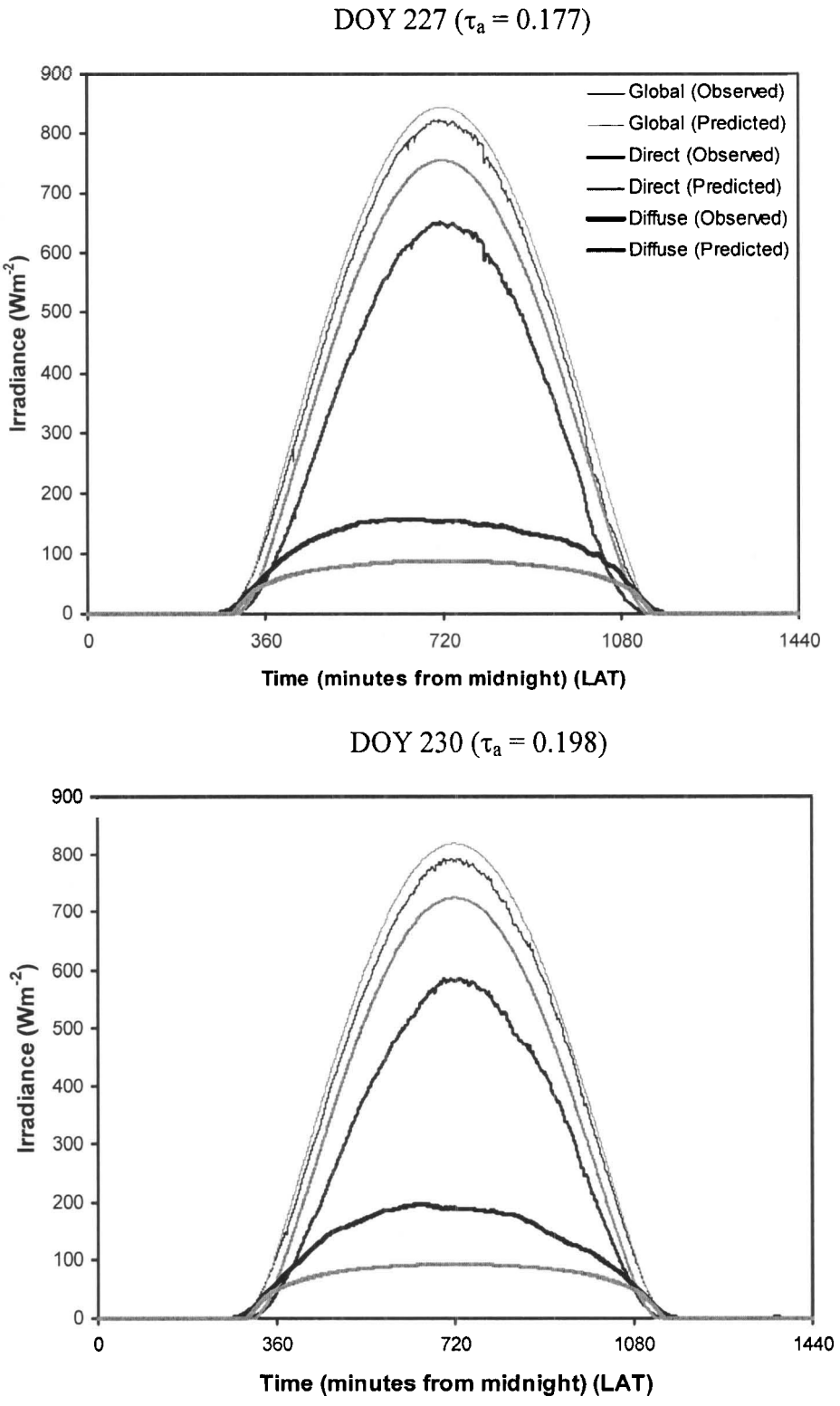

Figure 2.13. Diurnal trends of observed and predicted global, direct and diffuse irradiance on two cloudless days in which pyrogenic aerosols were present (DOY 227 and DOY 230).

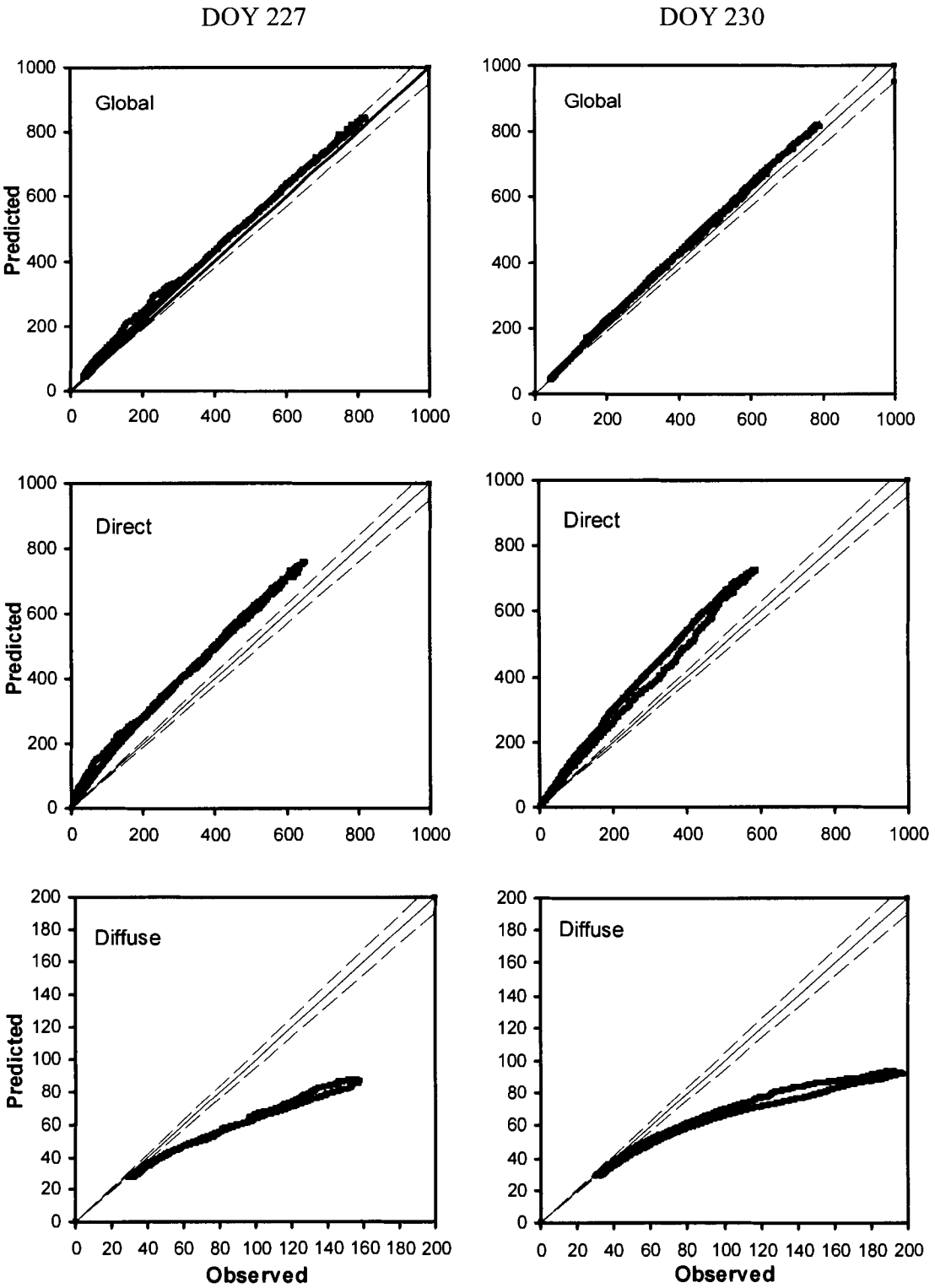

Figure 2.14. Predicted and observed one-minute global, direct and diffuse irradiance on two cloudless days (DOY 227 and DOY 230) for $z < 85°$. The units are in Wm^{-2} and pyrogenic aerosols are present in the atmosphere. Dashed lines represent ± 5 % deviation from the 1:1 line.

Table 2.3. Percentage increase or decrease in global, direct and diffuse irradiance by pyrogenic aerosols on three cloudless full and one cloudless half day in 2003. Percentage change is derived from the slope of the regression line applied to 1:1 plots of predicted and observed global, direct and diffuse irradiance on DOY 209, 227, 230 and 231. The * indicates the cloudless half day.

	Percentage change (%) in broadband irradiance		
DOY	Global	Direct	Diffuse
209*	- 2.5	- 11.7	+ 50.2
227	- 0.2	- 10.5	+ 44.3
230	- 3.4	- 23.1	+ 32.6
231	- 2.3	- 13.3	+ 49.7
Average	- 2.1	- 14.7	+ 44.2

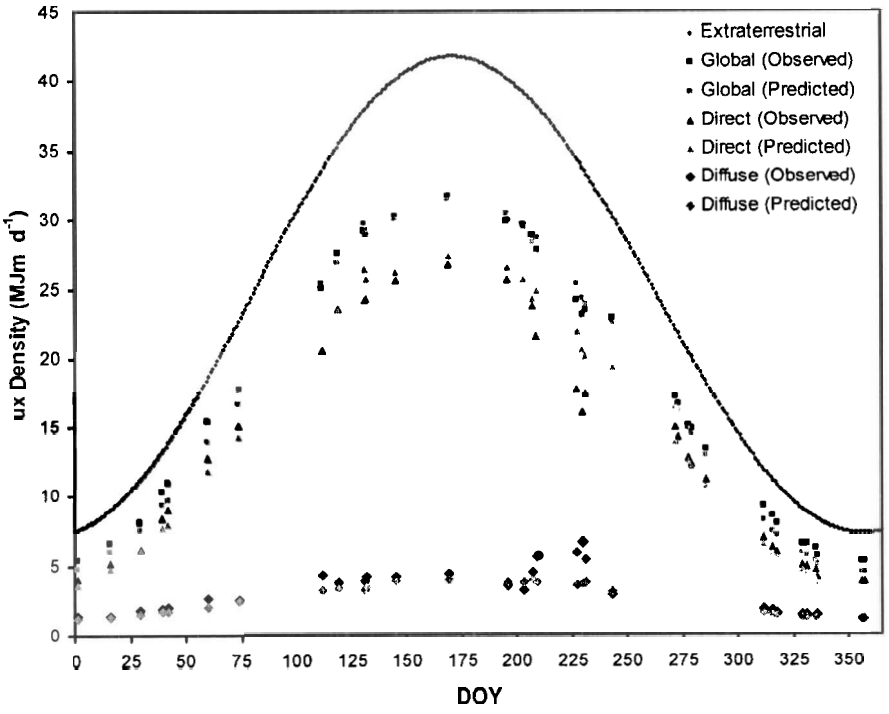

Figure 2.15. Cloudless-sky observed and predicted global, direct and diffuse irradiance regimes for 2003.

the same seasonal regimes. Upon closer analysis, the major differences between predicted and observed daily values of global and direct irradiance occur largely during two aforementioned periods: 1) the winter and late autumn, and 2) the mid-summer pyrogenic aerosol event. For example, Figure 2.16 shows that the greatest percent difference of predicted from observed global and direct irradiance occurs during these two periods. However, when examining a plot of the percent difference between predicted and observed diffuse irradiance (Figure 2.17) relatively large percent differences, greater than 10 percent, are found to occur throughout all seasons.

Other statistical methods exist which can provide a more meaningful assessment of model performance. These statistical techniques include the mean bias error (MBE), mean absolute error (MAE), root mean square error (RMSE) and index of agreement (d) (Willmott, 1982) (Appendix 5). If perfect agreement between predicted and observed values exist the MBE, MAE and RMSE will equal zero and d will equal one. Tables A5.5, A5.6 and A5.7 contain comparative data for each of the 14 cloudless full and 21 cloudless half days in 2003. The results shown in Tables A5.5, A5.6 and A5.7 further confirm the discussion of model performance given in the previous section.

From Tables A5.5 and A5.6, model estimates prove less accurate during winter, early spring and late fall periods (i.e. generally larger values for the MBE, MAE, and RMSE are observed during these times). For example, comparison statistics for global irradiance data result in a wintertime range in RMSE values between 17.1 W m^{-2} and 41.7 W m^{-2}. This can be contrasted against summertime RMSE values that range between 7.6 W m^{-2} and 11.9 W m^{-2} (note: RMSE values for DOY 209, 227, 230 and 231 are excluded here due to the influences of pyrogenic aerosols). Furthermore, for winter and late autumn periods, note that the model generally underestimates global irradiance (i.e. negative values for the MBE). These results indicate a need to adjust the model's current aerosol parameterization in order to account for the clean prairie atmosphere during colder months of the year (i.e. during the winter, early spring and late autumn).

The data given in Tables A5.5 and A5.6 also highlight the inaccuracy of model estimates during the summer pyrogenic aerosol event (i.e. the relatively large MBE, MAE, RMSE values that occur on DOY 209, 227, 230 and 231). For example, RMSE

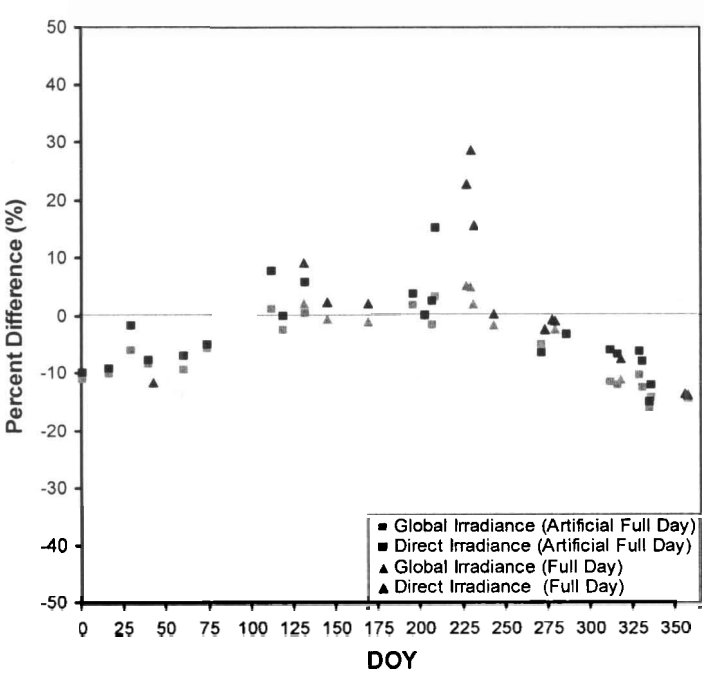

Figure 2.16. Percent difference of predicted global and direct irradiance (MJ m^{-2} d^{-1}) from their observed counterparts (MJ m^{-2} d^{-1}) for the 14 cloudless full and 21 artificial full days in 2003.

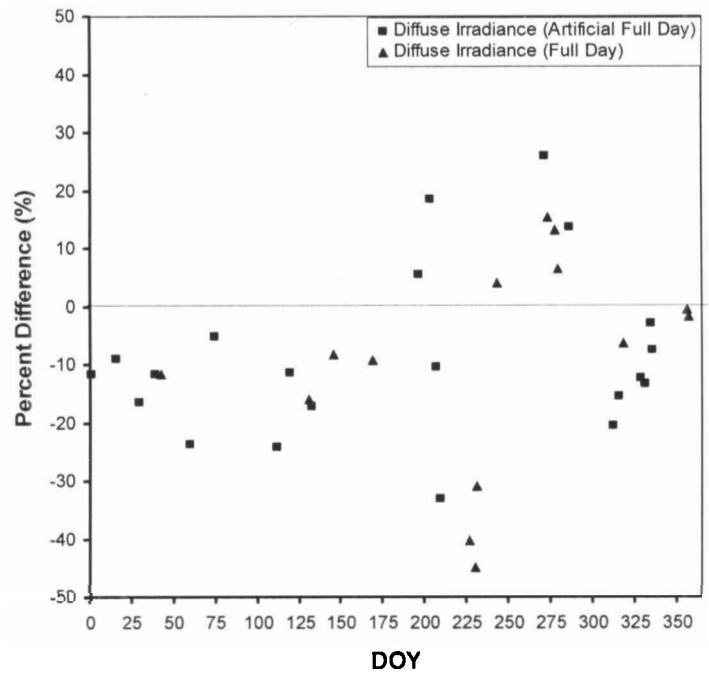

Figure 2.17. Percent difference of predicted diffuse irradiance (MJ m^{-2} d^{-1}) from the observed diffuse irradiance (MJ m^{-2} d^{-1}) for the 14 cloudless full and 21 artificial full days in 2003.

values calculated from global irradiance data on these four pyrogenic aerosol days ranges from 12.0 W m^{-2} to 26.3 W m^{-2}, higher than RMSE values on all other summertime cloudless days. Also, note the positive MBE values on these aerosol days, indicating model overestimation of global irradiance.

The comparison statistics calculated for the direct irradiance on DOY 209, 227, 230 and 231 (Table A5.6) illustrate a similar situation. RMSE values on these four days range from 63.3 W m^{-2} to 106.4 W m^{-2}. Alternately, the RMSE values calculated on all other summer days are considerably lower, ranging from 8.95 W m^{-2} to 21.1 W m^{-2}. This inaccuracy also appears in the comparison statistics calculated from the diffuse irradiance (Table A5.7). Specifically, RMSE values range from 37.9 W m^{-2} to 69.4 W m^{-2}. By comparison, RMSE values calculated for all other summer days only range from 4.5 W m^{-2} to 12.3 W m^{-2}. Furthermore, note the strong negative values for the MBE on DOY 209, 227, 230, and 231, indicating model underestimation of diffuse irradiance, an effect caused by enhanced atmospheric scattering by the pyrogenic aerosols.

Table 2.4 summarizes model performance with MBE, MAE, RMSE and d values calculated from one-minute measured and modelled global, direct and diffuse irradiance data on all 35 cloudless days in 2003. Furthermore, these statistics were also calculated for all measured and modelled one-minute irradiance values during cloudless winter (DOY 356 – 78), summer (without pyrogenic aerosols) (DOY 172 – 265) and pyrogenic aerosol (DOY 209, 227, 230 and 231) days (Table 2.4). The data presented in Table 2.4 not only confirms the previous assessment of model accuracy but also correlates well with the statistical data presented in Appendices A5.5, A5.6 and A5.7. From Table 2.4, it is evident that model estimates of global, direct and diffuse irradiance are relatively close to their observed counterparts throughout 2003, but are particularly accurate for summer days. Alternately, model estimates show a greater deviation from their observed counterparts during winter days, and days in which pyrogenic aerosols are present.

2.5.4. Re-Evaluation of the Dust Factor in the Houghton Model

Across the Earth, the concentration of aerosols within the atmosphere is variable over time. In the atmosphere, the total irradiance attenuation from aerosols (i.e. dust) can

Table 2.4. Comparison statistics for one-minute measured and modelled global, direct and diffuse irradiance in 2003. MBE (W m^{-2}), MAE (W m^{-2}), RMSE (W m^{-2}) and d (dimensionless) values are calculated for all 35 cloudless full and half days in 2003 (total), and days falling into winter (DOY 356 – 78), summer (DOY 172 – 265) and pyrogenic aerosol periods (DOY 209, 227, 230 and 231).

	Global				Direct				Diffuse			
	Total	Winter	Summer	Aerosol	Total	Winter	Summer	Aerosol	Total	Winter	Summer	Aerosol
MBE (Wm^{-2}):	0.35	-24.77	7.69	26.91	11.43	-19.46	5.65	74.96	-10.74	-5.63	2.33	-44.72
MAE (Wm^{-2}):	17.46	24.77	12.27	28.13	26.50	19.53	12.49	75.08	14.67	6.81	7.40	44.72
RMSE (Wm^{-2}):	21.51	27.72	15.07	31.37	39.86	21.26	14.96	84.84	23.95	10.08	9.04	52.27
d (dimensionless):	0.9995	0.9980	0.9998	0.9992	0.9978	0.9983	0.9998	0.9915	0.9715	0.9911	0.9959	0.9323

be evaluated by employing one-minute estimates from an aerosol free version of the Houghton model (i.e. k = 1.0) and one-minute observations of cloudless sky direct irradiance. From equations 2.3, 2.19 and 2.29, the dust factor can be determined as

$$\phi_d = k^m = e^{-\tau_a m} \tag{2.36}$$

$$k = e^{-\tau_a} \quad . \tag{2.37}$$

From equation 2.37, one-minute values of the dust factor were calculated. Employing a weighted average (i.e. weighted to the direct irradiance), a single dust factor value representative of an entire cloudless full or one-half day was calculated (Figure 2.18). The annual range in dust factor values for southern Saskatchewan is characterized by winter maxima and summer minima (Figure 2.18). During colder periods (i.e. winter, early spring and late autumn), dust factor values closer to unity are expected (i.e. reduced aerosol concentrations) while warmer periods (i.e. late spring, summer and early autumn) are generally characterized by smaller dust factor values (i.e. enhanced aerosol concentrations) then suggested by Houghton (Figure 2.18).

The general absence of dust factor values during the early spring and middle of autumn (Figure 2.18) is largely attributable to unstable atmospheric conditions above the Observatory. The unsettled weather conditions occur due to the movement of the northerly jet stream (mean storm track), northward in the spring, and southward in the autumn (Phillips, 1990). As the jet stream acts as a rough boundary between generally colder and drier air masses to the north, and warmer and moister air masses to the south, its movement high within the atmosphere often coincides with the formation of cloud and precipitation at lower altitudes.

From Figure 2.18, it is apparent that calculated dust factor values during winter and late autumn are distinctly different from Houghton's original parameterization of 0.95. The difference is the result of a clean prairie atmosphere (i.e. low aerosol concentrations), which is characteristic of the region during colder periods of the year. This deficiency contributes to the relative inaccuracy of model estimates during the winter and late autumn. Alternately, calculated dust factor values for late spring, summer

and early autumn days are notably closer to Houghton's original parameterization of 0.95. This result largely accounts for improved model accuracy during these times.

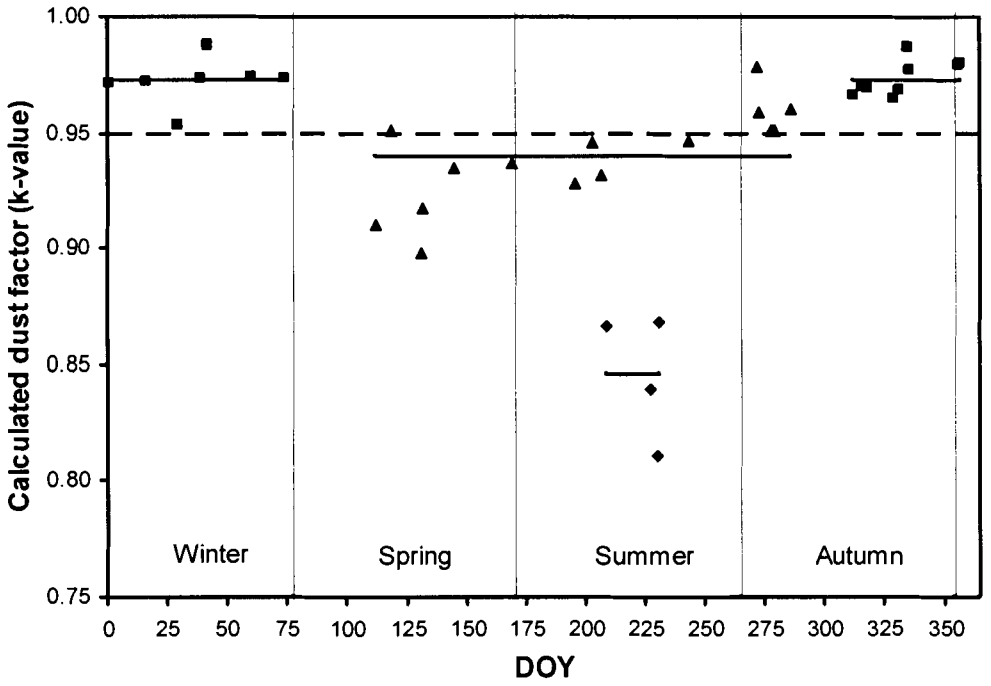

Figure 2.18. Calculated dust factors for cloudless full and half days. Average dust factor values (0.973, 0.940 and 0.846) for the three distinct periods (▲ for spring, summer and early autumn, ■ for winter and late autumn and ♦ for summer periods in which pyrogenic aerosols are present) are denoted by the solid horizontal lines. The dashed horizontal line denotes the dust factor value employed by Houghton.

The four dust factor values furthest from Houghton's original value (i.e. on DOY 209, 227, 230 and 231) are attributable to the presence of pyrogenic aerosols. The distinct effect of pyrogenic aerosols on the dust factor is largely responsible for the uncharacteristic disagreement of model estimates with measured irradiances during the summer.

In response to the aforementioned inadequacies of Houghton's dust factor value, Figure 2.18 presents a revised aerosol parameterization. After dividing dust factor values into three groups: 1) winter and late autumn, 2) spring, summer and early autumn and 3)

summer with pyrogenic aerosols, three average k-values were calculated. For the winter and late autumn, the average dust factor approached unity at 0.973. This value more accurately represents dust attenuation levels within the prairie atmosphere during colder periods of the year.

The average dust factor for spring, summer and early autumn days was equal to 0.940. Although only slightly lower than Houghton's original parameterization of 0.95, this value better approximates aerosol attenuation levels within the prairie atmosphere during warmer periods of the year. Finally, the average dust factor for summer days in which pyrogenic aerosols were present is 0.846. Despite the obvious inadequacies of using a constant aerosol parameterization for the estimation of cloudless sky irradiance, it is apparent that Houghton's original dust factor is reasonable for late spring, summer (without pyrogenic aerosols) and early autumn periods at the Observatory.

2.6. Conclusions

There were three major objectives for this chapter: 1) to examine aerosol optical depth in southern Saskatchewan for cloudless days in 2003, 2) to examine seasonal and diurnal global, direct and diffuse irradiance regimes using one-minute data and 3) to assess the accuracy of one-minute estimates of cloudless sky global, direct and diffuse irradiance from the Houghton (1954) model. In the absence of pyrogenic aerosols, the seasonal cycle of τ_a for southern Saskatchewan displayed a winter minimum and spring maximum. Due to the rural agricultural location of the Observatory, this cycle is dependant on atmospheric concentrations of dust, which are low in the winter and higher in the spring. During the summer of 2003, pyrogenic aerosol plumes caused τ_a to increase dramatically on several days. During the four days when pyrogenic aerosols were present, average daily values of τ_a were larger than on all other cloudless days in 2003. Furthermore, the pyrogenic aerosols caused significant diurnal variability in τ_a, an effect observed at other locations in both eastern and western Canada (Markham *et al.*, 1997; Gutro *et al.*, 2002). In the present study, the diurnal variability was found to be approximately 3 or 4 times greater than on non-pyrogenic aerosol days (Table 2.2).

With respect to the second research objective, cloudless sky measurements of global, direct and diffuse irradiance for 2003 were analyzed on a one-minute and daily basis in order to identify diurnal and season irradiance regimes. Graphical plots of daily global and direct irradiance identified distinct regimes in both datasets that clearly track extraterrestrial irradiance. Alternately, a graphical plot of daily diffuse irradiance values throughout 2003 identified a pattern in which absolute values showed less seasonal variation. While global, direct and diffuse irradiance follow seasonal patterns throughout most of 2003, significant variability in direct and diffuse irradiance occurred during the mid-summer pyrogenic aerosol period. However, variability in global irradiance was lower by comparison, as an increase in diffuse irradiance compensated for the depletion in direct irradiance.

Seasonal cloudless sky irradiance regimes were also studied using the clearness index, transmissivity and diffuse ratio. Using these ratios, optical air mass and pyrogenic aerosols were identified as the two major factors influencing cloudless sky global, direct and diffuse seasonal irradiance regimes in 2003. Both increased optical air mass and pyrogenic aerosols limit the irradiance reaching the surface by affecting attenuation levels within the atmosphere. The average daily clearness index and transmissivity for 2003 are 0.75 and 0.60 respectively. The average daily diffuse ratio for 2003 is 0.13. During winter periods, daily clearness index and transmissivity values drop to 0.70 and 0.52 respectively, while diffuse ratio values reach as high as 0.18. During summer days when pyrogenic aerosols were present, the daily clearness index and transmissivity drop as low as 0.69 and 0.47 respectively, while the diffuse ratio reaches 0.20. While wintertime deviations from the annual mean values are attributable to large optical air mass, the summertime deviations are not. Rather, the summertime deviations are attributable to the presence of pyrogenic aerosols.

Diurnal cloudless sky irradiance is principally symmetrical about solar noon. This diurnal symmetry in global, direct and diffuse irradiance is clearly dependant on solar zenith angle, with maximum irradiance values occurring at solar noon. This symmetry is also apparent in the diurnal plots of the clearness index, transmissivity and the diffuse ratio. While the clearness index and transmissivity show symmetry about a diurnal maximum value occurring at solar noon, the diffuse ratio shows symmetry about

a diurnal minimum value occurring at solar noon. However, changing atmospheric composition, between forenoon and afternoon periods, introduced small amounts of asymmetry to the cloudless sky diurnal irradiance trend. This asymmetry is attributable to increased irradiance attenuation, resulting from either increased surface convection (i.e. higher atmospheric concentrations of dust and water vapour) during afternoon periods or the movement of aerosol plumes (Figure 2.3). This diurnal asymmetry was most prevalent during the summer, when convective instability at the surface is most intense, and dust and water vapour are readily available for transport into the atmosphere.

The final research objective involved using the Houghton (1954) model to estimate one-minute values of global, direct and diffuse irradiance for 35 cloudless days with varying aerosol concentrations. The accuracy of one-minute irradiance estimates were assessed through use of the MBE, MAE, RMSE and d. During summer periods, model estimates of global, direct and diffuse irradiance are accurate. The RMSE for global irradiance on summertime non-pyrogenic aerosol days varies between 7.6 W m^{-2} and 11.9 W m^{-2}. During winter, RMSE values range between 17.1 W m^{-2} and 41.7 W m^{-2}. Finally, during the mid-summer pyrogenic aerosol event, RMSE values range between 12.0 W m^{-2} and 26.3 W m^{-2}. In the winter, model underestimation of global and direct irradiance is largely attributable to an inadequate aerosol parameterization. Specifically, Houghton's original k-value is too small, thus implying more attenuation. The limitations inherent to Houghton's aerosol parameterization necessitated the development of a revised parameterization. For this location, a wintertime k-value of 0.973 is more appropriate.

Model estimates during the mid-summer pyrogenic aerosol event poorly represented their observed counterparts. The deviation between predicted and observed irradiance values necessitated the development of a more adequate dust factor. This study found a k-value of 0.846 better approximates days with pyrogenic aerosols. Model overestimation of global and direct irradiance is attributable to increased absorption and scattering by pyrogenic aerosols. Maximum aerosol depletion of global and direct irradiance, above normal background levels, occurred on DOY 230 where irradiance deficits of 3.4% and 23.1% respectively occurred. Likewise, model underestimation of diffuse irradiance is attributable to increased scattering by the pyrogenic aerosols. The

maximum spike in diffuse irradiance from aerosols, above normal background levels, occurred on DOY 209 when the diffuse irradiance increased by 50.2%.

Future research may investigate the application of a variable dust factor in the hopes of improving flux estimates. For example, one possibility is to assume the average dust factor values derived in this study (Figure 2.18) in lieu of a constant k = 0.95. In a brief application of this approach, Houghton's model was re-run for DOY 42 (winter day, k = 0.973), 145 (spring day with no pyrogenic aerosols, k = 0.94) and 230 (summer day with pyrogenic aerosols, k = 0.846). The results of this approach are given in Table 2.5 for direct and diffuse irradiance. In this case, estimates for the direct beam were improved by approximately 50 percent for all three days while the diffuse irradiance was improved on two of the three days.

Table 2.5. Comparison of RMSE values (W m^{-2}) for direct and diffuse irradiances using variable k-values from this study and constant k-value from Houghton (1954).

DOY	RMSE Variable k values			RMSE Constant k values		
	k	Direct	Diffuse	k	Direct	Diffuse
42	0.973	13.02	12.35	0.950	31.04	9.90
145	0.940	7.77	6.67	0.950	14.68	7.79
230	0.846	32.16	58.27	0.950	106.38	69.42

In order to make further improvements in estimates of the diffuse irradiance, research is required to incorporate the effects of surface albedo and multiple reflections. Furthermore, the absorption and scattering extinction coefficients must be specified to correctly assess the absorption optical depth and scattering optical depth for aerosols.

Chapter 3.
Measurement of Spectral Global Irradiance on the Canadian Prairies: The Cloudless Sky Regime and the Influence of Pyrogenic Aerosols

3.1. Introduction

Spectral irradiance at the Earth's surface is most accurately determined through field measurement programs. However, measurement of spectral irradiance is not yet common within Canada. This deficiency is, in part, due to the high cost of spectral radiometers. Furthermore, depending on sensor type, operation of spectral radiometers can be labour intensive, often leading to increased costs. Unfortunately, this economic barrier has contributed to a lack of spectral databases (Betts *et al.*, 2001). The shortfall in spectral measurement programs has resulted in a lack of detailed knowledge of the spectral distribution of irradiance for many geographical locations (Betts *et al.*, 2001; Martínez-Lozano *et al.*, 1995). This situation is unfortunate, as the knowledge of spectral irradiance is important for the validation of transmission models, the development of solar energy devices (Adeyefa and Holmgren, 1996) and the estimation of their performance in a wide range of environments (Martínez-Lozano *et al.*, 1995). Given these needs, this research examines the spectral distribution of global irradiance under cloudless skies at Environment Canada's Baseline Surface Radiation Network (BSRN) Bratt's Lake Observatory in southern Saskatchewan. Data collection activities for this research took place from June 15 until August 22, 2003.

Irradiance attenuation from constituents within both solar and terrestrial atmospheres is a major factor shaping the spectral distribution of global irradiance at the Earth's surface. With respect to the Sun's atmosphere, absorption by several elements is responsible for much of the high amplitude global irradiance variability observed across the 0.28 – 0.80 μm spectral range. Within the Earth's atmosphere, global irradiance is subject to absorption and scattering from a variety of permanent (i.e. nitrogen and

oxygen) and variable (i.e. water vapour and ozone) gases, aerosols (i.e. dust, ash, smoke and salt), and cloud. The attenuation effects of these constituents cause more variability in an already high amplitude solar spectral distribution. In the absence of clouds, which have the greatest effect on the amplitude of irradiance at the surface (Bird *et al.*, 1982), spectral variability caused by individual atmospheric gases and aerosols can be studied.

Due to its mid-latitude continental location, the climate at the Bratt's Lake Observatory is characterized by cold winters and warm summers. Atmospheric concentrations of aerosol also vary by season, with lower concentrations generally occurring in winter and late autumn months and higher concentrations generally occurring in late spring and summer months (Smirnov *et al.*, 1996; Holben *et al.*, 2001). During the warmest periods of the year at the Observatory, large aerosol concentrations (i.e. higher aerosol optical depth) are often the result of increased surface convection and the intrusion of moist tropical air masses.

In late July and August of 2003, aerosol optical depths at the Observatory increased in response to the arrival of pyrogenic (i.e. smoke) aerosol plumes. As such, a large range in aerosol optical depth values were recorded during the spectral measurement period; from characteristically low background values when the pyrogenic aerosols were absent (Smirnov *et al.*, 1996) to high values when the pyrogenic aerosols were present. Research has also linked similar behaviour in summertime aerosol optical depths measured at 0.5 μm for locations in central Saskatchewan and Manitoba to forest fire activity (Markham *et al.*, 1997; Holben *et al.*, 2001). On average, optical depth variability in western Canada during the summer is attributable to smoke from forest fires 80% of the time (O'Neill *et al.*, 2002). In the present study, aerosol plumes mainly followed eastward trajectories into southern Alberta and Saskatchewan from fire source regions located in British Columbia and several northwestern states (Appendix 2). Besides an increase in aerosol optical depth, the arrival of pyrogenic aerosol plumes is denoted by the presence of haze and reduced clearness index values from 0.28 to 0.80 μm. While pyrogenic aerosols reduce global irradiance over all wavelengths between 0.28 – 0.80 μm, analysis indicates that attenuation is greatest at shorter wavelengths.

3.2. Extraterrestrial Spectral Irradiance

Essentially the only major source of irradiance that influences the Earth's climate is the Sun (Iqbal, 1983). While the Sun emits irradiance over all wavelengths, 99% of that energy falls between 0.25 – 4.0 μm (Iqbal, 1983). At the top of Earth's atmosphere, the spectral distribution of solar energy is termed the extraterrestrial spectral distribution. Determination of the extraterrestrial spectral distribution has been undertaken by a number of researchers (e.g. Arvensen *et al.*, 1969; Thekaekara *et al.*, 1971; Smith and Gottlieb, 1974, Neckel and Labs, 1984; Wehrli, 1985; Nicolet, 1989; VanHoosier, 1996; American Society for Testing and Materials, 2000; Thullier *et al.*, 2003), using both satellite and non-satellite data. Satellite data has come from a variety of spectroradiometers situated on space borne platforms (i.e. Orbiting Solar Observatory, 1962; Solar and Heliospheric Observatory, 1985; Upper Atmosphere Research Satellite, 1991; Solar Ultraviolet Spectral Irradiance Monitor, 1994) (VanHoosier, 1996; Myers, 2004) or spacecraft (Atmospheric Laboratory for Applications and Science-1, 2 and 3: 1992-1994) (VanHoosier, 1996). Non-satellite data has been obtained from ground observatory telescopes, high altitude observatories, stratospheric balloons, rockets and research aircraft.

Recently, Gueymard (2004) has assembled a new composite and synthetic extraterrestrial spectrum. This spectrum, referred to as the 2003 synthetic Gueymard spectrum (Renewable Resource Data Center, 2005), was proposed because of several problems discovered in both the Wehrli (1985) and American Society for Testing and Materials (2000) spectrums and due to publication of new irradiance datasets based on modern frequently calibrated instruments (Gueymard, 2004). The spectral resolution is approximately equal to the wavelength step size (i.e. 0.001 μm from 0.5 – 0.28 μm, 0.0005 μm from 0.280 – 0.4 μm, 0.001 μm from 0.4 – 1.705 μm, 0.005 μm from 1.705 - 4.0 μm and increasing intervals after 4.0 μm) (Gueymard, 2004). Furthermore, the total irradiance for Gueymard's spectrum is 1366.1 W m^{-2}, the value of the solar constant currently accepted by the space community (American Society for Testing and Materials, 2000; Renewable Resource Data Center, 2005; Johnson, 2005). Due in part to the above advantages, this research adopts the 2003 synthetic Gueymard extraterrestrial spectrum.

The resolution and interval of Gueymard's spectrum enables the computation of ratios versus surface global irradiance measurements collected at an interval of 0.001 μm from 0.28 to 0.80 μm. The ratio of global horizontal irradiance at the surface to extraterrestrial horizontal irradiance is termed the clearness index (Adeyefa and Holmgren, 1996). Calculation of the clearness index has been undertaken using both individual spectra and integrated spectral bands. These bands are listed in Table 3.1. The spectral range for ultraviolet B (UVB) and ultraviolet A (UVA) bands were adopted from several publications of the World Meteorological (WMO) (2003) and World Health (WHO) (2002) Organizations. Spectral ranges for visible and NIR bands were adopted after slight modification from Iqbal (1983). Integration of irradiance across these bands was undertaken using the trapezoidal rule.

Table 3.1. Name and spectral range of the integrated bands used to develop a clearness index.

Band Name	Spectral Range (μm)
UVB	0.280 – <0.315
UVA	0.315 – <0.400
Violet	0.400 – <0.455
Blue	0.455 – <0.492
Green	0.492 – <0.577
Yellow	0.577 – <0.597
Orange	0.597 – <0.622
Red	0.622 – <0.770
NIR	0.770 – <0.800
Full Band	0.280 – <0.800

3.3. Experimental Procedure

Spectral global irradiance measurements were collected from June 15 to August 22, 2003. Global irradiance was measured across the 0.28 – 0.80 μm spectral range, at 0.001 μm intervals, with an OL 754 Portable High Accuracy UV-Visible

Spectroradiometer (Optronic Laboratories Inc., Orlando Florida). The OL 754 Spectroradiometer system consists of an OL 754-O-PMT or OL 754-O-Si or OL 754-O-NIR Optics Head, OL 754-C Controller and optOLab^{TM} General Operating Software (Optronic Laboratories Inc., 1996). A portable computer is also incorporated into the system. The OL 754-O-PMT was the sole Optics Head used throughout this research. The OL 754 Optics Head consists of a high efficiency double monochromator with dual holographic gratings, an S-20 response thermoelectrically cooled photomultiplier (PMT) detector, and a PTFE coated integrating sphere with fused silica dome (Optronic Laboratories Inc., 1996). Several characteristics of this Optics Head are a large user adjustable wavelength range, narrow bandwidth, low stray light level and high wavelength precision and accuracy (Table 3.2). While the OL 754-O-PMT Optics Head is sensitive to irradiance from 0.20 to 0.80 μm, for practical purposes (i.e. strong O, O_2, O_3, N and N_2 attenuation at wavelengths less than 0.28 μm) only global irradiance from 0.28 to 0.80 μm was measured. The spectroradiometer was positioned to measure spectral global irradiance on a horizontal surface. The OL 754-C Controller houses the electronic controls and is responsible for all signal processing (Optronic Laboratories Inc., 1996).

At the Observatory, part of the Optics Head of the OL 754, the integrating sphere and fused silica dome, was located on the main instrumentation platform directly above the instrumentation trailer at a height of 6.1 meters above the ground. However, because this optical head is not waterproof it was protected by a waterproof tarp when not in use. A fiber optic cable was run from the integrating sphere (located on a tri-pod stand on the main platform) (Figure 3.1) down into an office where the remaining OL 754 components (i.e. the monochromator, controller and laptop computer) were located. In terms of protecting the measurement program from random power fluctuations and outages, an uninterruptible power supply was incorporated into the system.

The OL 754 requires approximately 23 minutes to measure spectral global irradiance, at 0.001 μm intervals, from 0.280 to 0.800 μm. However, scanning speed across this wavelength range is not uniform (Table 3.3). Depending on instrument settings and raw signal strength (Amps), spectral global irradiance measurements are

Table 3.2. Specifications for the PMT Optics Head (OL 754-O-PMT). Data Source: Optronic Laboratories Inc., 1996.

Wavelength Range		200 – 800 nm
Wavelength Accuracy	Full Range 200 – 800 nm UVB range 280 – 320 nm	± 0.2 nm ± 0.1 nm
Wavelength Precision		0.05 nm
Scan Resolution		0.05 nm
Spectroradiometric Accuracy (Relative to NIST at NIST standard irradiance levels)		± 1-3 %
Bandpass		1 to 10 nm
Noise Equivalent Irradiance (NEI) at 280 nm (2 nm HBW)		10^{-11} W / cm^2 nm
Stray Light		10^{-8} at 285 nm (typ)
Scan Speed (normal scanning)	Full Range 200 – 800 nm at 10 nm UVB Range 280 – 320 nm at 1 nm	≈ 1 min (typ) < 1 min (typ)
Detector		S-20 response PMT
Input Optics		0.1524 metre diameter integrating sphere
Filter wheel	3 blocking filters: 289 nm, 344 nm, 601 nm (nominal)	Open, shutter

Table 3.3. Time required to measure irradiance at a particular signal level (combined integration and settling time). Data Source: Optronic Laboratories Inc., 1996.

Signal Level (Amps)	Acquisition Time	Measurement Time (seconds)
1.000 E-05	Fast	2.4
1.000 E-06	Fast	2.4
1.000 E-07	Fast	2.4
1.000 E-08	Medium	3.5
1.000 E-09	Medium	3.5
1.000 E-10	Slow	6.0
1.000 E-11	Slow	6.0
1.000 E-12	Slow	6.0

Figure 3.1. The OL 754 Spectroradiometer. Silica dome (1), integrating sphere (2), fiber optic cable (3), dual wavelength and gain lamp (4) and tripod base (5).

collected at three speeds: fast, medium and slow. Typically, slow and medium measurement times occur across ultraviolet and near infrared portions of the spectrum (i.e. a relatively weaker signal) while fast measurement times occur across visible parts of the spectrum (i.e. a relatively stronger signal). The measurement times provided in Table 3.3 consist of both settling and integration times. The settling time refers to the time the controller will settle after each wavelength change prior to acquiring a new signal; the integration time is the time allotted for the controller to average the irradiance signal at each wavelength (Optronic Laboratories Inc., 1996). Table 3.3 provides the measurement times required for the OL 754 to obtain the global irradiance at every 0.001 μm interval from 0.28 to 0.80 μm.

The OL 754 Spectroradiometer was calibrated on a regular basis during the measurement program. Specifically, the OL 754 was calibrated with an OL 752-150 dual wavelength calibration and gain check source module (now referred to as a dual wavelength and gain lamp), a 200-Watt lamp and two 1000-Watt lamps (Appendix 6). The dual wavelength and gain lamp was used to calibrate the OL 754 on a daily basis

(Figure 3.1). The 200-Watt lamp is an OL 752-10E tungsten halogen lamp, an irradiance standard traceable to NIST (National Institute of Standards and Technology) (Wu, 2002). An OL 56A Programmable Current Source powers the lamp. The 200-Watt lamp was used for weekly calibrations of the OL 754. The 1000-Watt S-919 and S-701 lamps are also tungsten halogen lamps, and are irradiance standards traceable to NIST (Wu, 2002). Both 1000-Watt lamps were powered by an XHR 150-7DC Power Supply equipped with a computerized feedback loop, and calibrations involving these lamps were undertaken once every three weeks. Following an assessment of lamp stability over the measurement period, calibration factors obtained from the 1000-Watt S-701 lamp were applied to the spectral global irradiance dataset.

Due to the strong radiative absorption and scattering characteristics of cloud, irradiance measurements were undertaken during cloudless atmospheric conditions. Under these conditions, scans were run continuously, unless malfunctions occurred or calibration and maintenance was required. However, due to the relatively long time required for each scan, approximately 23 minutes, the presence of cloud was by far the most common factor necessitating the end of observations. Sky conditions were checked throughout the day and if clouds were present, scanning was halted. Often by the early afternoon, local cumulus development via surface convection was enough to warrant the termination of the irradiance scans. During late July and August, pyrogenic aerosols arising from upwind wildland fires (Appendix 2) were also present within the atmosphere. However, scanning continued when pyrogenic aerosols were present.

From June 15 to August 22, 366 irradiance scans were collected. Specifically, 61 scans were taken in June, 142 scans were taken in July, and 163 scans were taken in August. Besides visual observations, a MFRSR (Multi Filter Rotating Shadow Band Radiometer), CM21 Pyranometer and CH1 Pyrheliometer were used to identify the presence of cloud within the atmosphere. Using these instruments, the cloudless sky global irradiance dataset was refined to include 172 scans, 67 of which were collected in July, and 105 were collected in August. Table 3.4 provides a summary of all cloudless sky irradiance scans collected throughout the measurement program.

Table 3.4. Numerical summary of cloudless sky spectral global irradiance scans for 2003 at the Bratt's Lake Observatory.

Calendar Date	Day of Year	Number of Scans
July 15	196	14
July 22	203	13
July 24*	205	7
July 28*	209	15
July 30*	211	7
July 31*	212	11
August 10*	222	19
August 13	225	12
August 14*	226	17
August 15*	227	20
August 18*	230	19
August 19*	231	18

* denotes visible haze present within the atmosphere.

Located on an operational farm, surface cover at the Bratt's Lake Observatory included agricultural crops. Consideration of surface type is important when examining the spectral distribution of global irradiance at Earth's surface. This is because the diffuse component of global irradiance is affected by surface reflectivity (i.e. albedo) through multiple reflections between the ground and the sky. However, the impact of albedo is largely confined to shorter wavelengths, as the direct beam comprises the majority of incoming global irradiance above 0.4 μm (Gueymard, 1995). During the summer of 2003, surface vegetation to the east and north of the Observatory's main instrumentation platform were wheat and flax respectively. The 32.4-hectare wheat field planted to the east of the measurement platform was seeded on May 21, swathed on August 14 and combined on August 19. The flax field, which covered 47.4 hectares to the north of the measurement platform, was seeded on May 28 and combined on August 26.

As several agricultural crops were planted around the measurement site, the amount of multiple scattering between the ground and sky is dependant on the reflectivity of each crop type. Furthermore, the albedo of wheat is not constant over a growing season (i.e. from bare soil through to a ripe wheat crop) (Dexter, 2004). However, as the spectral irradiance data of interest to this research was collected towards the end of the

growing season, the change in surface reflectivity during this period is negligible. Unfortunately, the wheat crop was swathed and then combined on August 14 and 19 respectively (i.e. during the last few days of the spectral measurement period), actions that would ultimately lower the albedo. While the change in surface cover is significant, its overall affect on the spectral global irradiance dataset is reduced because the wheat was not combined until the last day of the measurement period and because the flax surface was not combined until measurements were over. The effect of surface reflectivity on spectral global irradiance is examined briefly in section 3.4.2 using the cloudless sky spectral irradiance model SMARTS2 (Simple Model for the Atmospheric Radiative Transfer of Sunshine) (Gueymard, 1995).

3.4. Results

3.4.1. Cloudless Sky Spectral Global Irradiance From 0.28 – 0.80 μm

Across the 0.25 – 4.0 μm wavelength range, solar spectral irradiance at the top of the Earth's atmosphere displays significant and irregular fluctuations. Fraunhofer lines (i.e. troughs in the solar spectrum caused by absorption of irradiance within the Sun's atmosphere) are responsible for the irregular fluctuations observed within the extraterrestrial spectrum (Figures 3.2 and 3.3) (Bird *et al.*, 1982). In Figure 3.3, matching high amplitude troughs on extraterrestrial and surface spectra denote the presence of Fraunhofer lines for Fe, Ca, H, Mg and Na. At the surface, the spectral distribution of global irradiance is lower in magnitude than that of the extraterrestrial distribution, the difference being the result of attenuation from the Earth's atmosphere (Figure 3.2). This attenuation, which introduces more variability into the global spectral distribution in several spectral regions, also reduces variability in several regions of the extraterrestrial spectrum (Figures 3.2 and 3.3).

Solar position exerts considerable influence on the magnitude of spectral irradiance reaching the Earth's terrestrial environment. Depending on the day of year, the position of Earth along its elliptical orbit (i.e. the Sun-Earth distance changes continuously) will affect the magnitude of extraterrestrial irradiance. Following the

inverse square law, the Earth will receive less irradiance at aphelion (i.e. Earth is furthest from the Sun) and more irradiance at perihelion (i.e. Earth is closest to the Sun).

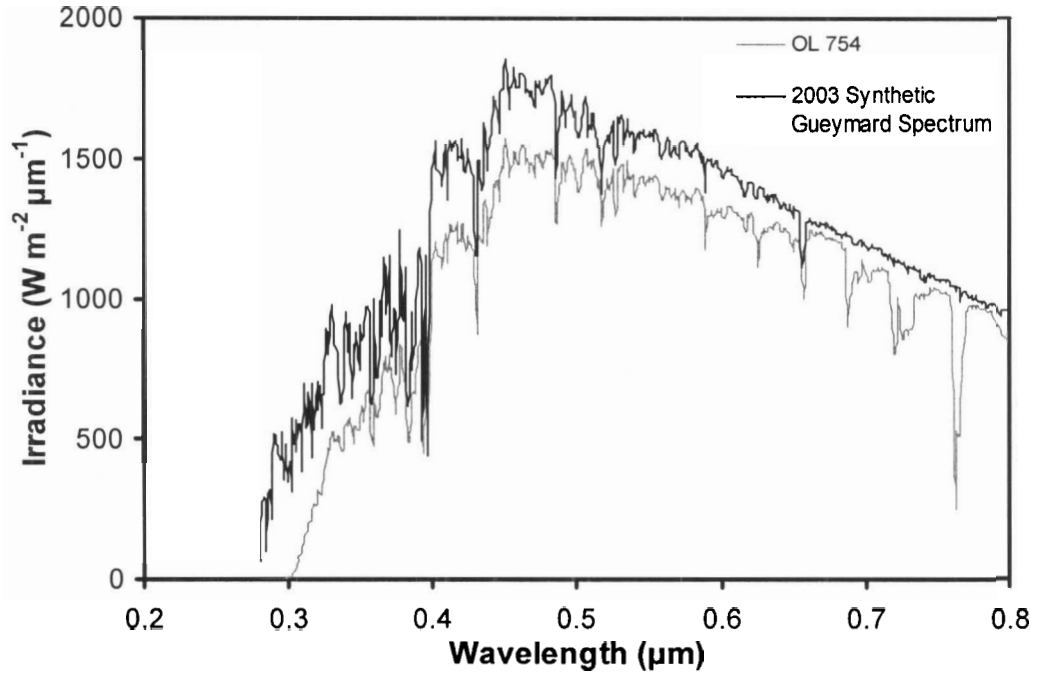

Figure 3.2. Comparison of surface (OL 754) and extraterrestrial (2003 Synthetic Gueymard) spectra between 0.28 and 0.80 µm on July 22 (DOY 203) at approximately solar noon.

Besides absorption within the solar atmosphere and Sun-Earth distance, the variability and magnitude of spectral irradiance at the Earth's surface is controlled by atmospheric composition, latitude and time of day. With respect to atmospheric composition, the distribution of spectral global irradiance at the surface depends on gas, cloud and aerosol concentrations. Neglecting cloud, strong radiative absorption and scattering characteristics of several gases and aerosols, contribute to form a surface spectrum that exhibits both lower magnitude and different structure than the extraterrestrial spectrum (Figure 3.3). Atmospheric gases and aerosols scatter and absorb irradiance across ultraviolet, visible and infrared parts of the spectrum. Atmospheric scattering from gases, Rayleigh scattering, increases with decreasing wavelength (λ) (i.e. atmospheric scattering is a continuous function of wavelength) (Iqbal, 1983). In Rayleigh

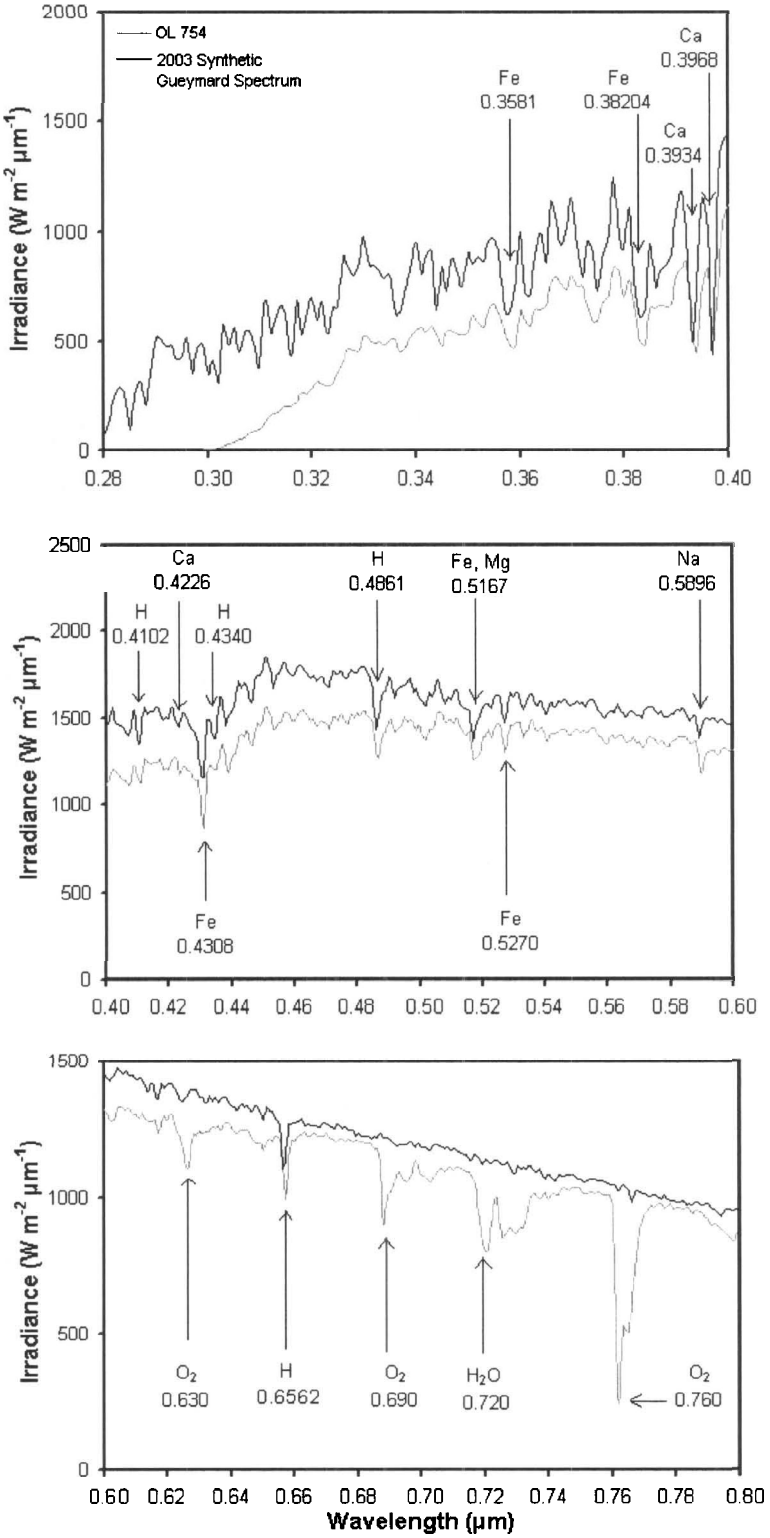

Figure 3.3. Comparison of surface (OL 754) and extraterrestrial (2003 Synthetic Gueymard) spectra between 0.28 and 0.80 µm on DOY 203 at approximately solar noon. Several Fraunhofer lines (Bird *et al.*, 1982) and absorption bands are identified.

scattering, the scattering particles are assumed spherical and less than 0.2 λ in diameter (Iqbal, 1983). Furthermore, scattering is equal in forward and backward directions but minimal at 90° to the direction of the incident photon (Iqbal, 1983).

Unlike atmospheric scattering, absorption by gases (i.e. O, O_2, O_3, H_2O, N, N_2, N_2O, NO_2, CO, CO_2 and CH_4) is wavelength selective (Iqbal, 1983). Of these gases, atomic and diatomic oxygen and nitrogen, and ozone are the five principal absorbers in the ultraviolet and visible portions of the electromagnetic spectrum (Iqbal, 1983). Along with several Fraunhofer lines, the major troughs caused by gaseous absorption are presented in the spectral distribution plots in Figure 3.3. Specifically, the distinct irradiance trough at 0.72 μm is attributable to water vapour absorption and the troughs at 0.63, 0.69 and 0.76 μm are attributable to diatomic oxygen absorption. Also on Figure 3.3, note that only extremely small amounts of extraterrestrial irradiance reach the surface below 0.30 μm. Here, strong absorption is attributable to atomic and diatomic oxygen and nitrogen, and ozone (Iqbal, 1983). Ozone also has a strong absorption band (Hartley band) between 0.22 – 0.32 μm (Jacovides *et al.*, 2000). The separation between surface and extraterrestrial spectral distributions from 0.300 – 0.345 μm (Huggins band) and 0.44 – 0.70 μm (Chappuis band) (Jacovides, *et al.*, 2000) is also partly attributable to ozone absorption. Water vapour absorption ranges from strong to weak across the 0.57 – 0.77 μm spectral range (Bird *et al.*, 1982). Finally, nitrogen dioxide is also an important absorber of irradiance across the 0.25 – 0.70 μm spectral range (Jacovides *et al.*, 2000).

Besides attenuation from gases, aerosols also influence the terrestrial spectral distribution. Aerosols are defined as small solid or liquid particles that remain suspended in the air and follow the motion of the air within certain broad limits (Iqbal, 1983). Aerosols originate from both terrestrial (i.e. volcanic eruptions, sandstorms, industrial smoke, pollen and forest fires) and marine (i.e. ocean spray and salt crystals) environments (Iqbal, 1983; Power 2003). While irradiance attenuation by aerosols generally involves scattering, absorption also occurs (Iqbal, 1983). Atmospheric scattering by aerosols is termed Mie scattering. Mie scattering is the process whereby aerosol particles of relatively large size (i.e. 10^{-3} to 10^{2} μm for natural aerosol particles) (Iqbal, 1983) (i.e. the particle size is approximately equal to the wavelength of irradiance), scatter more irradiance in a forward direction. While aerosol absorption may

show some spectral selectivity, both scattering and absorption processes are generally a continuous function of wavelength (Iqbal, 1983).

With respect to the time of day, diurnal changes in optical air mass (m) coincide with significant changes in spectral global irradiance at the surface. During periods when solar elevation is low and optical air mass values are high (i.e. early forenoon and late afternoon periods), atmospheric attenuation is relatively high and the magnitude of the terrestrial spectra is reduced. Also, and because Rayleigh scattering increases with decreasing wavelength and increasing optical air mass, this reduction is not uniform across the terrestrial spectrum, with more attenuation occurring in the ultraviolet and visible parts of the spectrum than at longer wavelengths (i.e. the Sun appears redder during forenoon and afternoon periods) (Bird *et al.*, 1982; Martinez-Lozano *et al.*, 1995). Alternately, the surface spectral distribution is least influenced by optical air mass during midday periods. During midday periods, when solar elevation is high and optical air mass values are low, atmospheric attenuation is relatively low and the magnitude of the terrestrial spectrum is relatively large. Figure 3.4 shows the variation in the surface distribution of spectral global irradiance from 0.28 to 0.80 μm for five forenoon scans (each scan is approximately one hour apart) on July 22 (DOY 203) at the Bratt's Lake Observatory in southern Saskatchewan. Here, note the influence of optical air mass on the distribution of spectral global irradiance. The spectral distributions with low energy amplitudes occur during early forenoon periods and correspond to low solar elevations (i.e. large optical air mass), while distributions with high energy amplitudes occur during midday periods that correspond to high solar elevations (i.e. small optical air mass). Furthermore, note that optical air mass is changing at a high rate during early forenoon periods (i.e. denoted by the large separation between consecutive scans) and at a lower rate during midday periods (i.e. denoted by the small separation between consecutive scans).

By integrating spectral global irradiance from 0.28 to 0.80 μm, as well as at several specified bands, the more familiar broadband diurnal global irradiance regime is observed. Figure 3.5 is a diurnal irradiance trend constructed by integrating spectral global irradiance across UVA, violet, blue, green, yellow and red bands (spectral ranges provided in Table 3.1) from 20 individual scans collected on August 10, 2003 (DOY

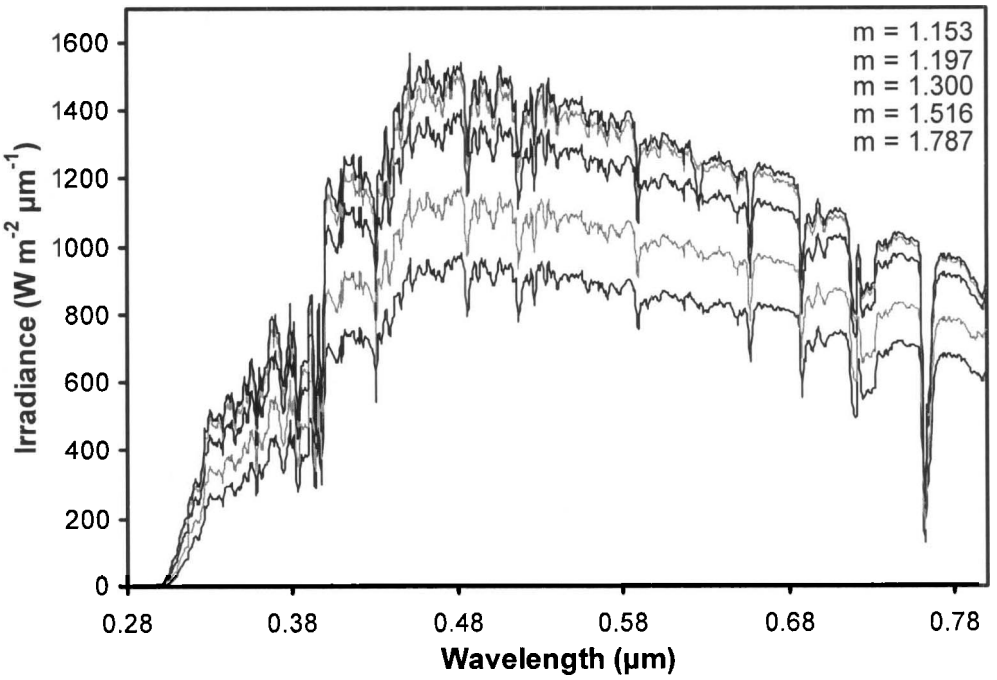

Figure 3.4. Five measured spectral distributions of global irradiance from 0.28 to 0.80 µm. Measurements (from bottom to top) were collected on DOY 203 at 7.94, 8.72, 9.78, 10.75 and 11.97 hours (LAT) at the Bratt's Lake Observatory.

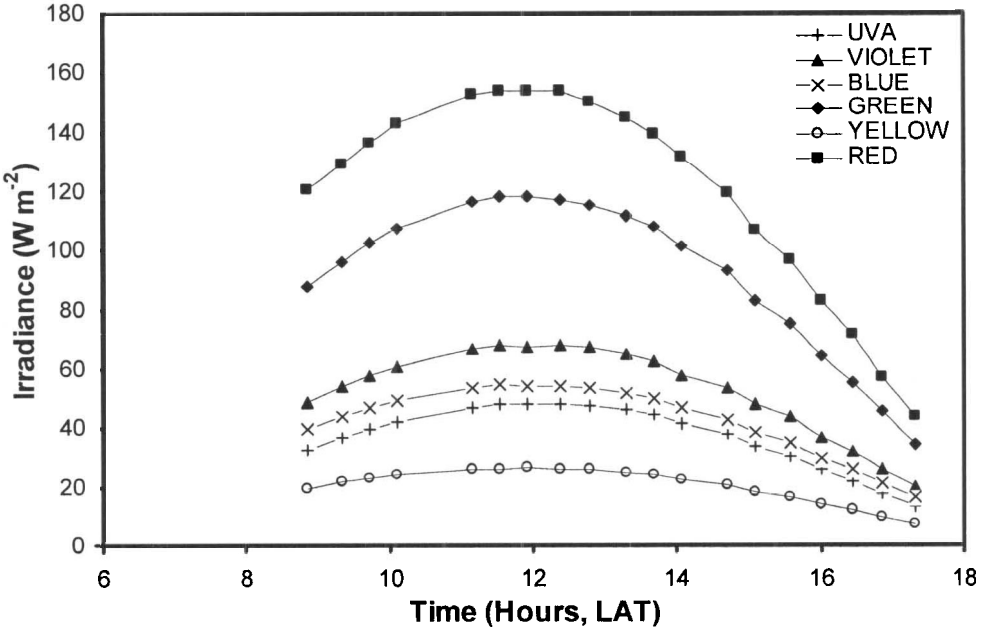

Figure 3.5. Diurnal global irradiance regime on one cloudless day (DOY 222). Individual trends represent the integrated global irradiance (W m^{-2}) across UVA, violet, blue, green, yellow and red spectral bands.

222). The smooth diurnal regime apparent for each spectral band on Figure 3.5 (with symmetry about 12 LAT) is characteristic of global irradiance plots for cloudless atmospheric conditions. Furthermore, Figure 3.5 shows that the relative amount of global irradiance distributed to each spectral band is not equal, with the majority of energy falling into red and green spectral bands.

3.4.2. Cloudless Sky Spectral Clearness Index From 0.28 – 0.80 μm

While graphical plots of irradiance provide insight into the effects of atmospheric attenuation on the distribution of spectral global irradiance, the clearness index is much more effective. By definition, the clearness index is the ratio of global irradiance at the surface to extraterrestrial irradiance (Adeyefa and Holmgren, 1996). As such, this ratio indicates the amount of attenuation within the atmosphere. However, unlike transmissivity, the clearness index is not a pure measure of atmospheric attenuation as the diffuse component of global irradiance partly depends on surface reflectivity (i.e. multiple reflections between the surface and the atmosphere). Therefore, while direct beam irradiance makes up the majority of incoming global solar irradiance above 0.4 μm (Gueymard, 1995), changes in surface reflectivity may mask subtle changes in atmospheric attenuation, especially at shorter wavelengths.

In the area surrounding the main measurement platform at the Observatory, several different agricultural crops were planted. During the 2003 growing season, these crops were wheat and flax. With respect to wheat, which was planted to the east of the platform, a previous study at the Observatory showed that broadband daily albedo values increased from 0.10 to 0.22 from seeding to harvest (Dexter, 2004). While this change is large, during later stages in the growing season (i.e. during the period most relevant to this study (i.e. July 15 – August 19)), the broadband daily albedo of wheat showed much less change, from approximately 0.18 on July 15 to 0.21 on August 19 (Dexter, 2004). However, during the summer of 2003, the wheat field was swathed and combined before the termination of the spectral measurement program (i.e. on August 14 and 19 respectively). From Dexter (2004), a reasonable approximation for the decrease in surface albedo after the wheat was combined is approximately 0.04.

Using the cloudless sky spectral irradiance model SMARTS2, an experiment was conducted to examine the influence of albedo on the surface distribution of spectral global irradiance from 0.28 to 0.80 μm. The SMARTS2 model was operationalized for August 19 (DOY 231; LAT = 11.73) and spectral global irradiance was calculated three times using broadband albedo values equal to 0.21 (i.e. for a ripe wheat crop), 0.17 (i.e. for a stubble surface) and 0.10 (i.e. for bare soil) (Dexter, 2004). Model estimates of spectral global irradiance using an albedo of 0.21 were only slightly larger than global irradiance calculated using an albedo of 0.17 and 0.10. Specifically, and relative to calculations made with an albedo equal to 0.21, global irradiance at all wavelengths from 0.28 to 0.80 μm decreased by less than 2 % and 5 % when using an albedo of 0.17 and 0.10 respectively. The percentage change was however not constant with wavelength; instead, it was greatest at shorter wavelengths.

In summary, surface albedo during the spectral measurement program is assumed constant for three reasons: 1) because even relatively large decreases in the broadband albedo did not cause large decreases in global irradiance between 0.28 and 0.80 μm, 2) because flax was also grown in the fields to the north and was not combined until after the measurement program concluded (i.e. a more constant albedo is expected) and 3) because the wheat field was not combined until the last day of the measurement period.

As previously mentioned, the extraterrestrial spectral distribution employed in this research is the 2003 synthetic Gueymard spectrum (Gueymard, 2004). One advantage in using Gueymard's spectrum is the constant wavelength step, which enabled direct ratioing with surface irradiance from the OL 754 (i.e. interpolation to match extraterrestrial spectral resolution was not necessary). The clearness index at each wavelength ($c_{i\lambda}$) between 0.28 and 0.80 μm was calculated using the following formula

$$c_{i\lambda} = G_{\lambda} / [I_{On\lambda} (\cos z) (TSI / I_o) (E_o)] \qquad (3.1)$$

where G_{λ} is the spectral global irradiance at the surface measured with the OL 754 spectroradiometer, $I_{On\lambda}$ is the 2003 Gueymard extraterrestrial spectral irradiance for average solar activity conditions at mean Sun – Earth distance on a surface perpendicular to the Sun's rays, E_o is the eccentricity correction factor, TSI is the total solar irradiance and I_o is the solar constant (Gueymard, 2004). Because the OL 754 requires

approximately 23 minutes to measure spectral global irradiance at 0.001 μm intervals between 0.28 – 0.80 μm, $I_{On\lambda}$ was cosine corrected using the measurement time of the OL 754 at each wavelength (i.e. Table 3.3). From Gueymard (2004), the ratio of TSI to I_o was determined as

$$TSI / I_o = 0.99956 + 9.1216 \times 10^{-6} R_z - 3.37296 \times 10^{-8} R_z^2 \qquad (3.2)$$

where R_z is the daily Zurich sunspot number (Van der Linden, 2005). While this latter correction only has an extremely small effect on the extraterrestrial spectrum, it is included for completeness purposes.

The spectral clearness index from 0.28 to 0.80 μm was calculated for every cloudless sky irradiance scan taken during the summer measurement period. Figure 3.6 is a spectral clearness index plot for two scans collected at approximately 12:30 local apparent time (LAT) on DOY 203 and DOY 230. The data shown in Figure 3.6 supports the above discussion of atmospheric attenuation with respect to wavelength. Here, the clearness index decreases with decreasing wavelength across the 0.28 – 0.80 μm range. This decreasing trend is generally attributable to the attenuation effects (i.e. decreasing spectral transmittance towards shorter wavelengths) of ozone, dry air molecules (i.e. Rayleigh scattering) and aerosols (i.e. Mie scattering). Alternately and as previously mentioned, the distinct troughs in the clearness index at 0.63, 0.69 and 0.76 μm are attributable to diatomic oxygen absorption while the trough at 0.72 μm is attributable to water vapour absorption. Furthermore, the high clearness index values at longer wavelengths on DOY 203 (i.e. small separation between terrestrial and extraterrestrial spectra) suggests that atmospheric scattering at the Observatory is low towards the end of the visible and beginning of the NIR.

Similar atmospheric conditions (i.e. low attenuation) also occurred for cloudless scans on DOY 196, DOY 212 and DOY 222. It should be noted that spectral clearness index values greater than one were obtained for several scans during these days, predominantly at Fraunhofer lines and at several longer wavelengths (i.e. closer to 0.8 μm). Spectral clearness index values in excess of unity across the 0.28 – 0.80 μm range are attributable to a combination of factors, including atmospheric attenuation, sensor capabilities and solar variability. The amplitude (i.e. $c_{i\lambda} > 1$) and variability in $c_{i\lambda}$ is

particularly intense across the 0.335 – 0.410 μm spectral range. While Rayleigh scattering is prominent from 0.335 – 0.410 μm, ozone absorption is weak (0.33 – 0.35 μm) to non -

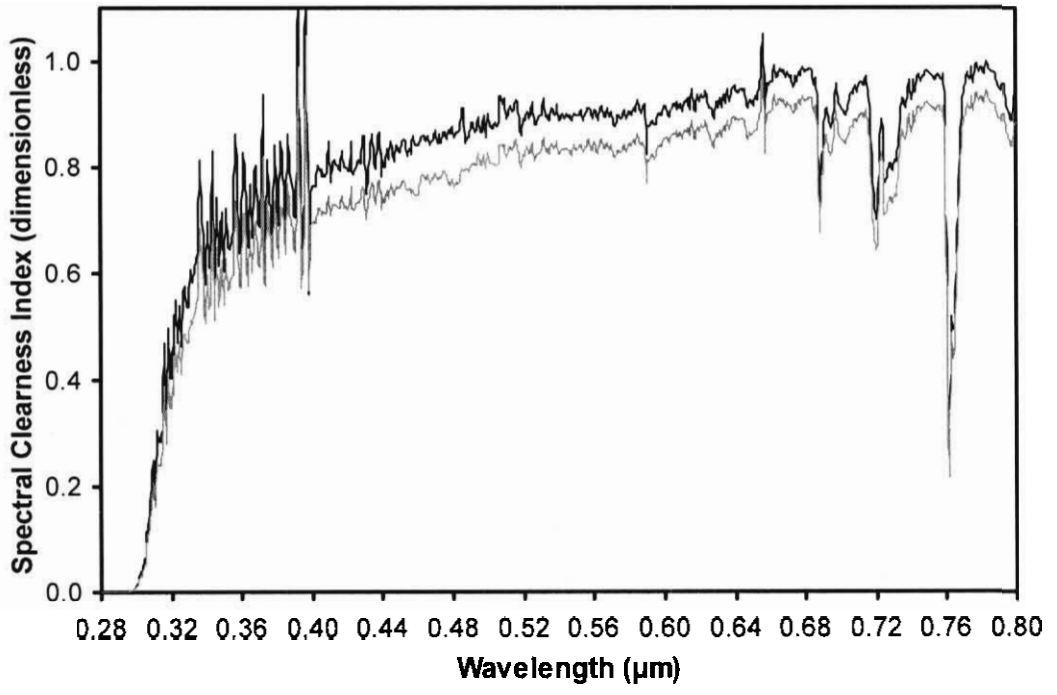

Figure 3.6. Spectral clearness index on DOY 203 (black) and DOY 230 (grey), at 12.48 and 12.53 hours (LAT) respectively. Pyrogenic aerosols are present on DOY 230.

existent (0.35 – 0.41 μm) (Iqbal, 1983). As such, surface and extraterrestrial irradiance will converge across this spectral range and clearness index values will naturally be closer to unity.

The observed variability from 0.335 – 0.410 μm is also likely attributable to measurement and source dependant parameters. With respect to measurement parameters, differences in calibration and wavelength precision and accuracy of spectroradiometers may contribute to this variability. At the top of the atmosphere, Gueymard's spectra from 0.335 – 0.410 μm is largely derived from space borne sensors. Finally, variability in $c_{i\lambda}$ may also be attributable to changes in solar output. Changes in solar output are influenced by both short (27-day rotational cycle) and long (11-year cycle) term solar cycles, resulting in increased or decreased irradiance levels at the top of the atmosphere

and surface. In fact, not all wavelengths are affected equally by solar variability, with much of the variation occurring in the far and extreme ultraviolet (i.e. < 0.2 μm) (Gueymard, 2004; Rottman, 1999). As such, solar variability is generally considered to have a very small amplitude (≈ 0.1 %) for the wavelengths of interest here (i.e. 0.335 – 0.41 μm) (Gueymard, 2004). Nevertheless, researchers have shown that variability in the extraterrestrial spectrum can be important at several Fraunhofer lines in the visible (Gueymard, 2004). Given this, it is interesting to note that the three $c_{i\lambda}$ values in excess of unity on Figure 3.6 occur at Fraunhofer lines (0.3934, 0.3968 and 0.6562 μm).

During summer, northwestern regions of North America often experience large and intense wildland fire activity. The summer of 2003 was no exception, with extensive wildland fires occurring throughout regions of British Columbia, Washington, Oregon, Idaho and Montana (Appendix 2). These fires generated large quantities of smoke and prevailing westerly winds carried these aerosols eastward into southern Saskatchewan. The smoke aerosols generated from wildfires have a wide range of effects; which include changes in visibility, air pollution, air chemistry and direct and indirect radiative forcing (O'Neill *et al.*, 2001). With respect to visibility, of the twelve observational days when spectral measurements were collected at the Observatory (Table 3.4), a distinct white haze was present within the atmosphere on nine. Using back trajectory analysis, the haze was linked to pyrogenic aerosols from fires burning hundreds of kilometres away in both western Canada and the northwestern United States. However, back trajectory analysis does not correlate with visual observations of white haze made on DOY 211 and 212 at the Observatory (Appendix 2). Specifically, back trajectory analysis shows strong northwesterly (Figure A2.5) and easterly (Figure A2.6) airflow at all pressure surfaces on DOY 211 and DOY 212 respectively.

In August, pyrogenic aerosol concentrations were particularly high. This statement is quantified by three observations during this period (i.e. DOY 226, 227, 230 and 231): 1) the density of atmospheric haze appeared to increase, 2) larger aerosol optical depth values were measured and 3) spectral global irradiance data showed enhanced atmospheric attenuation. Unfortunately, it was not possible to link the enhanced attenuation observed on DOY 225 to visual observations of pyrogenic aerosols (i.e. haze). However, the lack of haze on DOY 225 does not negate the presence of

pyrogenic aerosols, as the aerosols may have been located higher in the atmosphere than on other days. While back trajectory analysis on DOY 225 identifies that airflow was not of a westerly origin, airflow at the 700 hPa and 850 hPa pressure surfaces (Figure A2.8) does pass over a region of wildfire activity in southeastern Montana.

As mentioned above, the Mie scattering process defines irradiance scattering by aerosols. Figure 3.6 shows the spectral clearness index (i.e. from 0.28 to 0.80 μm) on a mid-summer day in which pyrogenic aerosols were visibly present within the atmosphere (i.e. DOY 230). Here, the attenuation effects from pyrogenic aerosols are distinct, with reduced clearness index values across the entire spectral range. From Iqbal (1983), it is apparent that aerosol attenuation generally increases in a non-linear fashion with decreasing wavelength across the 0.28 – 0.80 μm spectral range. This not only suggests that attenuation over all wavelengths (i.e. from 0.28 to 0.80 μm) will be greater when pyrogenic aerosols are present (i.e. Figure 3.6), but that attenuation likely increases with decreasing wavelength. For example, in a study by Miller *et al.* (1997), a forest fire smoke plume above northern / central Canada caused an increase in scattering that was not constant across the 0.403 – 0.916 μm range. Specifically, scattering was more pronounced for visible than near infrared wavelengths.

The magnitude of aerosol attenuation is generally not constant with wavelength; commonly, attenuation increases towards shorter wavelengths. Researchers studying the effects of pollutant aerosols on irradiance have identified this wavelength dependant extinction (Robaa, 2004; Rizk *et al.*, 1985). The wavelength dependence of pyrogenic aerosols generated by forest fires and biomass burning has been identified from studies of aerosol optical depth (AOD) (Pueschel *et al.*, 1988; Eck *et al.*, 1999). From Pueschel *et al.* (1988), both the type of fuel consumed and the length of time the fire-generated aerosols are suspended within the atmosphere, affect the wavelength dependency. Due to the relatively long atmospheric residence time of the pyrogenic aerosols of interest here (i.e. several days), it is expected that the wavelength dependency will be weaker (i.e. less steep) than if the aerosols were freshly generated (Pueschel *et al.*, 1988).

At the Observatory, daily average and standard deviation values for the AOD (i.e. calculated for cloudless conditions and for $z < 80°$) at 0.368, 0.412, 0.500, 0.675 and

0.778 μm were derived for the same twelve-day observational period displayed in Table 3.4. The values are presented in Table 3.5. AOD measurements were collected using an SPO1A sun photometer. Figure 3.7 presents the average daily AOD at the aforementioned five wavelengths for five days during the spectral measurement period, and two results are immediately apparent. Firstly, AOD values in Figure 3.7 are clearly larger at all wavelengths for days when pyrogenic aerosols are present (i.e. DOY 209,

Table 3.5. Daily average (μ) and standard deviation (σ) of the aerosol optical depth ($z < 80°$) for twelve days when spectral irradiance was measured using the OL 754.

DOY	Wavelength (μm)									
	0.368		0.412		0.500		0.675		0.778	
	μ	σ	μ	σ	μ	σ	μ	σ	μ	σ
196	0.149	0.035	0.125	0.033	0.084	0.027	0.049	0.017	0.041	0.012
203	0.113	0.007	0.097	0.006	0.061	0.004	0.031	0.003	0.041	0.005
205	0.296	0.019	0.252	0.016	0.175	0.011	0.100	0.007	0.082	0.006
209	0.428	0.023	0.364	0.020	0.247	0.013	0.130	0.006	0.099	0.005
211	0.432	0.089	0.370	0.075	0.262	0.054	0.140	0.029	0.105	0.021
212	0.166	0.021	0.144	0.018	0.098	0.015	0.053	0.009	0.043	0.006
222	0.191	0.009	0.169	0.007	0.112	0.005	0.092	0.008	0.055	0.003
225	0.349	0.074	0.295	0.063	0.200	0.042	0.112	0.021	0.091	0.016
226	0.764	0.150	0.649	0.125	0.451	0.090	0.241	0.046	0.180	0.032
227	0.580	0.131	0.496	0.112	0.344	0.087	0.185	0.047	0.142	0.034
230	0.674	0.102	0.580	0.086	0.410	0.062	0.224	0.031	0.167	0.022
231	0.347	0.023	0.309	0.020	0.229	0.014	0.144	0.007	0.121	0.006

226 and 227) than on days when the aerosols are absent (i.e. DOY 196 and 203). From Table 3.5, note that the AOD is also more variable when pyrogenic aerosols are present (i.e. large standard deviations), especially at shorter wavelengths. Temporal fluctuation of the AOD is largely attributable to variable aerosol concentrations within the overlying smoke plumes. Secondly and when compared to aerosol free DOY 196 and DOY 203, it is obvious that attenuation from pyrogenic aerosols is larger at shorter wavelengths, with maximum and minimum AOD values occurring at 0.368 and 0.778 μm respectively. For example, on DOY 226 when pyrogenic aerosols were present and aerosol attenuation was large, the AOD at 0.5 μm was 0.451 and ranged from 0.764 at 0.368 μm to 0.180 at 0.778 μm (Table 3.5).

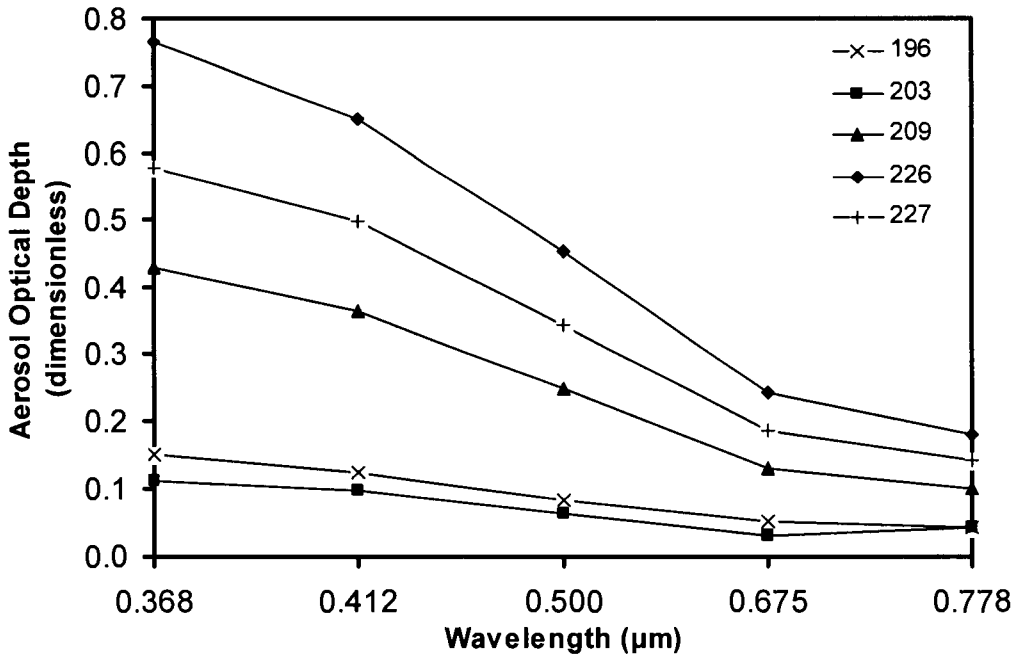

Figure 3.7. Average daily aerosol optical depth ($z < 80°$) for five days during the spectral measurement program. Pyrogenic aerosols are absent on DOY 196 and 203 and present on DOY 209, 226 and 227.

Besides AOD, the wavelength dependency of pyrogenic aerosols can be examined by ratioing two clearness index plots; $c_{i\lambda}$ when pyrogenic aerosols are present to $c_{i\lambda}$ when pyrogenic aerosols are absent (Figure 3.8). From Figure 3.8, pyrogenic aerosol attenuation is not constant from 0.28 to 0.80 μm, with slightly greater attenuation occurring at shorter wavelengths. The increased attenuation at shorter wavelengths is not attributable to differences in ozone concentration between days. This is because the average daily ozone depth (cm) on aerosol-free DOY 203 (i.e. 0.290) is greater than or equal to values measured on DOY 226, 227 and 230 (i.e. 0.290, 0.287 and 0.282 respectively) when pyrogenic aerosols were present.

Surface and extraterrestrial spectral irradiance were integrated and ratioed from 0.28 to 0.80 μm, and across UVB, UVA, violet, blue, green, yellow, orange, red and full spectral bands (Table 3.1) to create a number of clearness indices. Using these spectral bands, the clearness index was calculated for cloudless sky scans obtained during the measurement program. From this dataset, both diurnal and seasonal changes in

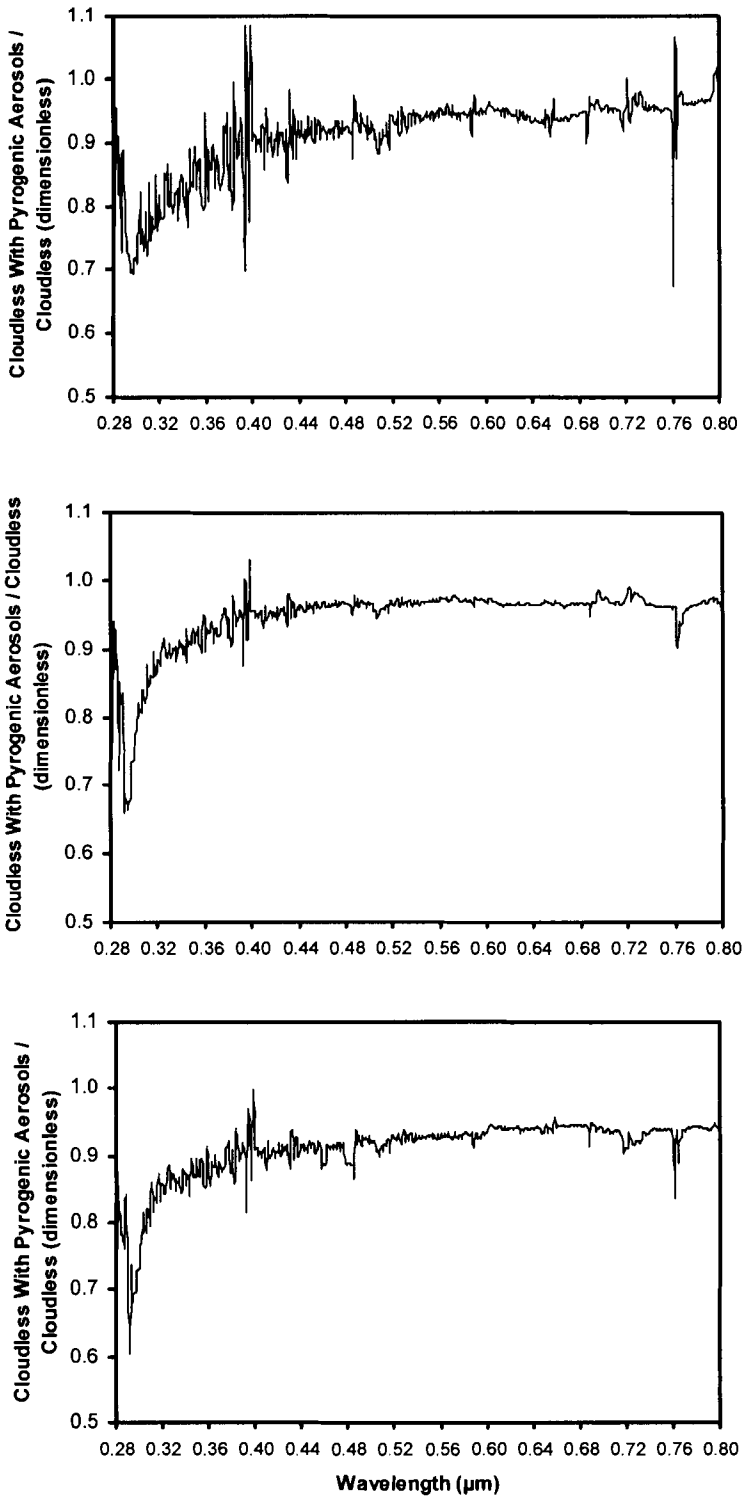

Figure 3.8. Ratio of midday (≈ 12.5 hours, LAT) spectral clearness index plots (cloudless day with pyrogenic aerosols (from top to bottom: DOY 226, 227 and 230) to cloudless day without pyrogenic aerosols (DOY 203)). Note the subtle decrease in the ratio towards shorter wavelengths.

atmospheric attenuation are examined. Figure 3.9 presents the diurnal clearness index (full band: 0.28 – 0.80 μm) for several days throughout the summer measurement program. Here, note the asymmetrical nature to the clearness index on all four days. While this asymmetry is not present on all days, reduced clearness index values during the afternoon suggest that higher aerosol attenuation occurred during the post midday period. However, an examination of diurnal changes in AOD does not entirely support this conclusion, as higher forenoon AOD values actually occurred on DOY 230 and 231.

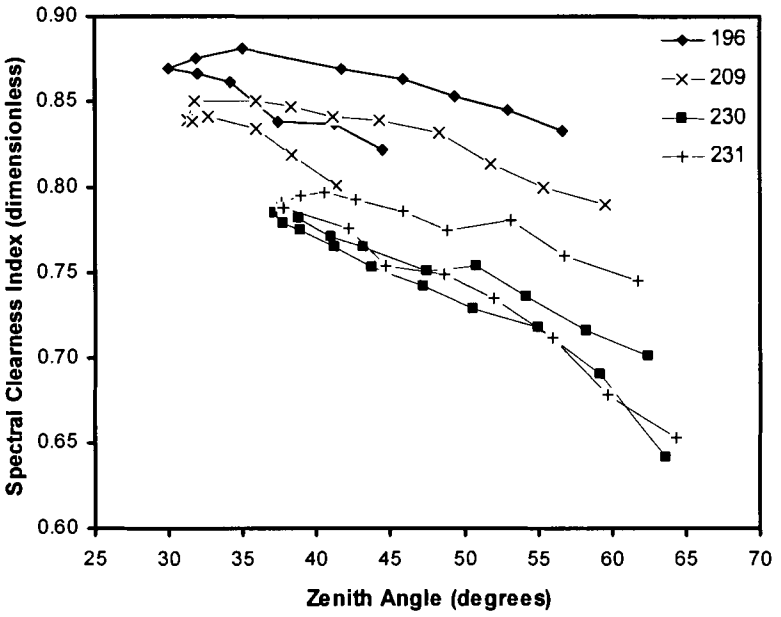

Figure 3.9. Ratio of integrated surface and extraterrestrial spectral irradiance, 0.28 – 0.8 μm ($z < 65°$) for cloudless sky scans collected on DOY 196, 209, 230 and 231 (summer days) in 2003.

In Figure 3.9, note the general decrease in clearness index values throughout the summer of 2003 (i.e. from DOY 196 to DOY 231). While the seasonal clearness index regime is discussed in a following section, the decreasing trend shown in Figure 3.9 is representative of the larger summertime pattern. More specifically, the clearness index (at minimum daily zenith angle (z)) decreased from 0.869 ($z = 30.02°$) on DOY 196 to 0.785 ($z = 37.18°$) on DOY 230. While an increase in optical air mass from DOY 196 to DOY 230 is likely responsible for a portion of this decrease, the change is largely the

result of an overall increase in aerosol optical depth during late July and August 2003. Specifically, the annual cycle of large spring and summertime aerosol optical depths at the Observatory is enhanced by the arrival of pyrogenic aerosol plumes.

Similar to the trends observed in Figure 3.9, both the diurnal asymmetry and summertime decrease in the clearness index are present when examining specific bands. Figure 3.10 shows the diurnal clearness index calculated for UVA, blue and red spectral bands on four days during the summer of 2003. Besides diurnal asymmetry, note how the atmosphere is significantly less transparent to irradiance at UVA wavelengths than to irradiance in blue and red bands. Furthermore, note the general decrease in the clearness index from DOY 196 to DOY 231.

Figure 3.11 provides a more detailed examination of mid-summer clearness index trends at the Observatory. Figure 3.11 is a plot of the average daily clearness index (i.e. calculated for scans: $1 < m < 1.5$) for UVA, violet, blue, green and red spectral bands on 12 days during the summer of 2003 at the Bratt's Lake Observatory (Table 3.6). Here, the clearness index at all spectral bands show a decreasing pattern. The seasonal decrease in the clearness index correlates with an overall increase in the AOD at 0.5 μm during the measurement period (Figure 3.12). While the average daily AOD at 0.5 μm (i.e. calculated during cloudless conditions and for $z < 80°$) increased from 0.084 on DOY 196 to 0.229 on DOY 231, large variability in the AOD (i.e. a range of 0.390) occurred during the 10 observational days between DOY 196 and 231.

From the 12 average daily values presented in Figure 3.12, the mean and standard deviation of the AOD at 0.5 μm for the entire measurement period at the Observatory are 0.223 and 0.128 respectively. By comparison, the mean and standard deviation of the summertime AOD at 0.5 μm observed at Wynyard, Saskatchewan (51° 46′ N, 104° 12′ W) between 1987 and 1991 are only 0.120 and 0.053 respectively (Smirnov *et al.*, 1996). While the above comparison is not perfect (i.e. the mean AOD at 0.5 μm for the Observatory is only representative of 12 summer days), it denotes the strong increase in atmospheric attenuation caused by the pyrogenic aerosols. The contrast in atmospheric attenuation between days when pyrogenic aerosols are present and days when they are absent is denoted by the large standard deviation in the AOD at 0.5 μm for the entire

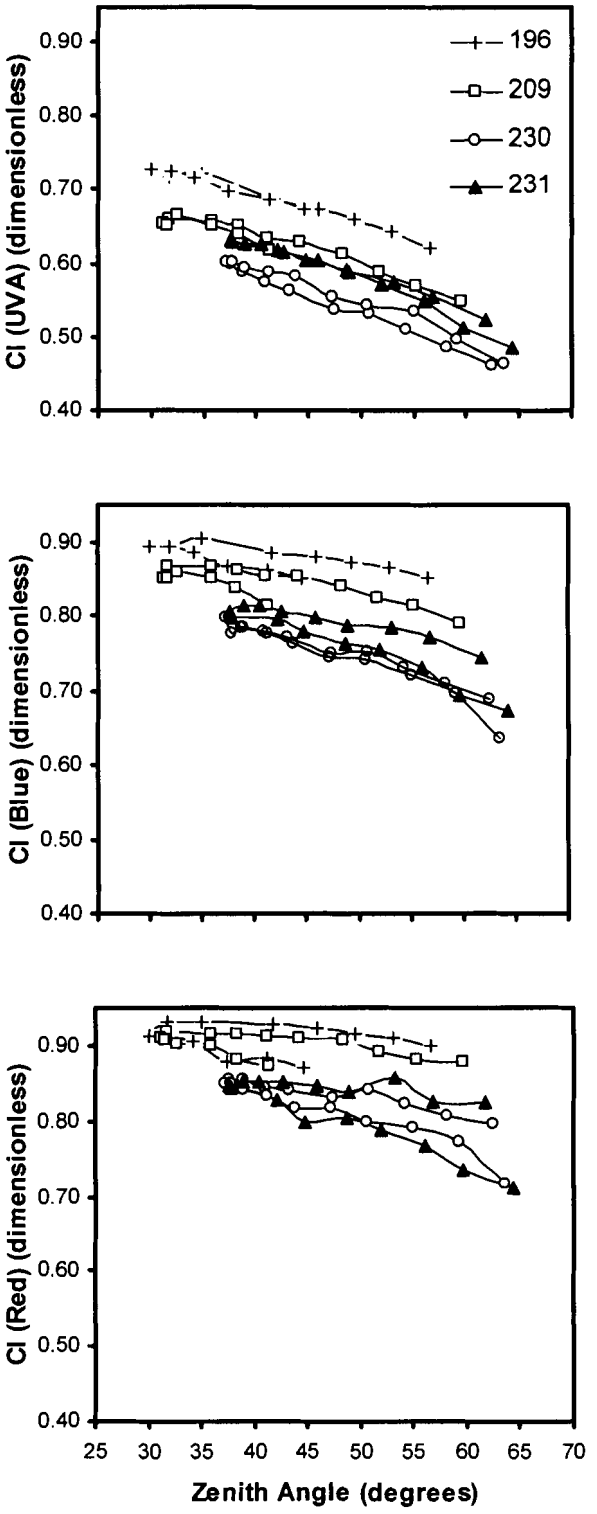

Figure 3.10. Ratio of integrated surface and extraterrestrial spectral irradiance, for UVA, blue and red spectral bands ($z < 65°$) on DOY 196, 209, 230 and 231 at the Bratt's Lake Observatory.

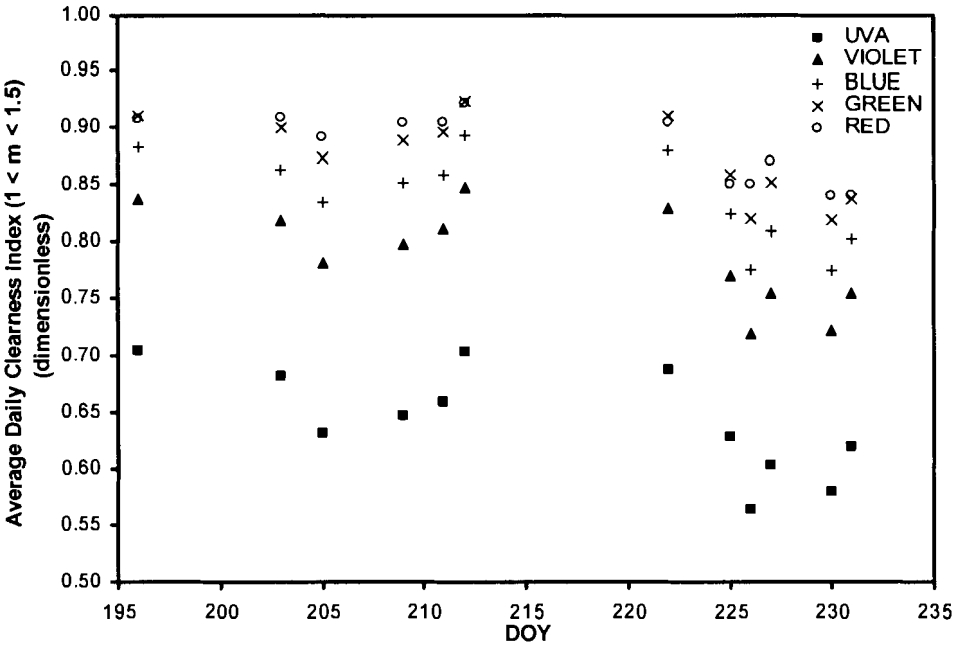

Figure 3.11. Average daily clearness index (1 < m < 1.5) for UVA, violet, blue, green and red spectral bands at the Bratt's Lake Observatory. Note the generally decreasing trend in the clearness index for all spectral bands from DOY 196 to DOY 231.

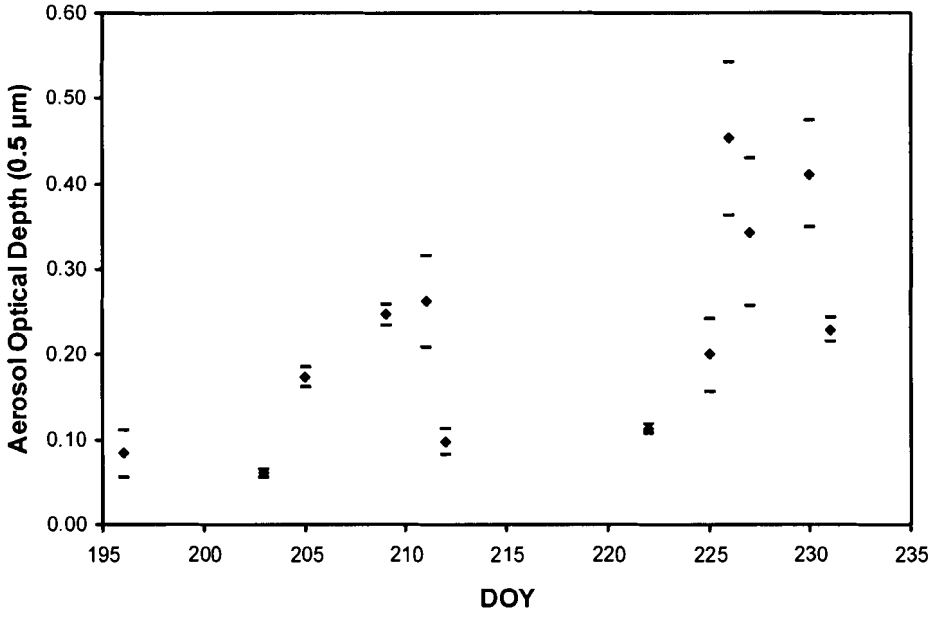

Figure 3.12. Average daily aerosol optical depth at 0.5 µm (z < 80°) for the 12 days when spectral measurements were collected with the OL 754. Horizontal bars represent ± one standard deviation.

measurement period. On a diurnal basis, AOD values generally display large standard deviations when pyrogenic aerosols are present (Figure 3.12). Such variability in the AOD at 0.5 μm suggests that aerosol concentrations within a plume are not uniform; instead, concentrations may vary substantially over time.

By definition, and from Figures 3.11 and 3.12, an inverse relationship exists between the clearness index and the AOD at 0.5 μm; with high clearness index values corresponding to low AOD values, and low clearness index values corresponding to high AOD values. Figure 3.13 is a plot of the average daily clearness index (full band: 0.28 – 0.80 μm) versus the average daily AOD at 0.5 μm. From Figure 3.13, it is apparent that a relatively strong inverse relationship exists between the two variables. Furthermore, the relationship between the clearness index and AOD can be approximated reasonably well (i.e. coefficient of determination equal to 0.709) by a linear function.

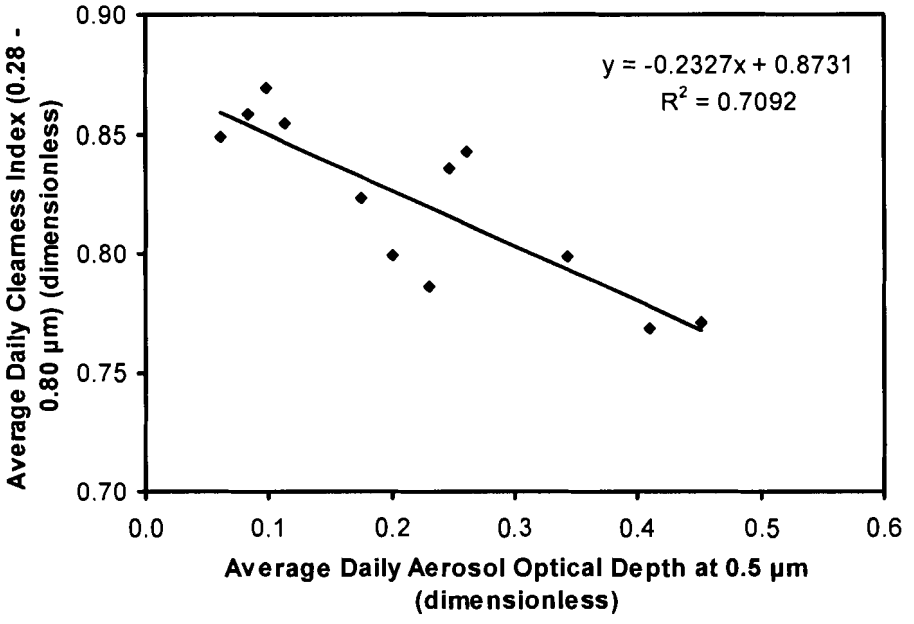

Figure 3.13. The relationship between average daily clearness index ($1 < m < 1.5$) and average daily AOD at 0.5 μm ($z < 80°$). Trend line (and equation of line) and coefficient of determination are included in Figure.

The relatively large clearness index values that occurred on DOY 212 and 222 seem nonsensical at first (i.e. haze was recorded on both days) (i.e. Table 3.4). However,

the low AOD on both DOY 212 and 222 (i.e. 0.0978 and 0.1122 respectively) support the high clearness index values and suggests that cleaner air moved over the Observatory. While back trajectory analysis (i.e. Appendix 2) shows that airflow at the 700 and 850 hPa surfaces is coming from aerosol source regions on DOY 222, the easterly airflow at 925 hPa likely contributes to the cleaner atmospheric conditions (i.e. the low AOD). Furthermore, back trajectory analysis conducted on DOY 212 reveals strong easterly flow of air at all pressure surfaces.

From the above discussion, it is clear that pyrogenic aerosols attenuate irradiance across the 0.28 – 0.80 μm spectral range (i.e. Figure 3.6). Furthermore, and as previously discussed, Figures 3.7 and 3.8 show that irradiance attenuation from pyrogenic aerosols is wavelength dependant. These arguments are now more closely examined using the percentage change in the clearness index between DOY 196 and eight days on which pyrogenic aerosols are present (i.e. DOY 205, 209, 211, 225, 226, 227, 230 and 231) (Table 3.7). From the data presented in Table 3.7, note that average daily clearness index values are distinctly lower for spectral bands when pyrogenic aerosols are present (i.e. negative percentage change values). Also, note that the percentage change becomes greater (i.e. more negative) towards shorter wavelength bands (i.e. violet, UVA and UVB). With respect to the entire 0.28 – 0.80 μm band (i.e. Table 3.7), pyrogenic aerosols contribute to a reduction in the clearness index ranging from 1.8 % (i.e. on DOY 211) to 10.4 % (i.e. on DOY 230). A graphical summary of the results in Tables 3.6 and 3.7 appears in Figure 3.14. The data in Figure 3.14 was derived as a ratio of the average daily clearness index for UVB, UVA, violet, blue, green, yellow, orange, red and NIR spectral bands (i.e. Table 3.6) when pyrogenic aerosols are present to the average daily clearness index when pyrogenic aerosols are absent (i.e. DOY 203). In Figure 3.14, note that ratio values are smallest at the shortest wavelength bands (i.e. at UVB, UVA and violet bands) while larger at longer wavelength bands.

In the preceding chapter, the daily broadband clearness index for 2003 was presented and seasonal trends were analyzed. Specifically, midsummer broadband clearness index values showed a decreasing trend. Similar to the broadband clearness index, spectral clearness index values (i.e. in Figures 3.9, 3.10, 3.11, 3.12 and Tables 3.6

Table 3.6. Average daily clearness index ($1 < m < 1.5$) for UVB, UVA, violet, blue, green, yellow, orange, red, NIR and full spectral bands.

		Day Of Year											
Band Name	Spectral Range (μm)	196	203	205	209	211	212	222	225	226	227	230	231
UVB	0.280 - <0.315	0.081	0.081	0.062	0.070	0.064	0.074	0.077	0.071	0.059	0.064	0.063	0.070
UVA	0.315 - <0.400	0.704	0.680	0.630	0.647	0.659	0.703	0.686	0.628	0.563	0.602	0.580	0.619
Violet	0.400 - <0.455	0.837	0.818	0.782	0.797	0.811	0.847	0.829	0.770	0.718	0.753	0.721	0.754
Blue	0.455 - <0.492	0.882	0.864	0.834	0.852	0.860	0.893	0.880	0.823	0.775	0.810	0.775	0.802
Green	0.492 - <0.577	0.911	0.901	0.874	0.889	0.895	0.924	0.911	0.859	0.820	0.852	0.818	0.837
Yellow	0.577 - <0.597	0.902	0.895	0.868	0.888	0.889	0.913	0.902	0.841	0.829	0.853	0.820	0.829
Orange	0.597 - <0.622	0.923	0.918	0.897	0.908	0.911	0.934	0.925	0.870	0.855	0.874	0.849	0.859
Red	0.622 - <0.770	0.908	0.910	0.891	0.904	0.904	0.922	0.905	0.850	0.851	0.870	0.840	0.841
NIR (Portion only)	0.770 - <0.800	0.967	0.968	0.964	0.969	0.976	0.983	0.968	0.920	0.921	0.929	0.903	0.896
Full Band	0.280 - <0.800	0.858	0.849	0.823	0.836	0.843	0.869	0.854	0.799	0.771	0.799	0.769	0.785

Table 3.7. Percentage change of the average daily clearness index (Table 3.6) for UVB, UVA, violet, blue, green, yellow, orange, red, NIR and full spectral bands on eight days when pyrogenic aerosols are present (DOY 205, 209, 211, 225, 226, 227, 230 and 231) from the clearness index on DOY 196 when pyrogenic aerosols are absent.

		Day Of Year With Pyrogenic Aerosols							
Band Name	Spectral Range (μm)	205	209	211	225	226	227	230	231
		% Change ((Aerosol DOY - DOY 196) / DOY 196) * 100							
UVB	0.280 - <0.315	-23.151	-12.854	-20.402	-12.121	-26.901	-20.231	-21.705	-13.293
UVA	0.315 - <0.400	-10.396	-8.038	-6.358	-10.746	-19.941	-14.409	-17.583	-11.965
Violet	0.400 - <0.455	-6.573	-4.721	-3.142	-8.018	-14.188	-9.991	-13.813	-9.920
Blue	0.455 - <0.492	-5.487	-3.433	-2.556	-6.659	-12.139	-8.196	-12.190	-9.128
Green	0.492 - <0.577	-4.058	-2.401	-1.717	-5.705	-10.019	-6.501	-10.207	-8.101
Yellow	0.577 - <0.597	-3.829	-1.586	-1.493	-6.772	-8.141	-5.483	-9.117	-8.114
Orange	0.597 - <0.622	-2.865	-1.634	-1.368	-5.798	-7.397	-5.303	-8.084	-6.945
Red	0.622 - <0.770	-1.848	-0.418	-0.430	-6.342	-6.302	-4.146	-7.509	-7.428
NIR (Portion only)	0.770 - <0.800	-0.382	0.135	0.926	-4.895	-4.776	-4.014	-6.624	-7.390
Full Band	0.280 - <0.800	-4.088	-2.533	-1.786	-6.851	-10.129	-6.923	-10.418	-8.482

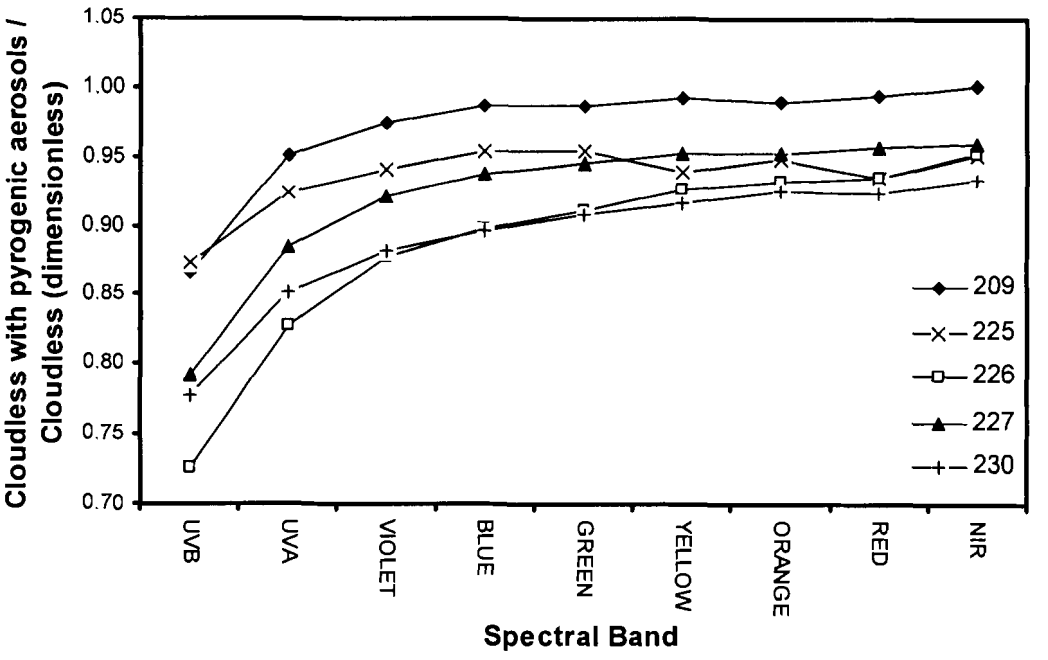

Figure 3.14. Ratio of the average daily clearness index ($1 < m < 1.5$) for ultraviolet, visible and NIR (portion only) bands when pyrogenic aerosols are present (DOY 209, 225, 226, 227, 230 and 231) to the average daily clearness index when pyrogenic aerosols are absent (DOY 203).

and 3.7) suggest a general decreasing summertime regime from DOY 196 to DOY 231. Figure 3.15 provides a comparison between daily broadband (i.e. surface irradiance measured from 0.305 to 2.8 μm) and spectral (i.e. surface irradiance measured and integrated from 0.28 – 0.80 μm) clearness index values from DOY 196 to DOY 231. Despite the difference in spectral range, Figure 3.15 shows that both clearness index regimes correlate well, with broadband and spectral clearness index values decreasing from 0.744 and 0.858 respectively on DOY 196 to 0.701 and 0.785 on DOY 231.

3.5. Conclusions

Spectral global irradiance from 0.28 to 0.80 μm under cloudless skies was measured at Environment Canada's Bratt's Lake Observatory and diurnal and seasonal regimes were analyzed and presented using the clearness index. Measurements were collected with a horizontally based OL 754 Spectroradiometer from June 15 to August

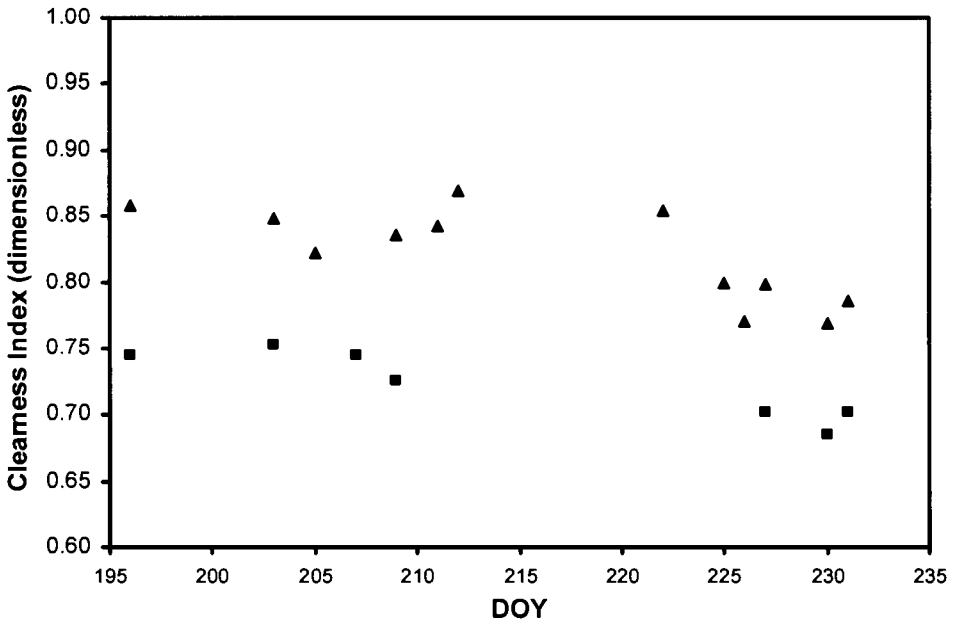

Figure 3.15. Daily broadband and average daily spectral clearness index ($1 < m < 1.5$) at the Bratt's Lake Observatory. Note: spectral (▲) and broadband (■) clearness index values are calculated from 0.28 – 0.80 μm and 0.305 – 2.8 μm spectral ranges respectively.

22, 2003. The spectral distribution of global irradiance at the surface showed high amplitude variability that is attributable to both solar (i.e. Fraunhofer lines) and terrestrial (i.e. molecular absorbers) absorption features. At the Earth's surface, H_2O and O_2 absorption cause distinct troughs (i.e. at 0.72 μm and 0.63, 0.69 and 0.76 μm respectively) that characterize the spectral distribution of global irradiance from 0.28 to 0.80 μm. Diurnal variation in the magnitude of spectral global irradiance is largely attributable to optical air mass, although an increase in convective turbulence or change in the flow of air (i.e. aerosol advection) may also contribute.

Pyrogenic aerosol effects on spectral global irradiance were assessed from clearness index values calculated for individual spectra and integrated bands from 0.28 to 0.80 μm. From this analysis, aerosol attenuation showed a wavelength dependency from 0.28 to 0.80 μm, with greater reduction in surface irradiance occurring at shorter wavelengths (i.e. towards the ultraviolet). The wavelength dependence of these pyrogenic aerosols was also evident from AOD measurements made at 0.386, 0.412,

0.500, 0.675 and 0.778 μm. On days when pyrogenic aerosols were present, the AOD showed a large difference between 0.386 and 0.778 μm, with shorter wavelengths having greater optical depths than longer wavelengths.

Calculation of the clearness index for UVB, UVA, violet, blue, green, yellow, orange, red and full spectral bands made possible an examination of diurnal and seasonal global irradiance regimes. While diurnal regimes showed asymmetry from forenoon to afternoon periods, with lower clearness index values typically occurring in the afternoon, these results did not always coincide with diurnal changes in the aerosol optical depth at 0.5 μm. With respect to the seasonal regime, the average daily spectral clearness index from 0.28 to 0.80 μm showed a decrease throughout the summer measurement period, from 0.858 on DOY 196 to 0.785 on DOY 231. This decrease agreed well with the pattern seen in the broadband clearness index, which decreased from 0.785 on DOY 196 to 0.701 on DOY 231. Alternately, the average daily aerosol optical depth at 0.5 μm increased from 0.084 on DOY 196 to 0.230 on DOY 231. Furthermore, the inverse relationship between the average daily spectral clearness index (0.28 – 0.80 μm) and the average daily aerosol optical depth at 0.5 μm was well approximated (i.e. coefficient of determination equal to 0.709) by a linear function.

Chapter 4.
Conclusions

4.1. Introduction

This research sought to characterize broadband and spectral global solar irradiance in a southern Saskatchewan prairie environment. Specifically, there were two major objectives of this research. The first objective was to analyze diurnal and seasonal regimes of cloudless sky global, direct and diffuse irradiance from one-minute data collected throughout 2003 at Environment Canada's Bratt's Lake Observatory. Additionally, a cloudless sky global irradiance model based on Houghton (1954) was employed, and results were validated against cloudless sky observations. Despite several known deficiencies in Houghton's modelling approach, one-minute estimates of global, direct and diffuse irradiance proved accurate, especially during the late spring, summer and early autumn. An examination of the broadband aerosol optical depth (Unsworth and Monteith, 1972) yielded insight into the annual and diurnal cycles of aerosol attenuation at the Observatory. Overall, the atmosphere in southern Saskatchewan was remarkably clean, with the exception of several days in mid to late July and August, when pyrogenic aerosols from upwind wildfires caused an increase in atmospheric turbidity.

The second objective involved an empirical and numerical study of spectral global irradiance from 0.28 to 0.80 μm employing spectral measurements collected during the summer of 2003. The spectral distribution of global irradiance from 0.28 to 0.80 μm was characterized by absorption within both solar (i.e. Fraunhofer lines) and terrestrial (i.e. molecular absorbers) atmospheres. An examination of the spectral clearness index and aerosol optical depth revealed further information about atmospheric attenuation at the Observatory. Throughout the measurement program, attenuation levels were variable, largely due to the rise in absorption and scattering on days when pyrogenic aerosols were present. More specifically, and in agreement with the findings of Pueschel *et al.* (1988), the pyrogenic aerosols displayed wavelength dependant extinction, with

attenuation increasing towards shorter wavelengths. While the two research objectives denoted above are inherently related, the major theme common to both objectives is the strong influence of pyrogenic aerosol plumes on both diurnal and seasonal broadband and spectral irradiance regimes.

4.2. Seasonal and Diurnal Cloudless Sky Broadband Global Irradiance Regimes in Southern Saskatchewan, Canada

This chapter examined cloudless sky broadband irradiance from both a measurement and modelling perspective. One-minute cloudless sky measurements of global, direct and diffuse irradiance for 2003 were used to identify diurnal and season irradiance regimes. While surface irradiance regimes track extraterrestrial irradiance throughout most of 2003, significant variability in direct and diffuse irradiance occurred during a mid-summer period of increased optical depth caused by pyrogenic aerosols. The global irradiance regime shows less variability during this period, due to an increase in the diffuse flux that compensated for the strong aerosol depletion of direct irradiance. In addition to pyrogenic aerosols, optical air mass also exerted significant influence in shaping diurnal and seasonal irradiance patterns.

The effect of optical air mass and pyrogenic aerosols on the amount of broadband irradiance reaching the surface was examined using the clearness index, transmissivity and diffuse ratio. The average daily cloudless sky clearness index and transmissivity in 2003 were found to be 0.75 and 0.60 respectively. The average daily cloudless sky diffuse ratio for 2003 is 0.13. Deviation from these average values is strongest during two periods of the year: 1) throughout the winter and autumn, and 2) during the mid-summer pyrogenic aerosol event. During winter and autumn periods, daily clearness index and transmissivity dropped as low as 0.70 and 0.52 respectively, while diffuse ratio values reached as high as 0.18. As shown graphically within the text, these changes were clearly attributable to the seasonal increase in the average daily optical air mass. During summer days when pyrogenic aerosols were present, daily clearness index and transmissivity dropped as low as 0.69 and 0.47 respectively, while diffuse ratio values reached as high as 0.20. As average daily optical air mass values remained relatively

constant during the summer, these changes are attributable to an increase in both scattering and absorption by pyrogenic aerosols.

Under cloudless conditions, diurnal changes in optical air mass form an irradiance regime that is principally symmetrical about solar noon. The diurnal symmetry in global, direct and diffuse irradiance is also apparent in the clearness index, transmissivity and diffuse ratio. While the clearness index and transmissivity show symmetry about a diurnal maximum at solar noon, the diffuse ratio shows symmetry about a diurnal minimum at solar noon. However, close examination of these patterns reveal that changing atmospheric composition, from forenoon to afternoon periods, introduces slight asymmetry to the cloudless sky diurnal irradiance regime. Diurnal changes in atmospheric composition can arise from both increased convective turbulence during afternoon periods (Latha and Badarinath, 2004), and, when pyrogenic aerosols are present, to strong temporal variability in the aerosol optical depth (Markham *et al.*, 1997; Gutro *et al.*, 2002).

In the past, estimates from the Houghton (1954) model have performed well at predicting global irradiance at individual locations over daily and monthly periods (Davies *et al.*, 1975; Monteith, 1962; Idso, 1970). This research has applied the Houghton (1954) model to estimate one-minute global, direct and diffuse irradiance at a location in southern Saskatchewan. The accuracy of one-minute irradiance estimates was assessed using the MBE, MAE, RMSE and d. During late spring, summer and early autumn periods, model estimates of global, direct and diffuse irradiance are accurate (i.e. summertime RMSE values ranging from 7.6 W m^{-2} and 11.9 W m^{-2} for global). The good performance is largely because the average dust factor during this period at the Observatory ($k = 0.94$) approaches the dust factor employed by Houghton (1954) ($k = 0.95$).

Alternately, model estimations were least accurate during the winter and late autumn (i.e. RMSE values ranging from 17.1 W m^{-2} and 41.7 W m^{-2} for global) and during the mid-summer pyrogenic aerosol event (i.e. RMSE values ranging from 12.0 W m^{-2} to 26.3 W m^{-2} for global). During the winter period, model underestimation of global and direct irradiance is also largely attributable to the model's inadequate aerosol

parameterization. Houghton's constant aerosol parameterization does not adequately account for reduced wintertime aerosol concentrations. Specifically, broadband aerosol optical depth (Unsworth and Monteith, 1972) values at the Observatory indicate that aerosol attenuation changes with season, with generally larger values occurring in the spring and summer and smaller values occurring in the winter. The limitations inherent in Houghton's original parameterization necessitated the development of a revised aerosol parameterization. For winter and late autumn periods, a dust factor value equal to 0.973 is more adequate.

During the pyrogenic aerosol period, deviation between predicted and observed irradiance values was also largely due to an inadequate dust factor. This research suggests that a dust factor value equal to 0.846 is more appropriate when pyrogenic aerosols are present. Model overestimation of global and direct irradiance during this period is attributable to increased absorption and scattering by pyrogenic aerosols. Maximum aerosol depletion of global and direct irradiance, above normal background levels, occurred on DOY 230 where irradiance deficits of 3.4% and 23.1% occurred respectively. Likewise, model underestimation of diffuse irradiance is attributable to increased scattering by the pyrogenic aerosols. The maximum spike in diffuse irradiance from pyrogenic aerosols occurred on DOY 209, when diffuse irradiance increased by 50.2% relative to normal background levels.

4.3. Cloudless Sky Spectral Global Irradiance Regime in Southern Saskatchewan, Canada

In response to the current shortfall in spectral measurement programs for many geographic locations (Betts *et al.*, 2001), Chapter 3 provided a discussion of spectral global irradiance (i.e. spectral range: 0.28 – 0.80 μm) data collected from June 15 to August 22, 2003, at Environment Canada's BSRN Bratt's Lake Observatory in southern Saskatchewan. An Optronic Laboratories OL 754 Spectroradiometer was employed to measure cloudless sky spectral global irradiance. Both solar (i.e. Fraunhofer lines) and terrestrial absorption features (i.e. molecular absorbers) are evident over the 0.28 to 0.80 μm spectral range. Despite the importance of solar absorption in shaping the spectral distribution of global irradiance at the Earth's surface, the spectra between 0.28 – 0.80

μm is characterized by H_2O and O_2 absorption bands centred at 0.72 μm and 0.63, 0.69 and 0.76 μm respectively. Besides molecular absorption, molecular scattering and aerosol scattering and absorption also reduce the magnitude of extraterrestrial irradiance reaching Earth's surface. The magnitude of this attenuation is also dependant on diurnal changes in optical air mass.

Calculation of the clearness index for both individual spectra and spectral bands provide further insight into atmospheric attenuation at the Observatory. The clearness index was derived using the 2003 synthetic Gueymard extraterrestrial spectrum. This ratio was particularly useful in quantifying the effects of pyrogenic aerosols on spectral global irradiance. During the summer of 2003, wildfires burned throughout regions of British Columbia and the states of Washington, Oregon, Idaho and Montana (Appendix 2). Due to these fires, large pyrogenic aerosol (smoke) plumes were injected into the atmosphere and prevailing westerly winds moved these aerosols hundreds of kilometres eastward into southern Saskatchewan. The arrival of pyrogenic aerosol plumes at the Observatory in late July and August was denoted by three events: 1) the presence of haze, 2) a decrease in the spectral clearness index and 3) an increase in the aerosol optical depth.

Pyrogenic aerosol effects on spectral global irradiance were observed across the entire 0.28 – 0.80 μm range. However, an examination of the clearness index and aerosol optical depth at several wavelengths identified that aerosol attenuation was not uniform across this spectral range, with enhanced attenuation occurring at shorter wavelengths. Given the relatively long time the aerosols spent within the atmosphere (i.e. several days), the wavelength dependency at the Observatory was likely less steep than if the aerosols were freshly generated (Pueschel *et al.*, 1988). Calculation of the clearness index for spectral bands enabled diurnal and seasonal global irradiance trends to be examined. Generally, the diurnal global irradiance regime showed asymmetry from forenoon to afternoon periods, with lower clearness index values often occurring in the afternoon. Contrary to most of these patterns, aerosol optical depth values were often lower during afternoon periods. With respect to the seasonal regime, spectral clearness index values decreased throughout the summer measurement period, from 0.858 on DOY 196 to 0.785 on DOY 231. Furthermore, and similar to the decrease in the spectral

clearness index, broadband clearness index values decreased from 0.744 on DOY 196 to 0.701 on DOY 231.

The average daily aerosol optical depth at 0.5 μm showed an increasing pattern throughout the measurement period, from 0.084 on DOY 196 to 0.230 on DOY 231. While the total increase is dramatic, even larger variability in the AOD occurred during the 10 observational days between DOY 196 and 231 (i.e. a range of 0.391), from characteristically low background values when the pyrogenic aerosols were absent (Smirnov *et al.*, 1996) to high values when the pyrogenic aerosols were present. Results obtained by Holben *et al.* (2001), link similar behaviour in summertime aerosol optical depth values measured at 0.5 μm at a site in Thompson, Manitoba to forest fire activity. The mean and standard deviation of the AOD at 0.5 μm for the entire measurement period at the Observatory are 0.223 and 0.128 respectively. Both of these values are large by comparison to those observed by Smirnov *et al.* (1996) at Wynyard, Saskatchewan (51° 46′ N, 104° 12′ W) between 1987 and 1991, a difference denoting the strong increase in atmospheric attenuation caused by the pyrogenic aerosols.

As expected, the clearness index and the AOD at 0.5 μm displayed an inverse relationship; with high clearness index values corresponding to low AOD values, and low clearness index values corresponding to high AOD values. This relationship was approximated reasonably well (i.e. coefficient of determination equal to 0.709) by a linear function.

Appendix 1.
List of Symbols and Units

Roman upper case

D	diffuse irradiance on a horizontal surface (W m^{-2}, MJ m^{-2} d^{-1})
D_o	cloudless sky diffuse irradiance on a horizontal surface (W m^{-2}, MJ m^{-2} d^{-1})
E_o	eccentricity correction factor (dimensionless)
G_λ	spectral global irradiance on a horizontal surface (W m^{-2} μm^{-1})
I_o	solar constant (W m^{-2})
$I_{On\lambda}$	extraterrestrial spectral irradiance at mean sun – earth distance on a surface perpendicular to the sun's rays (W m^{-2} μm^{-1})
$K\downarrow$	global irradiance on a horizontal surface (W m^{-2}, MJ m^{-2} d^{-1})
$K_o\downarrow$	cloudless sky global irradiance on a horizontal surface (W m^{-2}, MJ m^{-2} d^{-1})
K_{EX}	extraterrestrial radiation (W m^{-2}, MJ m^{-2} d^{-1})
L	mean longitude (degrees)
LAT	local apparent time (hours)
L_E	local station longitude (degrees)
L_S	standard longitude (degrees)
LST	local standard time (hours)
MAE	mean absolute error (W m^{-2})
MBE	mean bias error (W m^{-2})

N	number of predicted and observed values
O_i	observed irradiance (W m^{-2})
P_i	predicted irradiance (W m^{-2})
RMSE	root mean square error (W m^{-2})
R_z	Zurich sunspot number
R_λ	OL-754 system irradiance response (calibration factor) [(W m^{-2} μm^{-1}) / A]
S	direct irradiance on a horizontal surface (W m^{-2}, MJ m^{-2} d^{-1})
S_o	cloudless sky direct irradiance on a horizontal surface (W m^{-2}, MJ m^{-2} d^{-1})
S_{oa}	cloudless sky direct irradiance on a horizontal surface for an aerosol free atmosphere (W m^{-2}, MJ m^{-2} d^{-1})
S_λ	OL-754 raw spectral global irradiance signal (Amps)
TSI	total solar irradiance (W m^{-2})
U_o	ozone depth (cm)

Roman lower case

c_i	clearness index (dimensionless)
$c_{i\lambda}$	spectral clearness index (dimensionless)
d	index of agreement (dimensionless)
d_n	day-of-year (DOY)
d_r	diffuse ratio (dimensionless)
ep	obliquity of the ecliptic (degrees)
et	equation of time (minutes)
g	mean anomaly (degrees)

h	hour angle (degrees)
jd	julian date
k	dust factor (dimensionless)
m	optical air mass (dimensionless)
n	time (includes fractional day correction)
t	transmissivity (dimensionless)
wm	water mass (cm)
z	solar zenith angle (degrees)

Greek upper case

ϕ_d	transmission due to dust attenuation (dimensionless)
ϕ_{da}	transmission due to dust absorption (dimensionless)
ϕ_{ds}	transmission due to dust scattering (dimensionless)
ϕ_{o_3}	transmission due to ozone absorption (dimensionless)
ϕ_{rs}	transmission due to Rayleigh scattering (dimensionless)
ϕ_{wa}	transmission due to water vapour absorption (dimensionless)
ϕ_{ws}	transmission due to water vapour scattering (dimensionless)

Greek lower case

δ	solar declination (degrees)
ε	eccentricity of the Earth's elliptical orbit (0.01675)
ι	ecliptic longitude (degrees)
λ	wavelength (μm)
τ_a	aerosol optical depth (dimensionless)

ϕ station latitude (degrees)

ω Earth's angular velocity (2π / 365 rad d^{-1})

Appendix 2.
Overview of the 2003 Wildland Fire Season in Northwestern Regions of North America and Movement of Associated Pyrogenic Aerosol Plumes

During the summer of 2003, large wildland fires raged across northwestern regions of North America. A wildland fire is defined as any non-structure, non-prescribed fire that occurs in the wildland (National Interagency Coordination Center, 2003). The wildland includes forest, range and grassland ecosystems (McMahon, 1999). Wildland fire activity continued in northwestern regions throughout July, August and September. The severity of the 2003 fire season was, in part, due to the unusually hot and dry summer conditions that persisted in the northwest. In the northwestern United States, the hot and dry meteorological conditions were linked to a ridge of high pressure that formed over the Great Basin region during the summer (National Interagency Coordination Center, 2003; Gleason *et al.*, 2004). This ridge of high pressure not only resulted in near record high temperatures for the state of Washington, but in many northwestern states. In fact, the summer of 2003 brought above average temperatures to regions west of the Rocky Mountains (Gleason *et al.*, 2004). Furthermore, 2003 was the driest on record for the state of Washington (National Interagency Coordination Center, 2003). Besides Washington, wildland fire activity was prominent throughout regions of Oregon, Idaho and Montana (National Interagency Coordination Center, 2003) (Figure A2.1).

Within Canada, western provinces also experienced above normal average temperatures in 2003, with especially warm conditions occurring in the Okanagan River valley region in southern British Columbia (Filmon, 2004; Levinson and Phillips, 2004). Throughout 2003, drier than average conditions occurred from the Prairie Provinces through to the coast of British Columbia (Levinson and Phillips, 2004). In British Columbia, these hot and dry conditions contributed to the approximately 2500 wildfires

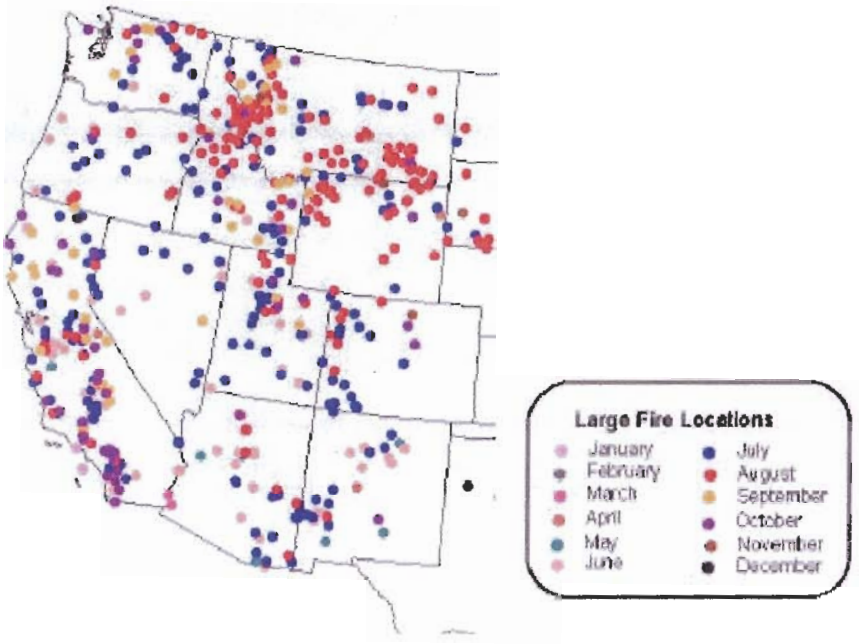

Figure A2.1. Map of western regions in the United States, showing location of large wildland fires in 2003. Source: National Interagency Coordination Center, 2003.

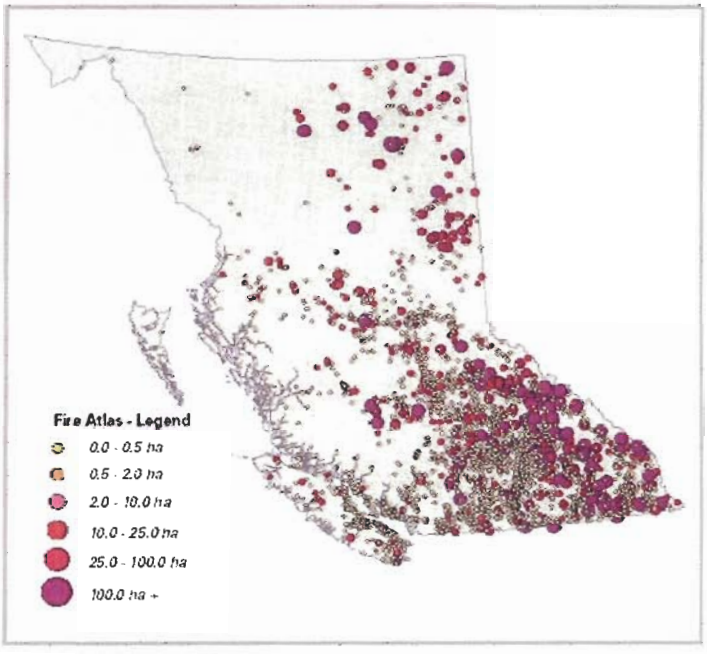

Figure A2.2. Map of British Columbia, Canada showing location and size of the 2003 wildfires. Source: Filmon, 2004. Copyright © Province of British Columbia. All rights reserved. Reprinted with permission of the Province of British Columbia.

that burned province wide, making the summer of 2003 the worst ever fire season on record in British Columbia (Figure A2.2) (Filmon, 2004; Levinson and Phillips, 2004). Concentrated in interior regions, the fires consumed more than 6863 km^2 (686,347 ha) of forest, rangeland and residential areas province wide (Levinson and Phillips, 2004). While significant amounts of dead underbrush was consumed by the fires, a large number of Douglas fir and lodge pole pine species were also burnt. The extreme heat generated at the surface from these fires lifted large quantities of pyrogenic (smoke) particles into the atmosphere by intense surface convection.

From the major source regions in British Columbia, Washington, Oregon, Idaho and Montana, prevailing westerly winds carried these aerosols in a predominantly eastward direction into Canada's Prairie Provinces and over the Bratt's Lake Observatory in Saskatchewan. Figures A2.3 through A2.12[1] provide back trajectories for a series of days (i.e. DOY 205, 209, 211, 212, 222, 225, 226, 227, 230 and 231) during which broadband and / or spectral measurements were collected. These figures show the flow of air at the 700, 850 and 925 hPa pressure surfaces (note: back trajectory data was provided by the Canadian Meteorological Centre and was plotted by E. Wu using the program TrajPlot3.0, written by J. D. MacNeil and B. Pabla). The back trajectories link the presence of white haze at the Observatory to scattering by pyrogenic aerosols produced by wildland fires in the United States and Canada (i.e. DOY 205, 209, 226, 227 and 230). Furthermore, they validate the large aerosol optical depth values that occur in late July and August. Finally, change in the direction and movement of airflow at the three pressure surfaces, away from pyrogenic aerosol source regions, are responsible for periods of reduced optical depth during late July and early August (i.e. DOY 212 and to a lesser extent DOY 222).

[1] The data in Figures A2.3 through A2.12 is not represented as an official version of the data produced, nor as having been made in affiliation with, or with the endorsement of, Environment Canada.

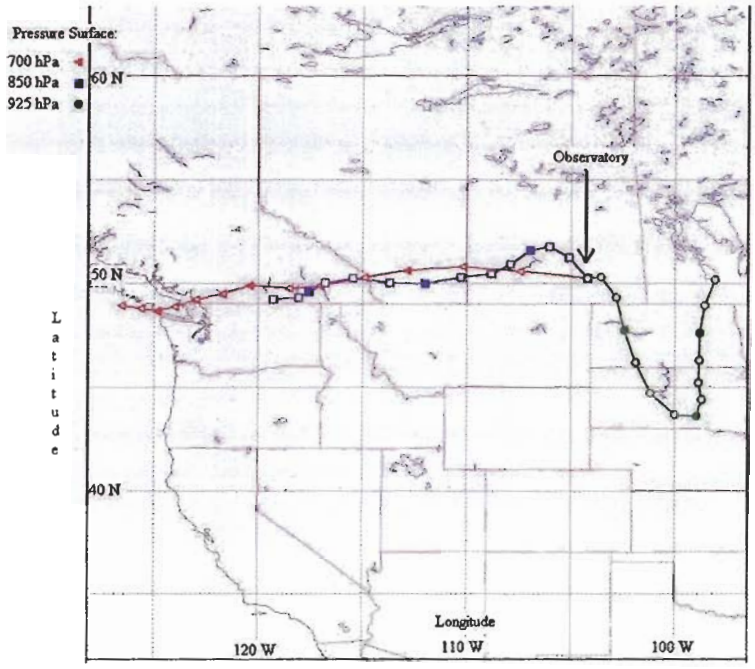

Figure A2.3. Back trajectory analysis for DOY 205 (July 24) at 18Z (UTC) showing flow (in 6 hour intervals) from pyrogenic aerosol source regions. Source: Jacinthe Racine, Canadian Meteorological Centre, Environment Canada.

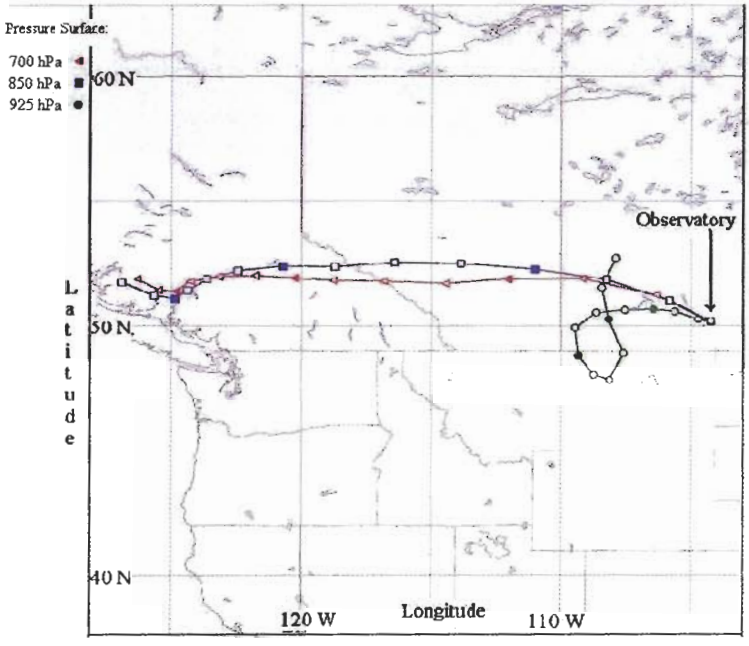

Figure A2.4. Back trajectory analysis for DOY 209 (July 28) at 18Z (UTC) showing flow (in 6 hour intervals) from pyrogenic aerosol source regions. Source: Jacinthe Racine, Canadian Meteorological Centre, Environment Canada.

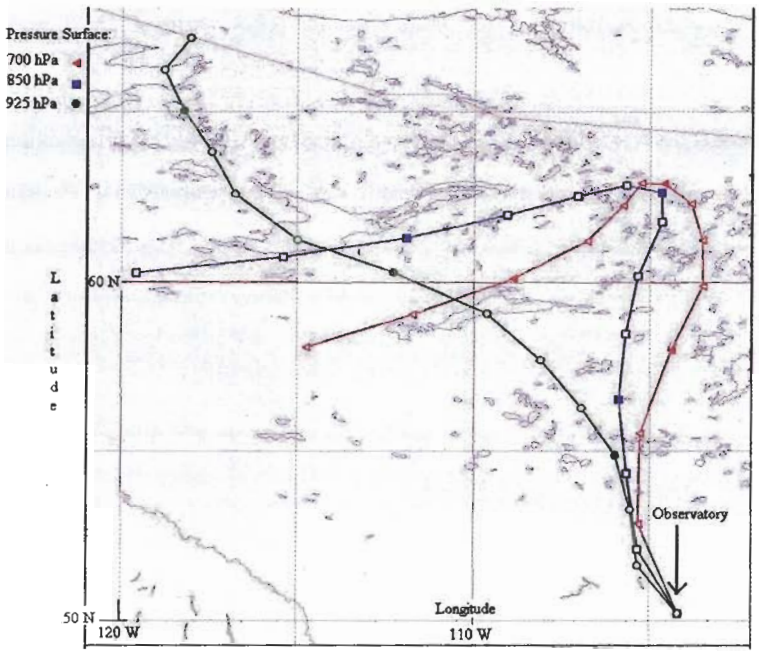

Figure A2.5. Back trajectory analysis for DOY 211 (July 30) at 18Z (UTC) showing flow (in 6 hour intervals). Source: Jacinthe Racine, Canadian Meteorological Centre, Environment Canada.

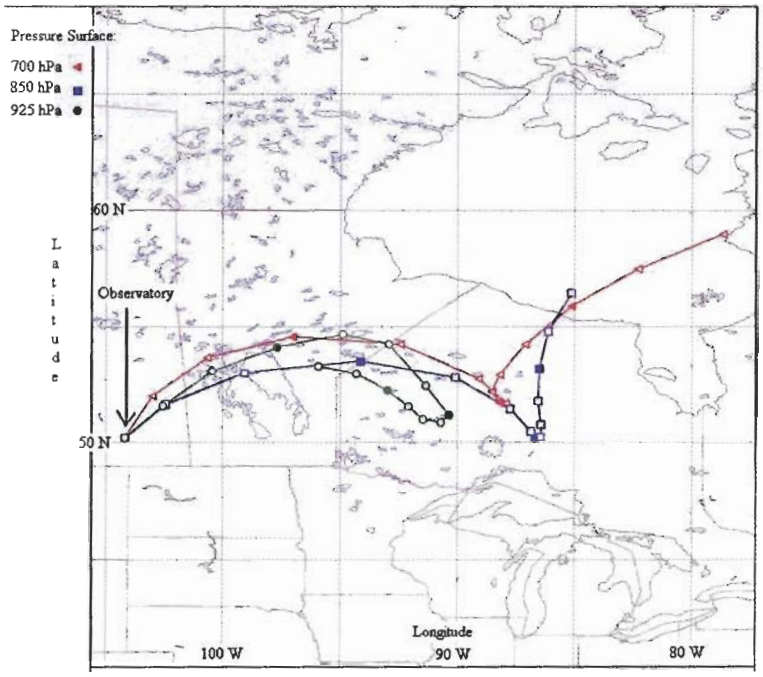

Figure A2.6. Back trajectory analysis for DOY 212 (July 31) at 18Z (UTC) showing flow (in 6 hour intervals). Source: Jacinthe Racine, Canadian Meteorological Centre, Environment Canada.

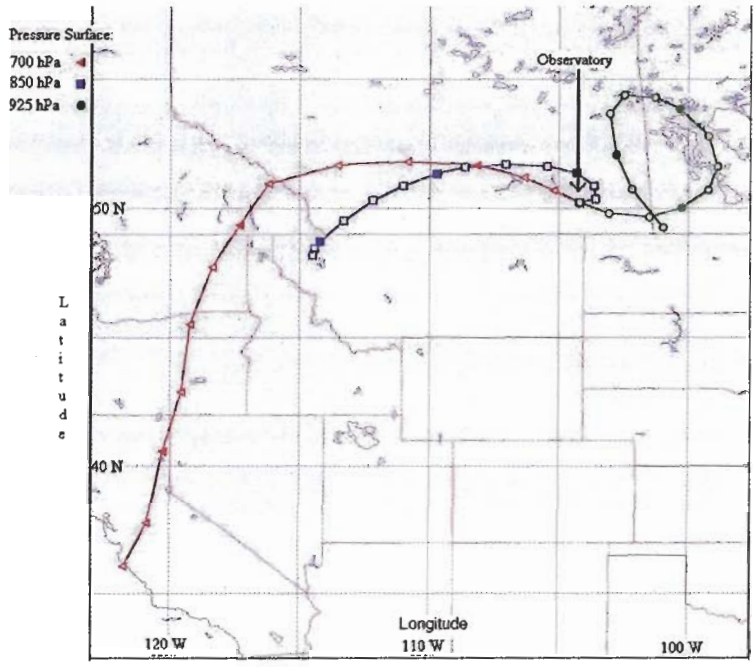

Figure A2.7. Back trajectory analysis for DOY 222 (August 10) at 18Z (UTC) showing flow (in 6 hour intervals). Source: Jacinthe Racine, Canadian Meteorological Centre, Environment Canada.

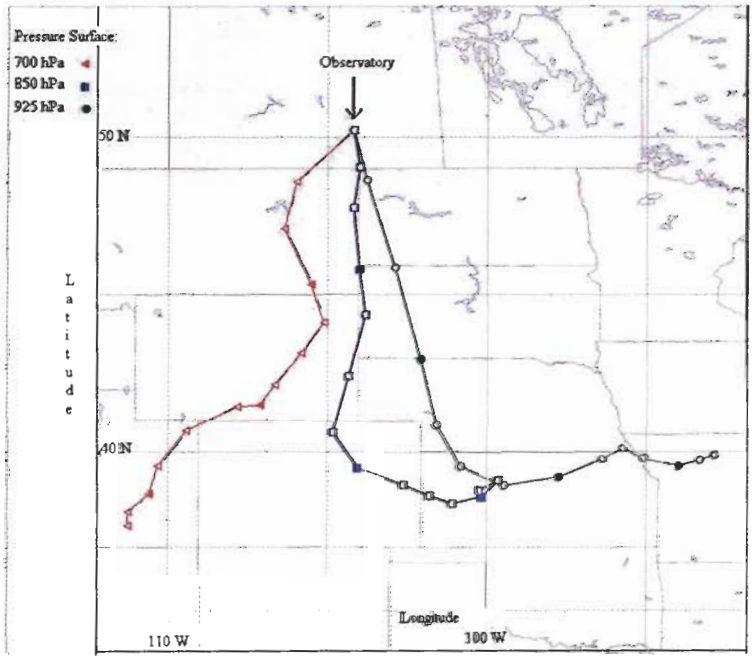

Figure A2.8. Back trajectory analysis for DOY 225 (August 13) at 18Z (UTC) showing flow (in 6 hour intervals). Source: Jacinthe Racine, Canadian Meteorological Centre, Environment Canada.

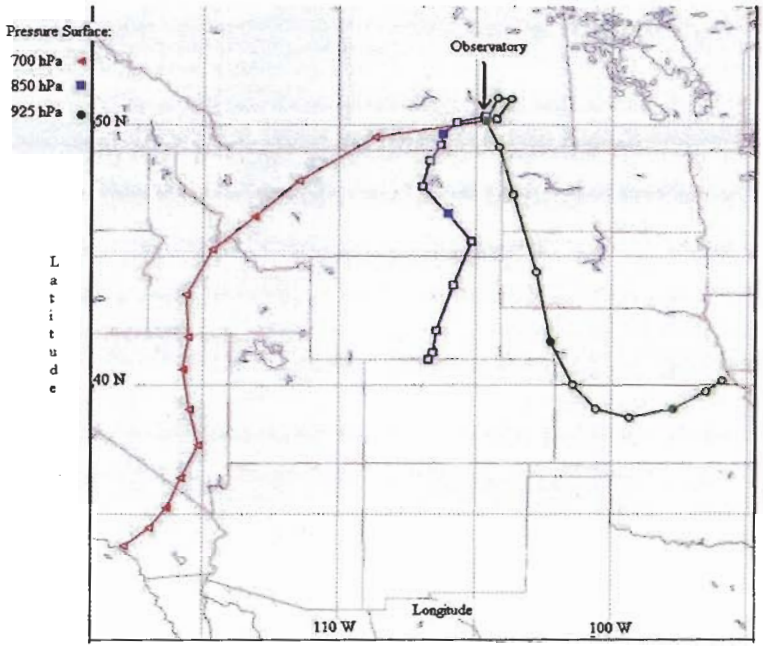

Figure A2.9. Back trajectory analysis for DOY 226 (August 14) at 18Z (UTC) showing flow (in 6 hour intervals) from pyrogenic aerosol source regions. Source: Jacinthe Racine, Canadian Meteorological Centre, Environment Canada.

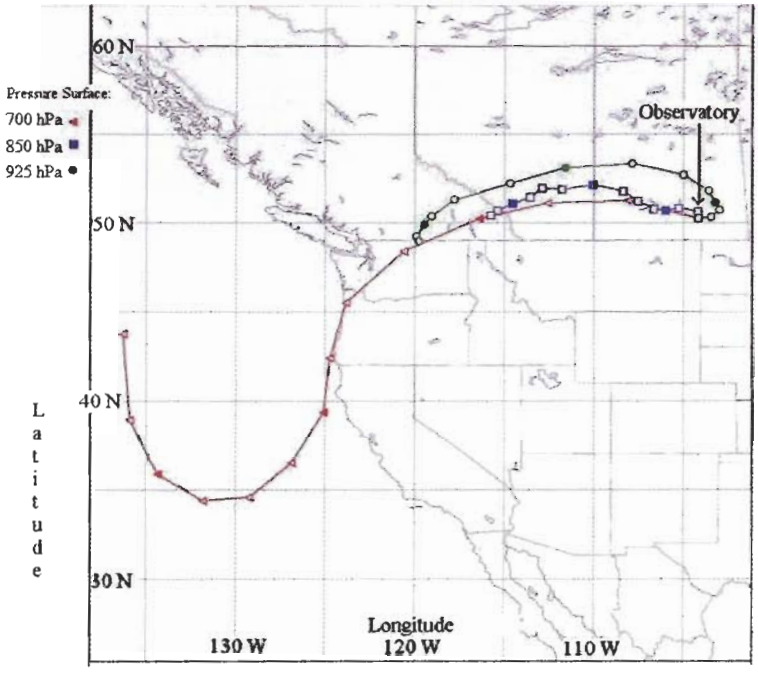

Figure A2.10. Back trajectory analysis for DOY 227 (August 15) at 18Z (UTC) showing flow (in 6 hour intervals) from pyrogenic aerosol source regions. Source: Jacinthe Racine, Canadian Meteorological Centre, Environment Canada.

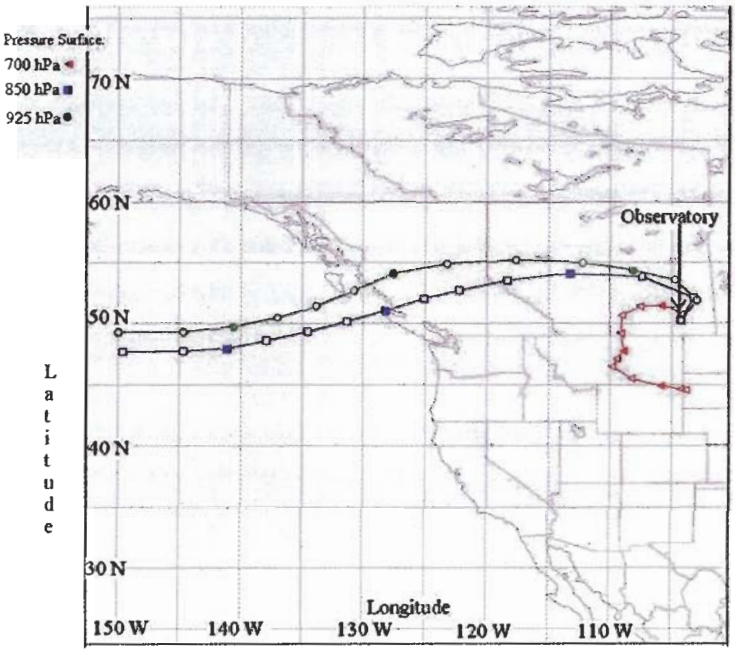

Figure A2.11. Back trajectory analysis for DOY 230 (August 18) at 18Z (UTC) showing flow (in 6 hour intervals) from pyrogenic aerosol source regions. Source: Jacinthe Racine, Canadian Meteorological Centre, Environment Canada.

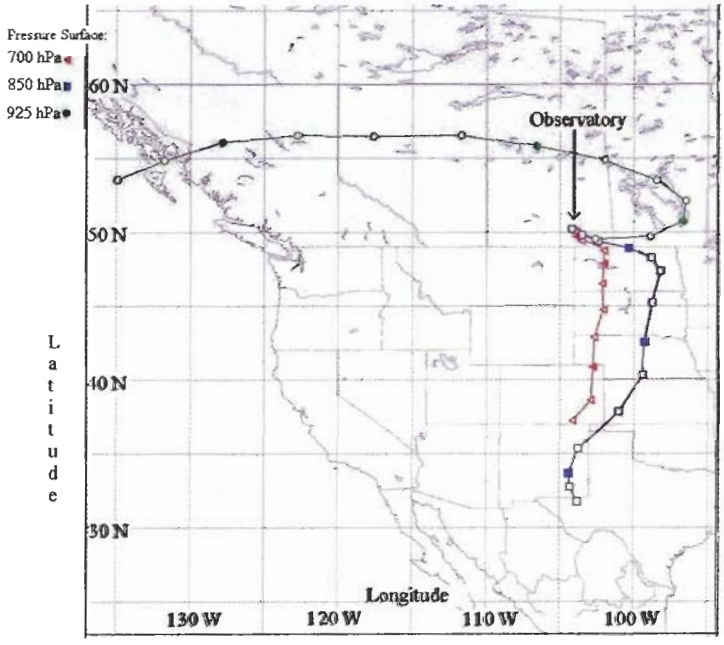

Figure A2.12. Back trajectory analysis for DOY 231 (August 19) at 18Z (UTC) showing flow (6 hour intervals) from pyrogenic aerosol source regions. Source: Jacinthe Racine, Canadian Meteorological Centre, Environment Canada.

Appendix 3.
Houghton Model Sensitivity to Precipitable Water

Precipitable water is the major input parameter needed to operationalize the Houghton model. Water vapour scattering and absorption within the atmosphere is modelled from the following equations

$$\phi_{ws} = 1 - 0.0225\ wm \quad \text{(A3.1)}$$

$$\phi_{wa} = 1 - 0.077\ wm^{0.3} \quad \text{(A3.2)}$$

where water mass (wm) is determined by the product of optical air mass and precipitable water. Due to its impact, it is important to understand the sensitivity of equations A3.1 and A3.2 to uncertainty in precipitable water.

Figures A3.1 through A3.4 provide a sensitivity analysis of ϕ_{ws} and ϕ_{wa} to changes in precipitable water for a range of optical air mass values. Figure A3.1 displays ϕ_{ws} for several precipitable water values across a range of optical air mass values. Figure A3.1 shows that ϕ_{ws} decreases with both increasing optical air mass and precipitable water. From this and Figure A3.2, it is apparent that relatively large changes in precipitable water do not drastically affect the value of ϕ_{ws}, especially for small optical air mass values. However, as optical air mass increases, smaller changes in precipitable water have a more significant effect on ϕ_{ws}. Similar to Figures A3.1 and A3.2, Figures A3.3 and A3.4 show the insensitivity of ϕ_{wa} to changes in precipitable water, especially at low optical air mass. Due to the exponential nature of equation A3.2, large changes in precipitable water and optical air mass do not have the same effect on ϕ_{wa} as they do on ϕ_{ws}. As such, even large changes in precipitable water (i.e. $\pm$ 50%) do not greatly influence ϕ_{wa}, even at large optical air mass values. While it is clear that ϕ_{ws} is more sensitive to changes in precipitable water than ϕ_{wa}, even relatively large changes in precipitable water (i.e. $\pm$ 50%) do not drastically change either. However, it is important

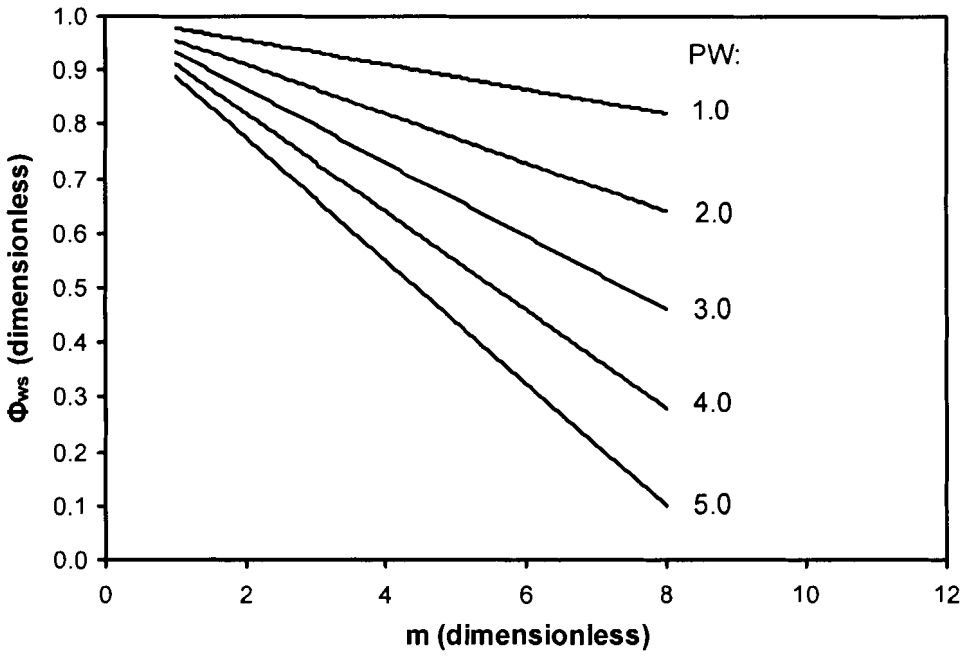

Figure A3.1. Sensitivity of ϕ_{ws} to precipitable water (cm) over a range of optical air mass values.

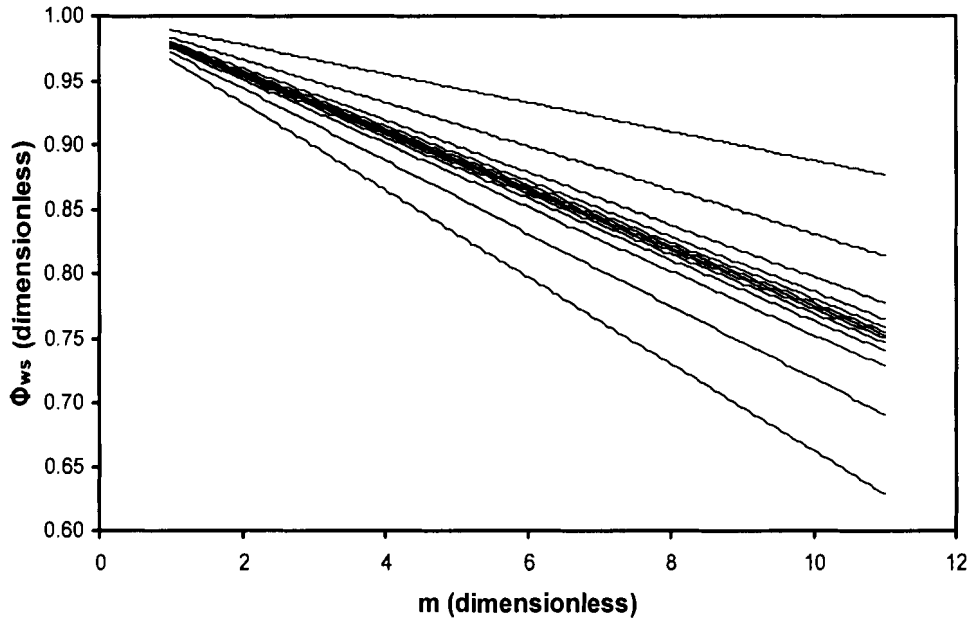

Figure A3.2. Sensitivity of ϕ_{ws} to percentage changes in a 1 cm precipitable water value over a range of optical air mass values. Percentage change, for upper to lower trends are +50, +25, +10, +5, +2.5, +1, -1, -2.5, -5, -10, -25 and -50.

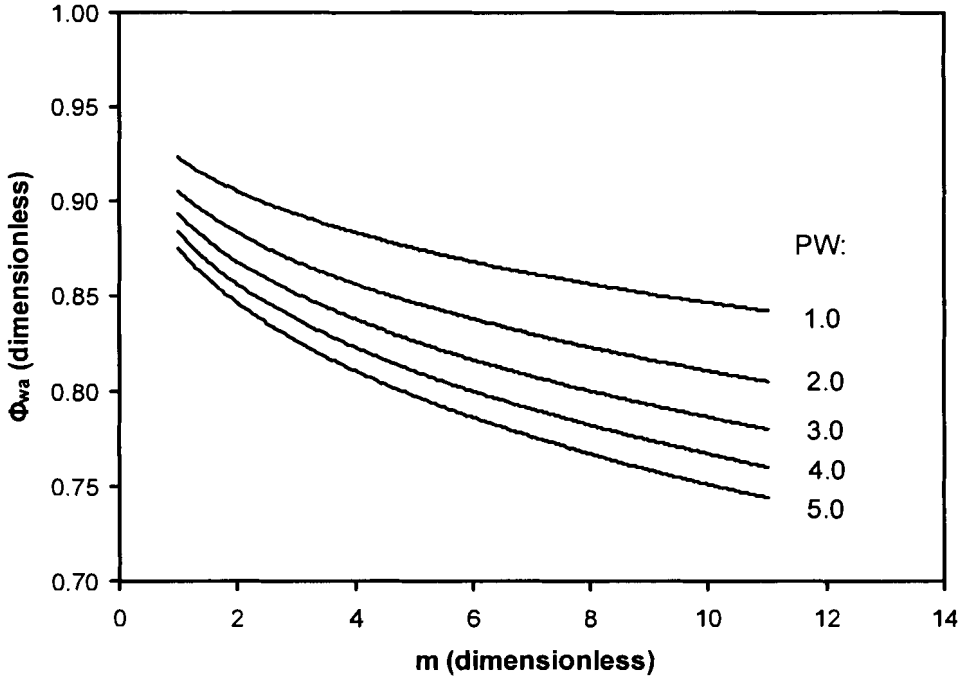

Figure A3.3. Sensitivity of ϕ_{wa} to precipitable water (cm) over a range of optical air mass values.

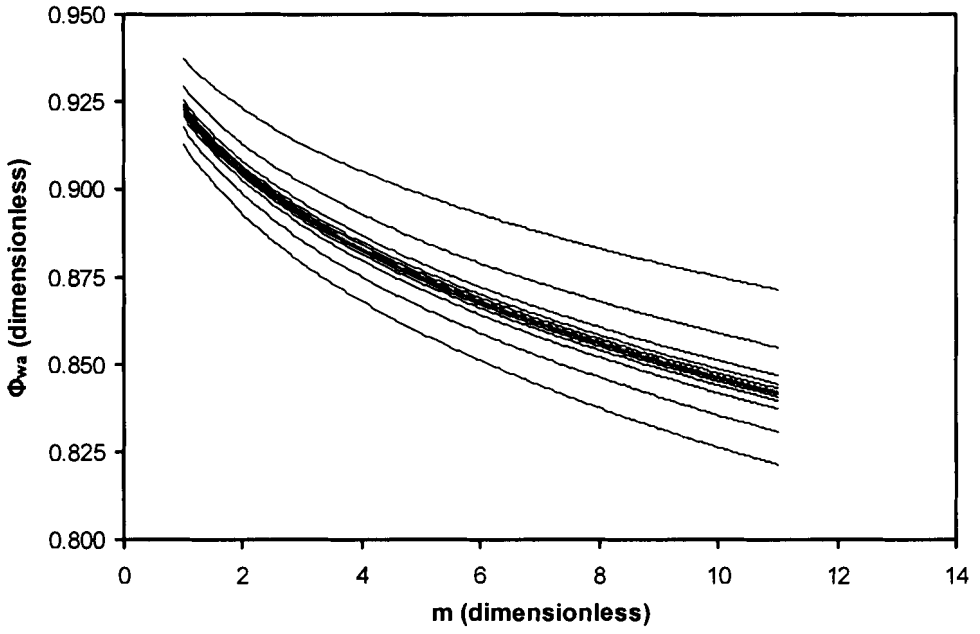

Figure A3.4. Sensitivity of ϕ_{wa} to percentage changes in a 1 cm precipitable water value over a range of optical air mass values. Percentage change, for upper to lower trends are +50, +25, +10, +5, +2.5, +1, -1, -2.5, -5, -10, -25 and -50.

to note the dominant role of ϕ_{ws} in Houghton's water vapour parameterization. Generally, it is ϕ_{ws}, not ϕ_{wa}, which has the greatest effect on surface estimates of irradiance.

Appendix 4.
Houghton Model Sensitivity to Ozone

Even though not a component of the original Houghton model (1954), this study explicitly considers atmospheric absorption by ozone. The ozone transmittance function (ϕ_{o_3}) used in this study is

$$\phi_{o_3} = 1 - [0.1082\, X_1 / (1+ 13.86\, X_1)^{0.805}] + [0.00658\, X_1 / (1 + (10.36\, X_1)^3)] + [0.002118\, X_1 / (1 + 0.0042\, X_1 + 0.00000323\, X_1^2)] \quad \text{(A4.1)}$$

where X_1 is determined by

$$X_1 = m\, U_o \quad \text{(A4.2)}$$

with U_o being the equivalent ozone depth (cm). Equation A4.1 was originally proposed by Lacis and Hansen (1974). Figure A4.1 shows the sensitivity of ϕ_{o_3} to several different ozone depth values. Here, ϕ_{o_3} changes non-linearly with increasing ozone depth and optical air mass. The decrease in ϕ_{o_3} with increasing optical air mass continues until a threshold minimum value is reached, after which ϕ_{o_3} increases with increasing optical air mass. To correct for this result, ϕ_{o_3} values were set as a constant with increasing optical air mass after the minimum ϕ_{o_3} value is reached (Figures A4.1). From Figure A4.1, it is apparent that ϕ_{o_3} is an important model parameterization, distinctly affecting global, direct and diffuse irradiance estimates. However, regardless of optical air mass, atmospheric attenuation from ozone is small, especially when compared to water vapour attenuation. Figure A4.2 shows the sensitivity of ϕ_{o_3} to changes in ozone depth (i.e. ± 1, 2.5, 5, 10, 25 and 50% change from a 0.30 cm ozone depth). Note the relative insensitivity of ϕ_{o_3} with even large changes in ozone depth.

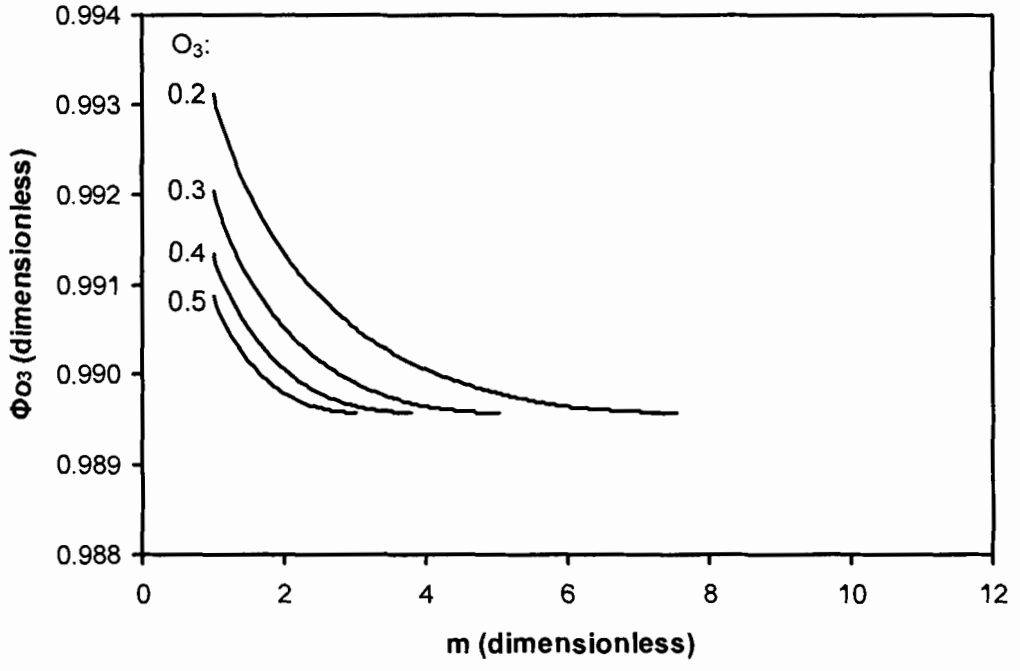

Figure A4.1. Sensitivity of ϕ_{o_3} to ozone depth (cm) over a range of optical air mass values.

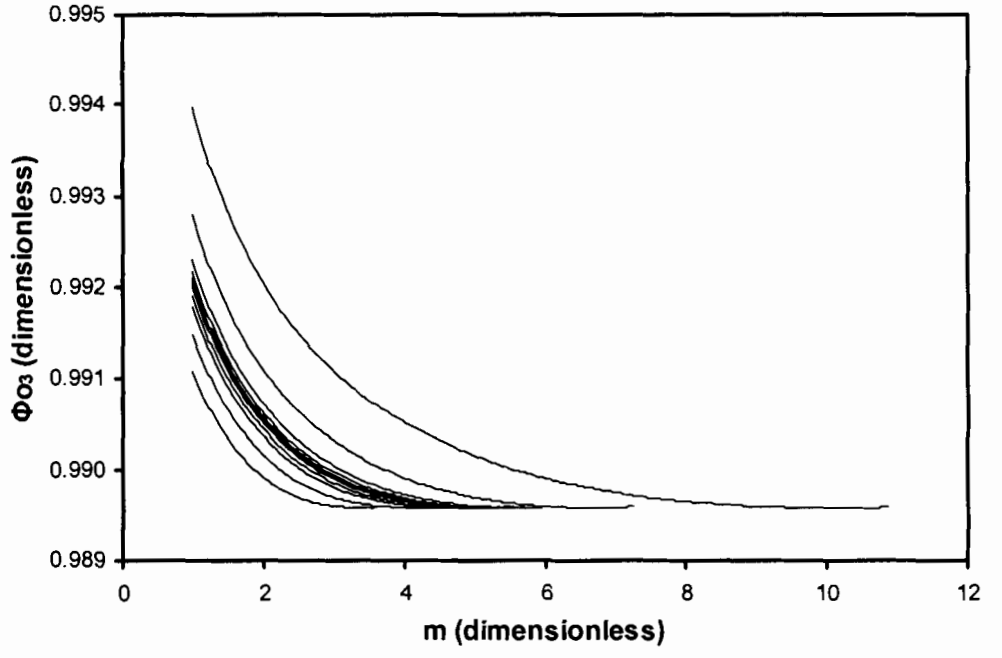

Figure A4.2. Sensitivity of ϕ_{o_3} to percentage changes from a 0.3 cm ozone depth value over a range of optical air mass values. Percentage change, for upper to lower trends are +50, +25, +10, +5, +2.5, +1, -1, -2.5, -5, -10, -25 and -50.

Appendix 5.
Data Tables: Irradiance and Statistical Data

Table A5.1. Conversion between day-of-year and month-day-year time formats.

Calendar Year	Calendar Month											
2003	JAN	FEB	MAR	APR	MAY	JUN	JUL	AUG	SEP	OCT	NOV	DEC
Calendar Day	Day Of Year											
1	1	32	60	91	121	152	182	213	244	274	305	335
2	2	33	61	92	122	153	183	214	245	275	306	336
3	3	34	62	93	123	154	184	215	246	276	307	337
4	4	35	63	94	124	155	185	216	247	277	308	338
5	5	36	64	95	125	156	186	217	248	278	309	339
6	6	37	65	96	126	157	187	218	249	279	310	340
7	7	38	66	97	127	158	188	219	250	280	311	341
8	8	39	67	98	128	159	189	220	251	281	312	342
9	9	40	68	99	129	160	190	221	252	282	313	343
10	10	41	69	100	130	161	191	222	253	283	314	344
11	11	42	70	101	131	162	192	223	254	284	315	345
12	12	43	71	102	132	163	193	224	255	285	316	346
13	13	44	72	103	133	164	194	225	256	286	317	347
14	14	45	73	104	134	165	195	226	257	287	318	348
15	15	46	74	105	135	166	196	227	258	288	319	349
16	16	47	75	106	136	167	197	228	259	289	320	350
17	17	48	76	107	137	168	198	229	260	290	321	351
18	18	49	77	108	138	169	199	230	261	291	322	352
19	19	50	78	109	139	170	200	231	262	292	323	353
20	20	51	79	110	140	171	201	232	263	293	324	354
21	21	52	80	111	141	172	202	233	264	294	325	355
22	22	53	81	112	142	173	203	234	265	295	326	356
23	23	54	82	113	143	174	204	235	266	296	327	357
24	24	55	83	114	144	175	205	236	267	297	328	358
25	25	56	84	115	145	176	206	237	268	298	329	359
26	26	57	85	116	146	177	207	238	269	299	330	360
27	27	58	86	117	147	178	208	239	270	300	331	361
28	28	59	87	118	148	179	209	240	271	301	332	362
29	29	-	88	119	149	180	210	241	272	302	333	363
30	30	-	89	120	150	181	211	242	273	303	334	364
31	31	-	90	-	151	-	212	243	-	304	-	365

Table A5.2. Observed daily irradiance flux densities for the 14 cloudless full and 21 cloudless half days in 2003. The * indicates a cloudless half day; half day totals were converted into full day totals by multiplying by 2. The units are in MJ m^{-2} d^{-1}.

DOY	Extraterrestrial	Global	Direct	Diffuse
1*	7.634	5.365	3.968	1.349
16*	8.986	6.682	5.198	1.420
29*	11.028	8.103	6.250	1.778
39*	13.097	10.304	8.446	1.857
42	13.733	10.981	9.034	1.957
60*	18.536	15.342	12.763	2.679
74*	22.585	17.757	15.034	2.576
112*	33.498	25.089	20.569	4.277
119*	35.284	27.582	23.578	3.787
131	37.725	29.161	24.285	3.908
132*	37.947	29.061	24.314	4.218
145	39.984	30.276	25.586	4.232
169	41.728	31.696	26.809	4.444
196*	40.263	29.966	25.695	3.630
203*	39.358	29.614	25.705	3.231
207*	38.721	28.845	23.778	4.523
209*	38.379	27.827	21.633	5.659
227	34.554	24.240	17.818	5.970
230	33.836	23.207	16.013	6.795
231	33.591	23.549	17.462	5.512
243	30.472	22.941	19.404	2.999
272*	22.155	17.178	14.930	1.883
273	21.851	16.625	14.210	2.009
278	20.407	15.019	12.704	1.994
279	20.122	14.814	12.290	2.148
286*	18.233	13.347	11.142	1.891
312*	11.870	9.295	7.101	1.940
316*	11.133	8.538	6.448	1.779
318	10.723	8.036	6.116	1.581
329*	9.058	6.684	5.016	1.474
331*	8.812	6.609	4.901	1.468
335*	8.392	6.330	4.764	1.304
336*	8.277	5.845	4.188	1.435
356	7.325	5.248	3.910	1.160
357	7.329	5.264	3.886	1.181

Table A5.3. Daily values of the clearness index (c_i), transmissivity (t), diffuse ratio (d_r) and average daily optical air mass (m) ($z < 85°$) for cloudless full and half days in 2003. The * indicates a cloudless half day.

DOY	c_i	t	d_r	m
*1	0.703	0.520	0.177	5.031
*16	0.744	0.579	0.158	4.654
*29	0.735	0.567	0.161	4.217
*39	0.787	0.645	0.142	3.890
42	0.800	0.658	0.143	3.789
*60	0.828	0.689	0.145	3.301
*74	0.786	0.666	0.114	3.001
*112	0.749	0.614	0.128	2.565
*119	0.782	0.668	0.107	2.528
131	0.773	0.644	0.104	2.476
*132	0.766	0.641	0.111	2.476
145	0.757	0.640	0.106	2.440
169	0.760	0.642	0.106	2.431
*196	0.744	0.638	0.090	2.439
*203	0.752	0.653	0.082	2.449
*207	0.745	0.614	0.117	2.459
*209	0.725	0.564	0.147	2.463
227	0.702	0.516	0.173	2.534
230	0.686	0.473	0.201	2.545
231	0.701	0.520	0.164	2.554
243	0.753	0.637	0.098	2.636
*272	0.775	0.674	0.085	3.017
273	0.761	0.650	0.092	3.033
278	0.736	0.623	0.098	3.131
279	0.736	0.611	0.107	3.150
*286	0.732	0.611	0.104	3.305
*312	0.783	0.598	0.163	4.056
*316	0.767	0.579	0.160	4.179
318	0.749	0.570	0.147	4.261
*329	0.738	0.554	0.163	4.621
*331	0.750	0.556	0.167	4.675
*335	0.754	0.568	0.155	4.792
*336	0.706	0.506	0.173	4.824
356	0.716	0.534	0.158	5.136
357	0.718	0.530	0.161	5.133

Table A5.4. Predicted daily irradiance flux densities for the 14 cloudless full and 21 cloudless half days in 2003. The * indicates a cloudless half day; half day totals were converted into full day totals by multiplying by 2. The units are in MJ m^{-2} d^{-1}.

DOY	Extraterrestrial	Global	Direct	Diffuse
1*	7.634	4.761	3.569	1.192
16*	8.986	6.004	4.714	1.291
29*	11.028	7.613	6.130	1.483
39*	13.097	9.427	7.789	1.638
42	13.733	9.703	7.975	1.729
60*	18.536	13.893	11.849	2.045
74*	22.585	16.693	14.251	2.442
112*	33.498	25.386	22.141	3.246
119*	35.284	26.886	23.536	3.350
131	37.725	29.735	26.452	3.283
132*	37.947	29.164	25.676	3.488
145	39.984	30.080	26.202	3.879
169	41.728	31.383	27.356	4.027
196*	40.263	30.425	26.599	3.825
203*	39.358	29.507	25.677	3.830
207*	38.721	28.343	24.294	4.049
209*	38.379	28.659	24.880	3.780
227	34.554	25.435	21.875	3.560
230	33.836	24.322	20.585	3.738
231	33.591	23.955	20.156	3.799
243	30.472	22.535	19.418	3.117
272*	22.155	16.295	13.924	2.371
273	21.851	16.170	13.852	2.318
278	20.407	14.844	12.587	2.256
279	20.122	14.451	12.169	2.283
286*	18.233	12.905	10.756	2.150
312*	11.870	8.209	6.668	1.542
316*	11.133	7.504	6.001	1.503
318	10.723	7.132	5.654	1.479
329*	9.058	5.984	4.693	1.292
331*	8.812	5.780	4.509	1.271
335*	8.392	5.306	4.041	1.265
336*	8.277	5.008	3.682	1.325
356	7.325	4.531	3.379	1.152
357	7.329	4.510	3.351	1.160

Currently, a variety of statistical methods exist which can provide a meaningful assessment of model performance. Such statistical techniques include the mean bias error (MBE), mean absolute error (MAE), root mean square error (RMSE) and index of agreement (d) (Willmott, 1982). Based simply on the difference between predicted and observed data, the formulae for the above techniques are as follows

$$MBE = N^{-1} * \sum(P_i - O_i) \quad (A5.1)$$

$$MAE = N^{-1} * \sum|P_i - O_i| \quad (A5.2)$$

$$RMSE = [N^{-1} * \sum (P_i - O_i)^2]^{1/2} \quad (A5.3)$$

$$d = 1 - [\sum (P_i - O_i)^2 / \sum (|P_i| + |O_i|)^2] \quad (A5.4)$$

where N is the number of cases, P_i the predicted values, and O_i the observed values (Willmott, 1982). If perfect agreement between predicted and observed values is attained, the MBE, MAE and RMSE will equal zero and d will equal one. Employing these techniques, Tables A5.5, A5.6 and A5.7 contain the results from a statistical comparison between one-minute predicted and observed global, direct and diffuse irradiance for each of the 14 cloudless full and 21 cloudless half days in 2003.

Table A5.5. Comparison statistics for one-minute values of predicted and observed global irradiance for the 14 cloudless full and 21 cloudless half days in 2003 at the Bratt's Lake Observatory. The * indicates a cloudless half day. Note: night data (i.e. irradiance = 0 W m^{-2}) were excluded from this analysis.

DOY	MBE (W m^{-2})	MAE (W m^{-2})	RMSE (W m^{-2})	d (dimensionless)
*1	-20.79	20.79	21.07	0.9972
*16	-21.92	21.92	22.13	0.9978
*29	-16.95	16.95	17.14	0.9990
*39	-27.44	27.44	28.67	0.9981
42	-37.04	37.04	38.82	0.9967
*60	-39.32	39.32	41.65	0.9976
*74	-25.58	25.58	26.98	0.9992
*112	6.15	8.64	8.63	0.9999
*119	-13.28	13.28	13.57	0.9999
131	10.82	13.07	14.42	0.9999
*132	2.10	4.11	4.85	1.0000
145	-3.32	4.34	5.25	1.0000
169	-5.23	7.35	8.15	1.0000
*196	8.10	11.07	11.94	0.9999
*203	1.69	6.39	7.63	1.0000
*207	-9.00	9.00	9.97	0.9999
*209	15.23	16.90	18.37	0.9998
227	23.45	24.37	26.29	0.9994
230	22.16	23.29	25.67	0.9994
231	8.32	10.45	12.00	0.9999
243	-8.03	8.05	8.86	0.9999
*272	-20.61	20.61	20.84	0.9995
273	-10.91	10.91	11.24	0.9998
278	-4.21	5.39	6.78	0.9999
279	-8.52	8.54	9.50	0.9999
*286	-11.09	11.09	11.79	0.9998
*312	-32.18	32.18	33.27	0.9969
*316	-32.68	32.68	34.31	0.9963
318	-27.16	27.16	27.98	0.9973
*329	-22.15	22.15	22.99	0.9977
*331	-26.61	26.61	26.97	0.9966
*335	-33.58	33.58	34.52	0.9940
*336	-26.62	26.62	27.07	0.9958
356	-24.72	24.72	25.13	0.9959
357	-25.99	25.99	26.57	0.9954

Table A5.6. Comparison statistics for one-minute values of predicted and observed direct irradiance for the 14 cloudless full and 21 cloudless half days in 2003 at the Bratt's Lake Observatory. The * indicates a cloudless half day. Note: night data (i.e. irradiance = 0 W m^{-2}) were excluded from this analysis.

DOY	MBE (W m^{-2})	MAE (W m^{-2})	RMSE (W m^{-2})	d (dimensionless)
*1	-14.32	14.32	14.79	0.9977
*16	-16.18	16.18	16.62	0.9981
*29	-3.64	4.48	5.96	0.9998
*39	-19.05	19.05	19.69	0.9987
42	-30.01	30.01	31.04	0.9970
*60	-21.06	21.06	21.59	0.9991
*74	-18.95	18.98	19.76	0.9994
*112	31.89	31.91	34.79	0.9988
*119	-0.81	4.28	4.94	1.0000
131	40.41	40.56	46.53	0.9982
*132	25.57	25.58	29.11	0.9993
145	11.32	12.69	14.68	0.9998
169	9.80	12.50	15.63	0.9998
*196	16.50	19.21	21.12	0.9996
*203	-0.43	9.09	10.38	0.9999
*207	9.96	17.37	19.12	0.9997
*209	61.24	61.35	68.30	0.9955
227	81.67	81.70	87.33	0.9912
230	94.35	94.46	106.38	0.9851
231	56.20	56.40	63.32	0.9951
243	0.35	7.75	8.95	0.9999
*272	-24.50	24.50	24.92	0.9990
273	-8.70	8.74	9.60	0.9999
278	-2.94	6.14	7.59	0.9999
279	-3.03	6.01	7.65	0.9999
*286	-10.16	10.16	11.53	0.9997
*312	-13.17	16.17	13.83	0.9992
*316	-13.95	13.95	14.65	0.9989
318	-14.72	14.72	15.06	0.9988
*329	-10.88	11.02	11.68	0.9990
*331	-13.27	13.27	13.60	0.9986
*335	-25.16	25.16	25.90	0.9946
*336	-17.97	17.97	18.20	0.9968
356	-19.31	19.31	19.83	0.9958
357	-19.57	19.57	20.09	0.9956

Table A5.7. Comparison statistics for one-minute values of predicted and observed diffuse irradiance for the 14 cloudless full and 21 cloudless half days in 2003 at the Bratt's Lake Observatory. The * indicates a cloudless half day. Note: night data (i.e. irradiance = 0 W m^{-2}) were excluded from this analysis.

DOY	MBE (W m^{-2})	MAE (W m^{-2})	RMSE(W m^{-2})	d (dimensionless)
*1	-4.74	4.86	6.08	0.9958
*16	-4.06	4.32	5.24	0.9970
*29	-10.08	10.08	11.65	0.9884
*39	-7.61	8.51	10.46	0.9909
42	-7.15	8.35	9.90	0.9923
*60	-18.44	18.76	22.88	0.9699
*74	-3.48	4.42	5.10	0.9984
*112	-20.21	20.21	21.24	0.9815
*119	-8.08	8.08	8.89	0.9962
131	-15.88	17.58	20.50	0.9803
*132	-17.19	17.19	18.88	0.9848
145	-6.16	6.26	7.79	0.9973
169	-6.91	7.09	8.50	0.9969
*196	3.47	6.35	7.60	0.9970
*203	10.99	11.69	12.27	0.9914
*207	-8.42	10.21	12.02	0.9946
*209	-34.10	34.10	37.90	0.9565
227	-46.50	46.50	51.34	0.9312
230	-59.86	59.86	69.42	0.9019
231	-33.49	33.49	37.97	0.9618
243	2.80	3.91	4.48	0.9989
*272	12.51	13.17	13.74	0.9831
273	7.44	8.29	8.69	0.9937
278	6.90	7.79	8.03	0.9947
279	3.80	4.81	5.06	0.9981
*286	7.13	8.12	8.39	0.9941
*312	-11.49	11.49	13.85	0.9845
*316	-9.06	9.06	9.58	0.9921
318	-2.82	3.38	4.14	0.9983
*329	-5.11	5.35	6.58	0.9954
*331	-5.78	6.16	7.59	0.9937
*335	-1.28	2.43	3.19	0.9988
*336	-2.83	3.51	4.29	0.9981
356	0.52	2.39	3.26	0.9986
357	-0.17	2.19	3.07	0.9988

Appendix 6.
Calibration of the OL-754 Portable High Accuracy UV-Visible Spectroradiometer

In order to take full advantage of cloudless sky atmospheric conditions, most calibration activities were run during periods of partial instability or overcast skies, when normal scanning was not permissible. The calibration procedure used throughout the measurement program includes four different lamps; a dual wavelength and gain lamp, a 1000-Watt (S-919) lamp, a 1000-Watt (S-701) lamp and a 200-Watt (OL 752-10E) lamp. The OL 752-150 dual wavelength and gain lamp consists of two small light sources that provide a useful and quick way to check the instrument's accuracy. The first light source is a 4-Watt fluorescent bulb that allows for a wavelength check procedure where the instrument searches for the highest signal around a user defined peak irradiance wavelength. Once the peak is found, the offset (difference between the location of the user defined peak wavelength and where the peak is actually located) is calculated (Optronic Laboratories Inc., 1996). The closer the offset is to zero the more accurately the instrument is operating. The other part of the lamp, the gain light source, allows a response calibration to assess the optical gain of the instrument. The gain light source is a 5-Watt tungsten lamp.

As previously mentioned, one 200-Watt and two 1000-Watt lamps were used to calibrate the OL 754. The 200-Watt lamp is an OL 752-10E tungsten halogen lamp, an irradiance standard traceable to NIST (National Institute of Standards and Technology) (Wu, 2002). An OL 56A programmable current source powers the lamp. This current source maintained a constant current of 6.5 Amps to the lamp, which remained at approximately 0.125 metres from the top of the fused silica dome during the calibration process. This 200-Watt lamp was used to calibrate the OL 754 on a weekly basis.

Both the 1000-Watt S-919 and S-701 lamps are also tungsten halogen lamps, and are irradiance standards traceable to NIST (Wu, 2002). Both lamps were powered by an

XHR 150-7 DC power supply. This power supply maintained a constant current of 8.0 Amps to the lamp, which was secured at a distance of 0.366 metres from the top of the fused silica dome. The 1000-Watt lamp calibrations were undertaken once every three weeks. During each calibration, the lamp was scanned three consecutive times, and the desired system irradiance response values ((W cm^{-2} nm^{-1}) / A) (i.e. the calibration factors) were obtained as the average of these three scans. Despite the fact that the 200-Watt lamp calibration was undertaken on a more regular basis, system irradiance response values from the S-701 lamp were chosen to correct cloudless sky spectral global irradiance (W cm^{-2} nm^{-1}) data obtained from the OL 754.

With respect to the S-701 lamp, the OL 754 was calibrated on July 14 (DOY 195), July 30 (DOY 211) and August 21 (DOY 233) (Figure A6.1). Given that only three calibrations occurred with the S-701 (i.e. system irradiance response values exist only for DOY 195, 211 and 233), and because system response values obtained from all three calibrations were different, linear interpolation was used to calculate system response values (i.e. at each wavelength from 0.28 to 0.80 um) for days between DOY 195, 211 and 233. The following formula denotes system irradiance response values (R_λ) employed in correcting the raw global irradiance signal (S_λ) (Amps) at each wavelength, in order to generate spectral global irradiance values (G_λ)

$$G_\lambda = S_\lambda R_\lambda \quad . \qquad \text{(A6.1)}$$

On one occasion during the summer measurement program, irradiance scans of zinc (Zn), cadmium (Cd), indium (In) and mercury (Hg) lamps were taken (Figures A6.2, A6.3, A6.4 and A6.5). The scans operated on a wavelength range from 0.28 to 0.80 μm. By comparing the spectroradiometer's output against known spectral emission lines for each of the above elements, the spectral response of the instrument can be examined. Table A6.1 provides several known emission lines for zinc, cadmium, indium and mercury from 0.28 to 0.80 μm. While not every emission line shown on Figures A6.2 through A6.5 appears in Table A6.1, a large number coincide.

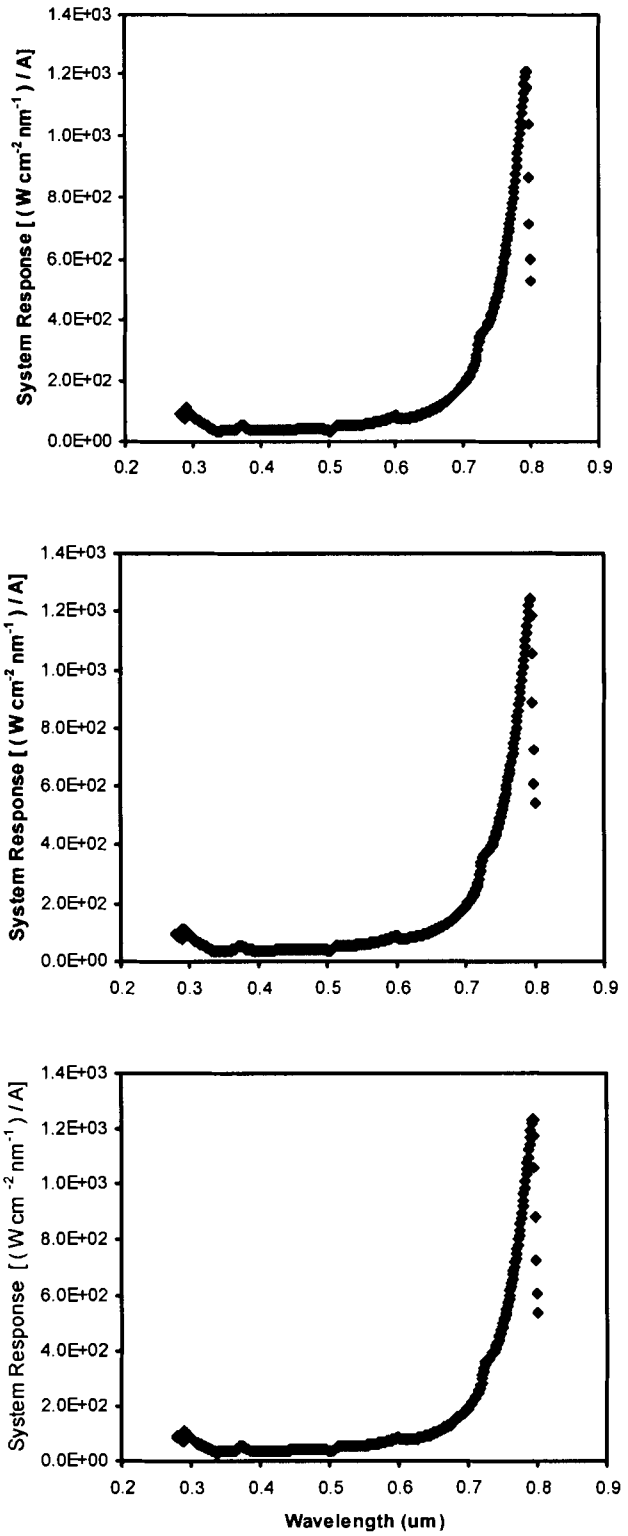

Figure A6.1. From top to bottom, system irradiance response (i.e. calibration factor) values (0.28 – 0.80 μm) obtained as an average of three consecutive scans during 1000-Watt S-701 lamp calibrations on DOY 195, 211 and 233. Note: subtle changes do exist between these three days.

Table A6.1. Known spectral emission lines for zinc, cadmium, indium and mercury from 280 to 800 nm (Robinson, 1991; Oceanoptics.com, 2005; International Accreditation New Zealand, 2003).

	Element			
	zinc (Zn)	cadmium (Cd)	indium (In)	mercury (Hg)
Emission Lines (nm):	328	326	304	297
	330	340	326	302
	335	347	410	313
	468	361	451	334
	472	468		365
	481	480		366
	636	509		405
		644		408
				436
				546
				577
				579

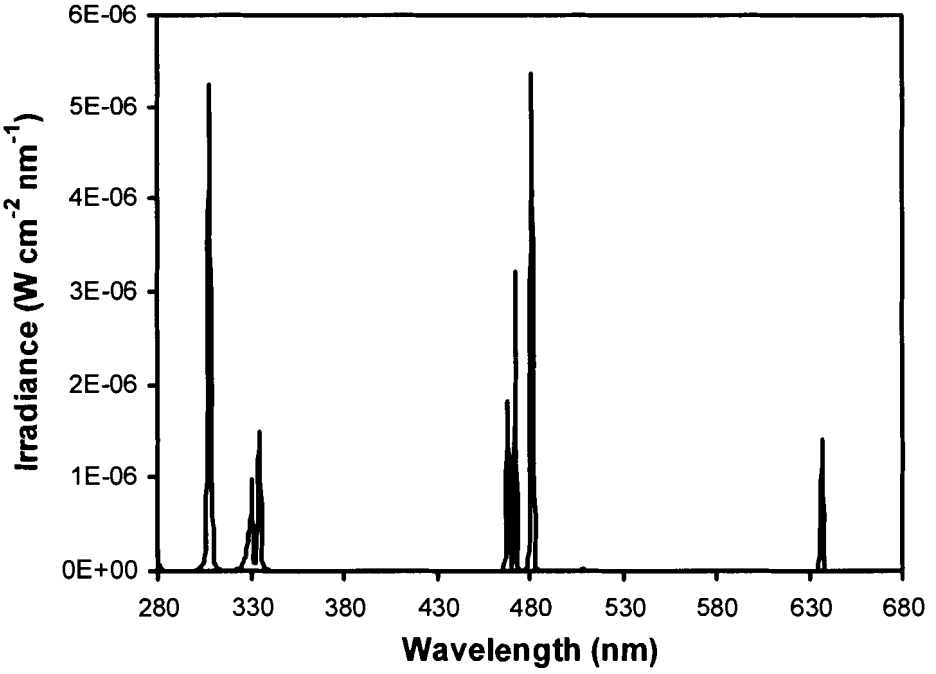

Figure A6.2. Irradiance scan of zinc (Zn) lamp. Spectral emission lines given in Table A6.1 correspond to peaks in figure.

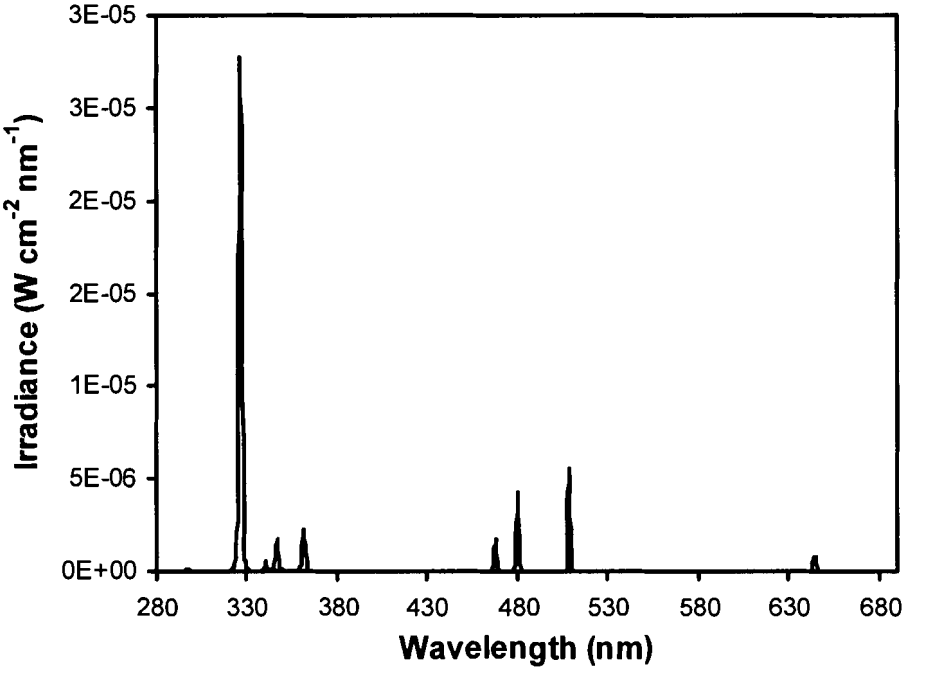

Figure A6.3. Irradiance scan of cadmium (Cd) lamp. Spectral emission lines given in Table A6.1 correspond to peaks in figure.

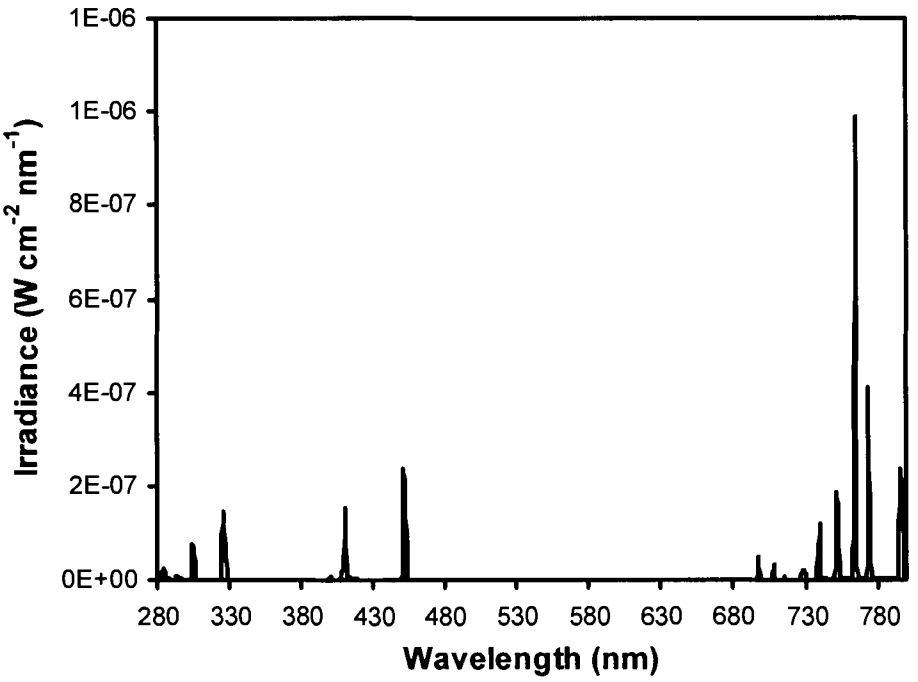

Figure A6. 4. Irradiance scan of indium (In) lamp. Spectral emission lines given in Table A6.1 correspond to peaks in figure.

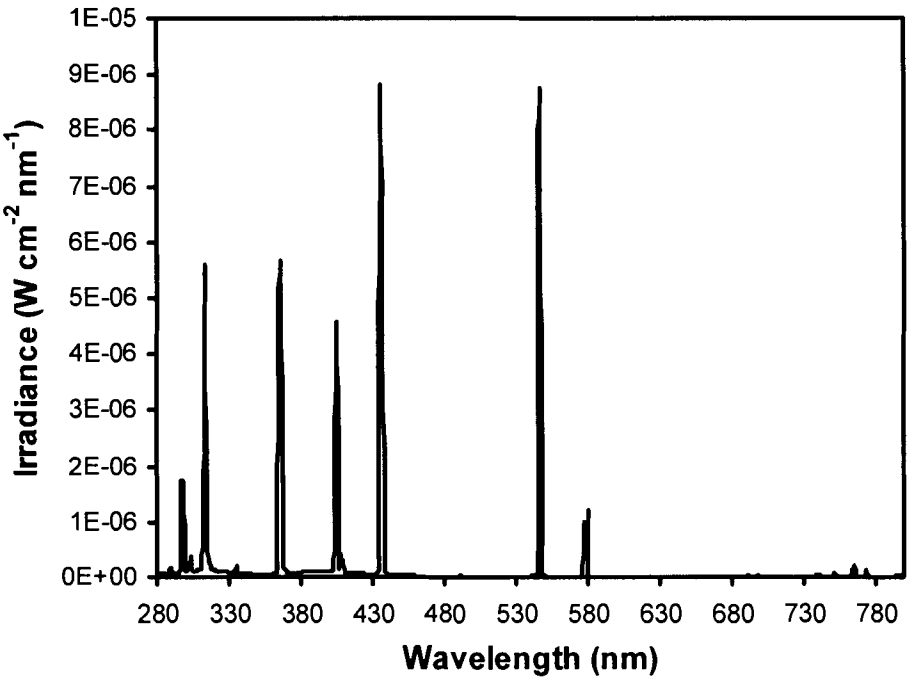

Figure A6.5. Irradiance scan of mercury (Hg) lamp. Spectral emission lines given in Table A6.1 correspond to peaks in figure.

References

Adeyefa, Z. D. and B. Holmgren, 1996: Spectral solar irradiance before and during a Harmattan dust spell. *Sol. Energy,* **57**, 195-203.

American Society for Testing and Materials, 2000: Standard solar constant and zero air mass solar spectral irradiance tables. Standard E 490-00. *Annual book of ASTM standards,* American Society for Testing and Materials, 473-488.

Arvesen, J. C., R. N. Griffin and B. D. Pearson, 1969: Determination of extraterrestrial solar spectral irradiance from a research aircraft. *Appl. Opt.,* **8**, 2215-2232.

Betts, T. R., R. Gottschalg and D. G. Infield, 2001: Progress towards modelling solar spectral radiation for optimisation of amorphous silicon photovoltaic systems. *Proceedings of Conference C76 of the Solar Energy Society,* Belfast, 163-170.

Bird, R. E., R. L. Hulstrom, A. W. Kliman and H. G. Eldering, 1982: Solar spectral measurements in the terrestrial environment. *Appl. Opt.,* **21**, 1430-1436.

Davies, J. A. and D. C. McKay, 1989: Evaluation of selected models for estimating solar radiation on horizontal surfaces. *Sol. Energy,* **43**, 153-168.

Davies, J. A. and D. C. McKay, 1982: Estimating solar irradiance and components. *Sol. Energy,* **29**, 55-64.

Davies, J. A., W. Schertzer and M. Nunez, 1975: Estimating global solar radiation. *Bound.-Layer Meteor.,* **9**, 33-52.

Dexter, R. H., 2004: Diurnal and seasonal albedo trends of wheat at the Bratt's Lake Observatory, Saskatchewan. M.S. thesis, Department of Geography, Simon Fraser University, 113 pp.

Eck, T. F., B. N. Holben, J. S. Reid, O. Dubovik, A. Smirnov, N. T. O'Neill, I. Slutsker and S. Kinne, 1999: Wavelength dependence of the optical depth of biomass burning, urban, and dust aerosols. *J. Geophys. Res.*, **104**, 31,333-31,349.

Filmon, G., 2004: Firestorm 2003 provincial review. 100 pp. [available online at http://www.2003firestorm.gov.bc.ca/firestormreport/default.htm].

Friedlander, S. K., 1977: *Smoke, Dust and Haze.* John Wiley & Sons Inc., 317 pp.

Fung, K. (Editor), 1999: *Atlas of Saskatchewan.* PrintWest, 336 pp.

Gleason, K. L., A. M. Waple, T. Eichler and G. D. Bell, 2004: State of the climate in 2003, 6. a. II. Regional climate United States of America. *Bull. Amer. Meteor. Soc.*, **85**, S36-S41.

Gueymard, C., 2000: Prediction and performance assessment of mean hourly global radiation. *Sol. Energy,* **68**, 285-303.

Gueymard, C., 1995: SMARTS2, a simple model of the atmospheric radiative transfer of sunshine: Algorithms and performance assessment. Florida Solar Energy Center Report No. PF-270-95, 78 pp.

Gueymard, C. A., 2004: The Sun's total and spectral irradiance for solar energy applications and solar radiation models. *Sol. Energy,* **76**, 423-453.

Gueymard, C. A., J. K. Vaughan, N. S. Laulainen and F. E. Vignola, 2000: China's dust affects solar resource in the U.S.: A case study. *ASES 'SOLAR 2000',* Madison, Wis., 1-6.

Gutro, R. J., G. Pelloille, H. Mackey and W. Bruce, 2002: Nasa and Canada study smoke from flaming Canadian forests. *NASA News Arch.*, August 6, 1-4.

Hare, F. K. and M. K. Thomas, 1974: *Climate Canada.* Wiley Publishers of Canada Ltd., 256 pp.

Harrison, L., J. Michalsky and J. Bernt, 1994: Automated multifilter rotating shadow-band radiometer: An instrument for optical depth and radiation measurements. *Appl. Opt.*, **33**, 5118-5125.

Hay, J. E., 1971: Precipitable water over Canada; II distribution. *Atmosphere,* **9**, 101-111.

Holben, B. N., D. Tanré, A. Smirnov, T. F. Eck, I. Slutsker, N. Abuhassan, W. W. Newcomb, J. S. Schafer, B. Chatenet, F. Lavenu, Y. J. Kaufman, J. Vande Castle, A. Setzer, B. Markham, D. Clark, R. Frouin, R. Halthore, A. Karneli, N. T. O'Neill, C. Pietras, R. T. Pinker, K. Voss and G. Zibordi, 2001: An emerging ground-based aerosol climatology: Aerosol optical depth from AERONET. *J. Geophys. Res.*, **106**, 12,067-12,097.

Houghton, H. G., 1954: On the annual heat balance of the northern hemisphere. *J. Meteor.*, **11**, 1-9.

Idso, S. B., 1970: The transmittance of the atmosphere for solar radiation on individual clear days. *J. Appl. Meteor.*, **9**, 239-241.

Intergovernmental Panel on Climate Change, 2001: *Climate change 2001: The scientific basis. Contribution of working group I to the third assessment report of the intergovernmental panel on climate change.* Cambridge University Press, 881 pp.

International Accreditation New Zealand, 2003: Technical guide: UV / Vis spectrophotometer calibration procedures. IANZ Tech. Guide AS TG4, 6 pp. [available online at http://www.ianz.govt.nz/publications2/pdfs/AS_TG4_UV-VIS_Spectro_May_03.pdf].

Iqbal, M., 1983: *An Introduction to Solar Radiation.* Academic Press, 390 pp.

Jacovides, C. P., M. D. Steven and D. N. Asimakopoulos, 2000: Spectral solar irradiance and some optical properties for various polluted atmospheres. *Sol. Energy,* **69**, 215-227.

Johnson, C. W., cited 2005. The solar constant: 1.3661 and the Earth/matriX temperature scale: 1.366085811. [available online at http://www.earthmatrix.com/sciencetoday/solar-constant.html.].

Kasten, F., 1966: A new table and approximation formula for the relative optical air mass. *Arch. Meteor. Geophys. Bioklimatol.,* **B14**, 206-223.

Kelly, D. J. and M. L. Bothwell, 2002: Avoidance of solar ultraviolet radiation by juvenile coho salmon (Oncorhynchus kisutch). *Can. J. Fish. Aquat. Sci.,* **59**, 474-482.

Kelly, D. J., M. L. Bothwell and D. W. Schindler, 2003: Effects of solar ultraviolet radiation on stream benthic communities: An intersite comparison. *Ecology,* **84**, 2724-2740.

Lacis, A. A. and J. E. Hansen, 1974: A parameterization for the absorption of solar radiation in the Earth's atmosphere. *J. Atmos. Sci.,* **31**, 118-133.

Latha, K. M. and K. V. S. Badarinath, 2004: Direct radiative forcing of aerosols over a typical tropical urban environment. *Sol. Energy,* **77**, 225-229.

Levinson, D. H. and D. Phillips, 2004: State of the climate in 2003, 6. a. I. Regional climate Canada. *Bull. Amer. Meteor. Soc.,* **85**, S34-S36.

Liou, K. N., 1980: *An Introduction to Atmospheric Radiation.* Academic Press, Inc., 392 pp.

Markham, B. L., J. S. Schafer, B. N. Holben and R. N. Halthore, 1997: Atmospheric aerosol and water vapor characteristics over north central Canada during BOREAS. *J. Geophys. Res.,* **102**, 29,737-29,745.

Martínez-Lozano, J. A., M. P. Utrillas and F. Tena, 1995: Spectral solar irradiance in the range 300 – 1100 nm measured at Valéncia, Spain. *Renew. Energ.,* **6**, 997-1003.

McArthur, L. J. B., 1998: Baseline surface radiation network (BSRN) operations manual (version 1.0). WMO / TD Report No. 87, 69 pp.

McCullough, E. C., 1968: Total daily radiant energy available extraterrestrially as a harmonic series of the day of year. *Arch. Meteor. Geophys. Bioklimatol.,* **B16**, 129-143.

McDonald, J. E., 1960: Direct absorption of solar radiation by atmospheric water vapour. *J. Meteor.,* **17**, 319-328.

McMahon, C. K., 1999: Forest fire and smoke-impacts on air quality and human health in the USA. *TAPPI International Environmental Conference,* Nashville, Tenn., TAPPI Press, 443-453.

Michalsky, J. J., 1988: The astronomical almanac's algorithm for approximate solar position (1950-2050). *Sol. Energy,* **40**, 227-235.

Miller, J. R. and N. T. O'Neill, 1997: Multialtitude airborne observations of insolation effects of forest fire smoke aerosols at BOREAS: Estimates of aerosol optical parameters. *J. Geophys. Res.,* **102**, 29,729-29,736.

Monteith, J. L., 1962: Attenuation of solar radiation: A climatological study. *Quart. J. Roy. Meteor. Soc.,* **88**, 508-521.

Myers, D., 2004: Terrestrial solar spectral modelling for renewable energy applications. *ASES 'SOLAR 2004',* Portland, Ore., National Renewable Energy Laboratory, 1-26.

National Interagency Coordination Center, 2003: 2003 statistics and summary report. 60 pp. [available online at http://www.nifc.gov/news/2003_statssumm/intro_summary.pdf].

Neckel, H. and D. Labs, 1984: The solar radiation between 3300 and 12500 Å. *Sol. Phys.,* **90**, 205-258.

Nicolet, M., 1989: Solar spectral irradiances with their diversity between 120 and 900 nm. *Planet. Space Sci.,* **37**, 1249-1289.

O'Neill, N. T., T. G. Eck, B. N. Holben, A. Smirnov, A. Royer and Z. Li, 2002: Optical properties of boreal forest fire smoke derived from Sun photometry. *J. Geophys. Res.,* **107**, AAC 6-1-AAC 6-19.

Ocean Optics Inc., cited 2005. HG-1 Mercury Argon calibration source. [available online at http://www.oceanoptics.com/Products/hg1.asp.].

Oke, T. R., 1987: *Boundary Layer Climates.* Routledge, 435 pp.

Optronic Laboratories Inc., 1996: OL 754 portable high accuracy UV-Visible spectroradiometer. Optronic Laboratories Instrument Manual M000170, 139 pp.

Phillips, D., 1990: *The Climates of Canada.* Canadian Government Publishing Centre, 176 pp.

Pinker, R. T., B. Zhang and E. G. Dutton, 2005: Do satellites detect trends in surface solar radiation. *Science,* **308**, 850-854.

Power, H. C., 2003: The geography and climatology of aerosols. *Prog. Phys. Geog.,* **27**, 502-547.

Pueschel, R. F., J. M. Livingston, P. B. Russell, D. A. Colburn, T. P. Ackerman, D. A. Allen, B. D. Zak and W. Einfeld, 1988: Smoke optical depths: Magnitude, variability, and wavelength dependence. *J. Geophys. Res.,* **93**, 8388-8402.

Renewable Resource Data Center, cited 2005. Solar spectra: Airmass zero. [available online at http://rredc.nrel.gov/solar/spectra/am0/.].

Rizk, H. F. S., S. A. Farag, A. A. Ateia and A. El-Bialy, 1985: Effect of pollutant aerosols on spectral atmospheric transmissivity in Cairo. *Environ. Int.,* **11**, 487-492.

Robaa, S. M., 2004: A study of ultraviolet solar radiation at Cairo urban area, Egypt. *Sol. Energy,* **77**, 251-259.

Robinson, G. D., 1962: Absorption of solar radiation by atmospheric aerosol as revealed by measurements at the ground. *Arch. Meteor. Geophys. Bioklimatol.,* **B12**, 19-40.

Robinson, J. W., 1991: *Practical Handbook of Spectroscopy.* CRC Press Inc., 928 pp.

Rottman, G., 1999: Solar ultraviolet irradiance and its temporal variation. *J. Atmos. Sol.-Terr. Phy.,* **61**, 37-44.

Smirnov, A., N. T. O'Neill, A. Royer, A. Tarussov and B. McArthur, 1996: Aerosol optical depth over Canada and the link with synoptic air mass types. *J. Geophys. Res.*, **101**, 19,299-19,318.

Smith, E. V. P. and D. M. Gottlieb, 1974: Solar flux and its variations. *Space Sci. Rev.*, **16**, 771-802.

Thekaekara, M. P., A. J. Drummond, D. G. Murcray, P. R. Gast, E. G. Laue and R. C. Wilson, 1971: Solar electromagnetic radiation. NASA Report No. SP-8005, 33 pp.

Thuillier, G., M. Hersé, D. Labs, T. Foujols, W. Peetermans, D. Gillotay, P. C. Simon and H. Mandel, 2003: The solar spectral irradiance from 200 to 2400 nm as measured by the SOLSPEC spectrometer from the ATLAS and EURECA missions. *Sol. Phys.*, **214**, 1-22.

Unsworth, M. H. and J. L. Monteith, 1972: Aerosol and solar radiation in Britain. *Quart. J. Roy. Meteor. Soc.*, **98**, 778-797.

Van der Linden, R. A. M., cited 2005. Online catalogue of the sunspot index. [available online at http://sidc.oma.be/index.php3.].

VanHoosier, M. E., 1996: Solar ultraviolet spectral irradiance data with increased wavelength and irradiance accuracy. *SPIE Proceedings,* Vol. 2831, 57-64.

Wardle, D. I., L. Dahlgren, K. Dehne, L. Liedquist, L. J. B. McArthur, Y. Miyake, O. Motschka, C. A. Velds and C. V. Wells, 1996: Improved measurements of solar irradiance by means of detailed pyranometer characterisation. International energy agency-solar heating and cooling programme, task 9. IEA-SHCP Report No. 9C-2, 217 pp.

Wehrli, C., 1985: *Extraterrestrial Solar Spectrum. Pub. No. 615.* World Radiation Center, Davos Dorf, Switzerland.

Whitlock, C. H., T. P. Charlock, W. F. Staylor, R. T. Pinker, I. Laszio, A. Ohmura, H. Gilgen, T. Konzelman, R. C. DiPasquale, C. D. Moats, S. R. LeCroy and N. A. Ritchey, 1995: First global WCRP shortwave surface radiation budget dataset. *Bull. Amer. Meteor. Soc.*, **76**, 905-922.

Willmott, C. J., 1982: Some comments on the evaluation of model performance. *Bull. Amer. Meteor. Soc.*, **63**, 1309-1313.

World Climate Research Programme, 1991: Radiation and climate. Second workshop on the implementation of the baseline surface radiation network. Davos, Switzerland, 6-9 August 1991. WMO/TD Report No. 453, 26 pp.

World Health Organization, 2002: *Global solar UV index: A practical guide.* World Health Organization, Geneva, Switzerland, 28 pp.

World Meteorological Organization, 2003: Scientific assessment of ozone depletion: 2002. Global Ozone Research and Monitoring Project Report No. 47, 498 pp.

Wu, E. K., 2002: Laboratory experiments with the Optronic OL 754-O-PMT spectroradiometer. *Poster Presentation at the Seventh BSRN Science and Review Workshop. May 28 to 31,* Regina, Saskatchewan.